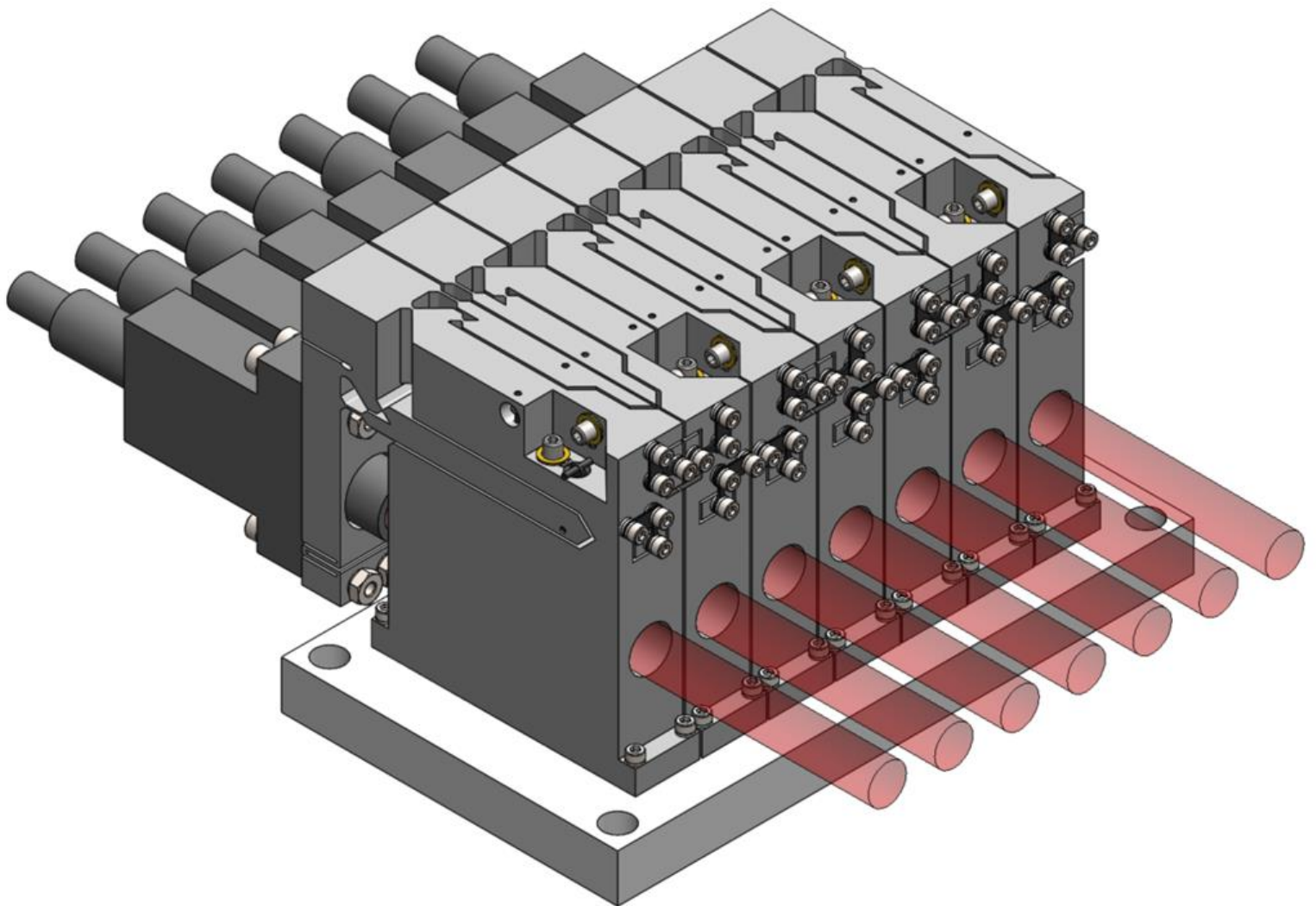


Department of Precision and Microsystems Engineering

Design and Validation of a Collimator Alignment Assembly for a High-Power Bulk Multiplexer used in Ground-to-GEO Laser Communication

J.B. Lutgerink

Report no : MOOM_2019.026
Coach : Dr.ir. L.A. Cacace
Professor : Ir. J.W. Spronck (Associate Professor)
Specialisation : Opto-Mechatronics
Type of report : Master of Science Thesis
Date : 29 August 2019

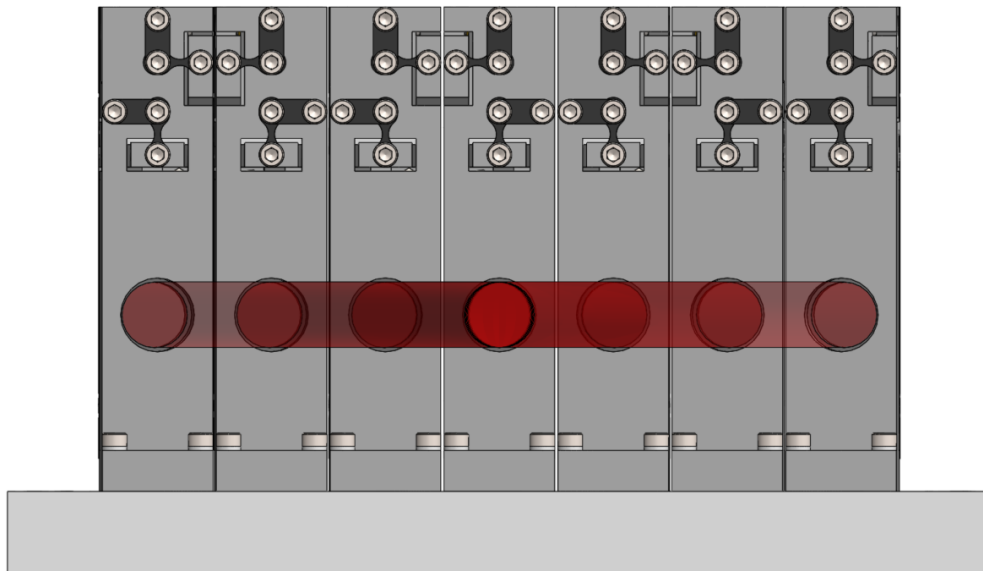


Design and Validation of a Collimator Alignment Assembly for a High-Power Bulk Multiplexer used in Ground-to-GEO Laser Communication

by

J.B. Lutgerink

to obtain the degree of Master of Science
at the Delft University of Technology,
to be defended publicly on Thursday August 29, 2019 at 14:45.



Student number: 4348249
Project duration: September 10, 2018 – August 29, 2019
Thesis committee: Ir. J.W. Spronck (Associate Professor), TU Delft, chair
Ir. J. Rommers, TU Delft, external member
Prof.dr.ir. G.V. Vdovine, TU Delft, external member
Dr.ir. L.A. Cacace, TU Delft, supervisor/coach
Dr.ir. J. de Vreugd, TNO, supervisor
Dr.ir. F. Pettazzi, TNO, supervisor

This thesis is confidential and cannot be made public until August 31, 2024.

An electronic version of this thesis is available at <http://repository.tudelft.nl/>.

Abstract

The average worldwide internet traffic demand in 2022 is projected to be over 1200 Terabits per second. A fifth of this data would be transmitted using mobile networks. One of the technologies used for this is radio frequency (RF) telecommunication, but this technology is reaching its limits. Despite ongoing development, typical data rates are still in the order of Gigabits per second per link.

TNO is working on a telecommunication link (called TOmCAT) that can reach data transfer rates of a Terabit per second. The high data rate is achieved using a very promising alternative to RF telecommunication: optical telecommunication, which is also known as laser communication.

In order to reach the intended data rates, the data needs to be spread over multiple optical frequencies. These signals need to be combined into one transmitted beam using a free-space optical bulk multiplexer.

The laser beams that are transmitted by their collimators need to be aligned with respect to each other in order to reach the satellite as one beam. The footprint available for the required alignment mechanisms is very limited. Furthermore, the system needs to achieve a good thermal and mechanical stability in order to meet the strict specifications.

The aim of this thesis is two-fold: to show the need for achieving state-of-the-art alignment specifications with strict footprint constraints, and to defend the steps taken to achieve these requirements. The research spans the entire design process of the alignment assembly: from higher/system level trade-offs and calculations, to the derivation of the design specifications, to the conceptual and detailed design, and concluding with the manufacturing and testing of the first prototype.

Preface

This thesis is written as the main documentation for my graduation project at TNO Delft Stieltjesweg, where I started my internship at September 10, 2018. I am very glad that I was able to bring together a wide variety of disciplines in this project, and managed to complete a full design circle. Besides meeting the original, diverse objectives, I also made additional contributions to the Bulk Multiplexer project. The main additional contribution was the spectral analysis of the effect of a diffraction grating on a modulated laser beam. The original intention was to properly understand and visualize this black box as part of the literature survey, because it was already known that it had severe implications on the design criteria for the Bulk Multiplexer project. However, during my investigation I found that the problem was actually more severe than previously anticipated. Since my results were confirmed by other models, this actually led to an update in the optical design and earned me the position of co-writer in a paper about the subject.

The method of opening every relevant black box has been my preferred strategy throughout this thesis. My aim has been that anyone who reads this document can come to the same level of understanding on this subject as I achieved throughout my project, but in a fraction of the time. The literature survey is designed to answer the questions that arose during the project about the optical design and its implications on the mechanical design.

During the design phase of the project, it was decided to make and test a first prototype of the proposed design. Unfortunately, this prototype phase took much longer than initially anticipated due to practical issues. The most severe individual delay of four weeks was due to a technical issue at the 3D-printing company. However, the end result was a working prototype that could be used to validate and tune the COMSOL model. Thus the project could be wrapped up with interesting recommendations for the final design of the collimator alignment assembly to be used in the TOMCAT project.

As mentioned, the wide variety of disciplines and activities made for a very interesting project that allowed for me to learn a lot of soft and hard skills that the regular curriculum at the TU Delft could not offer. I gained experience acting as chair in meetings of professionals each with different expertise, guiding the discussions to a set of useful conclusions and action points. I also learned to set and keep my own deadlines and schedule, while achieving the objectives and sometimes more. Furthermore, I was repeatedly challenged to make reliable claims regarding my design, as well as the spectral analysis mentioned earlier.

Other skills I learned include presenting my work to mechanical experts, setting up a realistic FEM model, obtaining a budget for my prototype, designing whilst communicating with manufacturers/suppliers, repairing a broken auto-collimator (including electrical design and soldering of a custom power supply), building and maintaining a microrad-stable test setup, obtaining reliable data, and data analysis.

All in all it has been an interesting and educational journey, bringing together all my major passions and talents, and I believe I will treasure my time at TNO and the lessons learned for years to come.

*J.B. Lutgerink
Delft, August 2019*

Acknowledgements

Professional

I want to thank my supervisors and everyone else involved for their contribution to my thesis, and for helping me navigate the different elements that came with it. Throughout my project I was able to obtain unique feedback and critical questions from these people, based on their unique expertise.

I want to thank Federico Pettazzi for our weekly meetings and day-to-day supervision in the first two months at TNO, as well as for his expertise in the field of optics, system design and TOmCAT.

I want to thank Jan de Vreugd for our weekly meetings and day-to-day supervision for most of my time at TNO, as well as for his expertise in the field of (thermo-)mechanical analysis and the supervision of master students.

I want to thank Lennino Cacace for our bi-weekly meetings with the OM student group at the TU Delft, and our meetings at TNO, as well as for his expertise in the field of opto-mechatronics.

I want to thank Fabrizio Silvestri for our meetings and discussions at TNO, as well as for his expertise in the field of optics and the Bulk Multiplexer.

I want to thank the OM student group (Alok Bharadwaj, Arnold Smolders, Martin van Mierlo, Robbert Kleer and Suzanne van den Boogaart) for our bi-weekly meetings at the TU Delft, as well as for their feedback, interesting discussions and friendship.

I want to also thank the other students in my office (Arnold Smolders, Berend Gort and Martin Kooper) for their feedback, interesting discussions and friendship.

I want to thank Pieter Kappelhof and Will Crowcombe for their roles in setting up my graduation project, as well as for their occasional support throughout the project.

I want to thank Jan Nijenhuis for organising the weekly mechanical meetings at TNO, thus increasing my general knowledge and understanding.

I want to thank Martin Eschen and Jos Groote Schaarsberg for their help in setting up my lab setup.

And I want to thank Wim Korevaar for his expertise on wireless communication. Despite finishing my spectral analysis months before he started at TNO, I did manage to include his feedback.

Personal

Furthermore, I want to thank my friends and family for their support throughout this past year. They gave me a chance to tell and refine my story to laymen throughout the year, as well as the much needed distractions from my work.

A special thanks to my parents (Ben and Marjet), my brother (Barnie) and my sisters (Judi and Tinka and their husbands and children) for their (financial) support, love and time, as well as for their much needed prayers and kind confrontations.

I also want to thank my local church (Shelter Haarlem) and youth group (Wild Saints), for providing me with an abundance of love, wisdom, identity and friendship, as well as for giving me the opportunity to pursue my other great passion in life: music.

And last but not least, I want to thank God for His love, kindness, goodness and personal guidance throughout my life. He has given me an appetite for the impossible, for compassion and for peace. He has always been my motivation to pursue a greater quality of work than expected from me, all the while giving me the means to do so by providing me with a sense of greater purpose, a sense of belonging, divine inspiration (eureka moments) and a sound mind.

Nomenclature

Abbreviation	Full term	Definition
AO	Adaptive optics	The field of optics where the optical properties or geometries can be controlled in order to achieve better performance.
BER	Bit error rate	The amount of bits per second that are received incorrectly.
CBC	Coherent beam combining	General term referring to technologies that combine laser beams while controlling their relative phase.
COTS	Commercially off-the-shelf	Referring to components that are nominally in stock at its supplier in anticipation of a recurring demand (as apposed to custom components, which are made based on a specific order).
DM	Deformable mirror	A mirror that can be deformed locally using actuators, in order to compensate for potential wavefront errors.
DOF	Degree of freedom	One of the six independent directions of motion in a 3 dimensional space. These six are: translation along, and rotation around the orthogonal X, Y and Z axes.
DQPSK	Differential quadrature phase-shift keying	Modulation scheme where bits are represented in four stages as the difference in phase between the current time block and the previous.
FEM	Finite element method	A computing technique where a geometry is divided into a mesh of smaller elements. The equations are solved iteratively for each element until the solution converges.
FSM	Fast-steering mirror	Mirror mounted on an active tip/tilt alignment mechanism with a relatively high control bandwidth.
FSO	Free Space Optical (communication)	Communication using optical frequencies where the light propagates in free space, rather than through fibers.
GEO	Geosynchronous Equatorial Orbit	Also known as geostationary orbit, is where the satellite orbits the earth on a specific altitude (35,786 km above the equator) where the orbital velocity of the satellite is equal to the spin velocity of the earth. As such, the satellite does not move relatively to the ground. Note that this is only possible above the equator.
HD	High definition	Display resolution of 1280×720 pixels.

Abbreviation	Full term	Definition
IBC	Incoherent beam combining	General term referring to technologies that combine laser beams without controlling their relative phase.
IF	Infra-red frequency	Frequency belonging to the infra-red frequency range (300 GHz - 430 THz) of the electromagnetic spectrum.
ITU	International Telecommunication Union	Specialized agency of the United Nations, that aims to regulate all international telecommunication to prevent interference and ensure availability of frequency band to international users.
IRT	Index of refraction turbulence	Phenomenon where the atmospheric index of refraction varies locally due to temperature differences and turbulence.
LED	Light-emitting diode	Electronic component that emits light.
LEO	Low-earth orbit	The orbital region closest to earth, with altitudes below 2000 km.
LHPC	Left-hand circularly polarized	Referring to light that has a polarization that rotates in a direction opposite to the one defined by the right-hand rule.
MZM	Mach-Zender modulator	Controllable optical component that introduces a phase shift based on the applied voltage.
OFL	Optical Feeder Link	An optical beam that is aligned to the receiving terminal and is modulated to transmit information.
OGS	Optical Ground Station	Telescope facility with the capability of sending and receiving an optical beam.
OGT	Optical Ground Terminal	Part of the optical ground station, consisting of the optical design but excluding the main structure (such as walls).
OOK	On-off keying	A modulation scheme where the signal is low to represent a 0-bit and high to represent a 1-bit.
PAA	Point-ahead angle	The angle between the incident and outgoing beam in satellite or ground station. This angle is non-zero due to the time delay caused by the finite speed of light.
PSD	Power spectral density	Plot with the frequency on the horizontal axis and the amount of power per frequency on the vertical axis.
RF	Radio frequency	Frequency belonging to the radio frequency range (20 kHz - 300 GHz) of the electromagnetic spectrum.
RHCP	Right-hand circularly polarized	Referring to light that has a polarization that rotates in a direction defined by the right-hand rule.
RMS	Root-mean-squared	Variation of a parameter calculated as the root of the sum of the squared differences with the average/mean. Also corresponds to the 1σ value of a normal/Gaussian distribution.

Abbreviation	Full term	Definition
TNO	Nederlandse Organisatie voor Toegepast Natuurwetenschappelijk Onderzoek	Dutch technological institution with a variety of specialisations in different locations across the Netherlands. In this thesis, the name TNO is used to refer to the location of Delft Stieltjesweg which houses both an Opto-Mechatronics and Optics department.
TOmCAT	Terabit Optical Communication Adaptive Terminal	TNO project which this thesis is part of. The project aims to establish a ground-to-GEO optical communication link with a data rate of at least 1 Tbit/s.
TTS	Tip/tilt sensor	Sensor designed to measure the tip/tilt alignment of an incoming beam.
VC	Vibration Criteria	Standard used for specifying vibration spectra.
WBC	Wavelength beam combining	General term referring to technologies that combine laser beams by using the wavelength dependency of optical phenomena.
WFS	Wavefront sensor	Sensor designed to reconstruct the wavefront of an incoming beam.

Contents

1	Introduction	1
1.1	Technical background	1
1.2	Research objective	1
1.3	Thesis structure	1
1.4	Supporting document	2
I	Literature Survey	3
2	Laser Communication	4
2.1	Introduction	4
2.2	Motivation for laser communication	4
2.2.1	Increased data rate	4
2.2.2	Less divergence	6
2.2.3	Driver for technology development	7
2.3	Challenges for laser communication	7
2.3.1	Pointing accuracy	7
2.3.2	Point-ahead angle	8
2.3.3	Index of refraction turbulence	9
2.3.4	Atmospheric transmittance	10
2.3.5	Other atmospheric losses	11
2.3.6	Background radiation	11
2.4	State-of-the-art of laser communication	12
2.4.1	European Data Relay Satellite	12
2.4.2	Lunar Laser Communication Demonstration	13
3	Bulk Multiplexer	14
3.1	Introduction	14
3.2	Wavelength beam combining	15
3.2.1	Combination using wavelength dependency of refraction	15
3.2.2	Combination using the wavelength dependency of interference orders	17
3.2.3	Combination using the wavelength dependency of reflectance	28
3.3	Proposed design challenge	29
3.4	Thermo-mechanical challenge	30
4	Alignment Mechanisms	33
4.1	Introduction	33
4.2	Alignment features	33
4.2.1	Resolution	33
4.2.2	Range	34
4.2.3	Actuation	34
4.2.4	Guiding	36

4.2.5	Locking stability	37
4.2.6	Thermal stability	39
4.2.7	Creep stability	39
4.2.8	Stiffness	39
4.3	State-of-the-art	40
4.3.1	GAIA collimator mount	40
4.3.2	GAIA fine mirror mount	40
4.3.3	Elastic lever mirror mount	41
4.4	Design parameters overview	41
II Design		43
5	Conceptual Design	44
5.1	Introduction	44
5.2	Single lever concept	44
5.3	Stiffness ratio concept	48
5.4	Lever ratio concept	51
5.5	Double wedge concept	52
5.6	Concept choice	55
5.6.1	Locking stability	55
5.6.2	Thermal stability	55
5.6.3	Conclusion	56
6	Detailed Design	57
6.1	Introduction	57
6.2	Double wedge concept	57
6.2.1	Single collimator design	57
6.2.2	Breadboard design	59
6.2.3	Material selection	61
6.3	Lever ratio concept	61
6.3.1	Spark erosion design	61
6.3.2	Rapid prototyping design	63
6.3.3	Material selection	66
7	Stability Analysis	68
7.1	Introduction	68
7.2	Thermal gradients	68
7.3	Vibration stiffness	71
7.4	Locking drift	72
7.5	Screw play	73
7.6	Back-scatter analysis	74
III Validation		76
8	Prototype	77
8.1	Introduction	77
8.2	Printed parts	77
8.3	Adjustment screws	79
8.4	Mechanism assembly	79

9	Test setup	83
9.1	Introduction	83
9.2	Collimator dummy	84
9.3	Auto-collimator	84
9.4	Double mirror alignment	86
9.5	Electric heat dissipation	88
9.6	Assembling three mechanisms	89
9.7	Stability	90
10	Test Results	92
10.1	Introduction	92
10.2	Range and cross-talk	92
10.3	Resolution and locking	93
10.4	Thermal stability	95
11	Discussion	98
11.1	Introduction	98
11.2	Lessons learned from prototype	98
11.2.1	Rapid prototyping tolerances	98
11.2.2	Assembling challenges	98
11.2.3	Locking drift	99
11.2.4	Hysteresis in cross-talk	99
11.2.5	Heat source	99
11.2.6	Mounting to table	99
11.3	Match between simulation and measurements	99
11.3.1	Conductance collimator dummy	99
11.3.2	Thermal contact resistance	100
11.3.3	Lower achieved heat load	100
11.4	Updated model for final design	100
12	Conclusions and recommendations	102
12.1	Conclusions	102
12.1.1	Literature survey	102
12.1.2	Design	102
12.1.3	Validation	103
12.2	Recommendations	103
12.2.1	Replace rings	103
12.2.2	Reduce heat load	103
12.2.3	Remove lever ratio	103
12.2.4	Beam steering	103
IV	Appendices	104
A	Divergence	105
B	Grating interference	111

Chapter 1

Introduction

1.1 Technical background

The worldwide internet traffic demand in 2022 is projected to be 4.8 Zetabytes in total [1]. This translates to an average data rate of over 1200 Terabits per second. A fifth of this data (thus 240 Tbit/s) would be transmitted using mobile networks. One of the technologies used for this is radio frequency (RF) telecommunication, but this technology is reaching its limits. Despite ongoing development, typical data rates are still in the order of Gbit/s per link [2].

TNO is working on a telecommunication link that can reach data transfer rates of over 1 Tbit/s [3]. The high data rate is achieved by using a very promising alternative to RF telecommunication: optical telecommunication. This technology uses infra-red frequency (IF) lasers, and is therefore also known as laser communication.

The telecommunication system that TNO proposed is called Terabit Optical Communication Adaptive Terminal (TOMCAT), and uses adaptive optics to establish a bi-directional ground-to-satellite optical feeder link [3].

In order to reach the intended data rates, the data needs to be spread over multiple optical frequencies. The signals then need to be combined into one transmitted beam using an optical bulk multiplexer. If the frequencies are sufficiently far apart, they can be separated at the satellite, based on their frequency [3].

The laser beams that are transmitted by their collimators need to be aligned with a high accuracy with respect to each other in order to reach the satellite as one beam. However, the footprint available for these alignment mechanisms is very limited. Furthermore, the system needs to achieve a good thermal and mechanical stability in order to meet the strict specifications.

1.2 Research objective

The aim of this thesis is two-fold: to show the need for achieving state-of-the-art alignment specifications with strict footprint constraints, and to defend the steps taken to achieve these requirements.

To achieve the first aim, the design process leading up to the required design challenge is presented, ranging from the highest to the lowest level design choices. The performed trade-offs and calculations are reviewed or expanded upon using original models, in order to gain a deeper understanding of the theory and possibly spot any errors.

To achieve the second aim, the design process leading up to the final recommended design is presented, also ranging from high to low level design choices.

1.3 Thesis structure

The thesis is divided into three parts. The first part is focused on reviewing the literature about (and state-of-the-art of) laser communication (Chapter 2), the bulk multiplexer project (Chapter 3) and alignment mechanisms (Chapter 4).

The second part is focused on the opto-mechanical design process of the proposed alignment mechanism, moving from a trade-off between four different conceptual designs (Chapter 5), to a detailed design (Chapter 6), and ending with a stability analysis (Chapter 7).

The third part is focused on the experimental validation of the proposed design, thus presenting the manufactured prototype (Chapter 8), the used test setup (Chapter 9), the test results (Chapter 10) and ending with a discussion (Chapter 11) and conclusions and recommendations (Chapter 12).

1.4 Supporting document

This thesis comes with a supporting document, which will not be made public. The document presents a detailed analysis of the TOMCAT project, to provide a clear understanding of the background of the design challenge of this thesis and the design parameters that have led to the specifications used in this thesis.

Furthermore, the document presents a detailed analysis of the combined effects of dispersion, divergence and pointing errors on the remaining signal integrity at the satellite. This analysis was added to the scope of the thesis based on the TOMCAT analysis, and is concluded with three mitigation strategies for the suggested issues of the existing system design.

The document also presents a thermo-mechanical analysis of the collimators that need to be aligned, and concludes with an overview of alignment mechanisms found in internal literature. The three most relevant of these are also presented in Chapter 4 of this thesis.

Part I
Literature Survey

Chapter 2

Laser Communication

2.1 Introduction

This chapter presents the motivation for, and challenges and state-of-the-art of laser communication. These objectives are pursued using a set of three research questions.

- What motivates the development of laser communication?
- What challenges need to be considered for laser communication?
- What is the state-of-the-art of laser communication?

2.2 Motivation for laser communication

As mentioned in Section 1.1, the main motivation for laser communication is the need for an increase in data transfer rates. Since radio frequency (RF) communication has to deal with limited licensed bandwidth, a new technology is required to support it. This new technology (laser communication) also has some major added benefits compared to RF communication. Most of these benefits arise from the fact that the electromagnetic frequency is much higher for infrared waves, compared to RF waves (see Table 2.1). This allows for an increased data rate and less divergence of the waves.

2.2.1 Increased data rate

The limited data transfer rates for RF are due to frequency congestion: the theoretical limit for one RF telecommunication link is in the order of Gbit/s according to [2]. This is because there is a minimum channel spacing that increases for higher modulation rates. This can be understood from how the laser is modulated.

There are three main types of modulation, based on changing either the intensity, phase or frequency of a beam [4]. The simplest example of these is on-off keying (OOK). Here, the laser beam is either turned on or turned off in order to represent either a 1-bit, or a 0-bit, respectively. This is illustrated in Figure 2.1 for a 1 GHz RF beam modulated at 0.2 GHz, which is a fifth of the carrier frequency (the rule of thumb according to [5]). The signal can then be reconstructed by measuring the intensity during each 5 ns time block.

The issue becomes apparent when looking at the frequency domain of this signal, as shown in Figure 2.2. For an non-modulated beam the power spectral density shows a sharp peak at the carrier frequency. However, the power spectral density of a square wave (such as the modulation signal) is described by a sinc function, of which the first zero lies at the on/off frequency of that square wave. When modulating a sine wave, the sinc function and the narrow peak are combined, as shown in Figure 2.2. The power spectral density is a sinc function centered around the carrier frequency, and with its first zero at the carrier frequency plus/minus the modulation frequency.

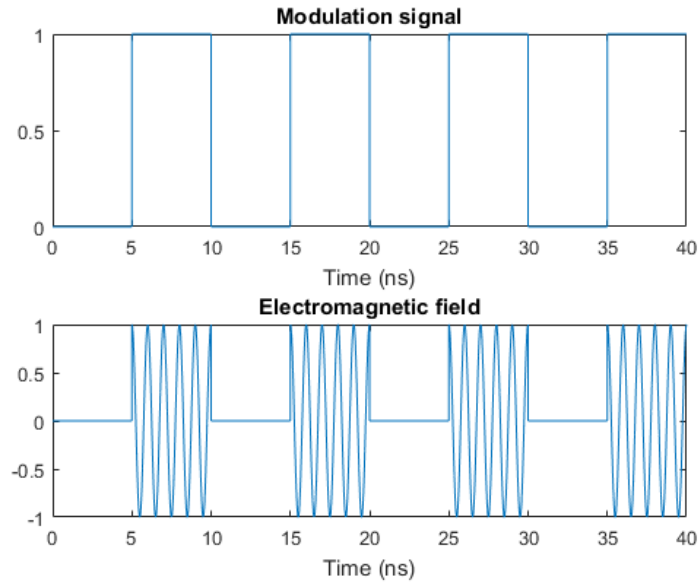


Figure 2.1: Modulation of a 1 GHz RF beam with a fifth of the carrier frequency.

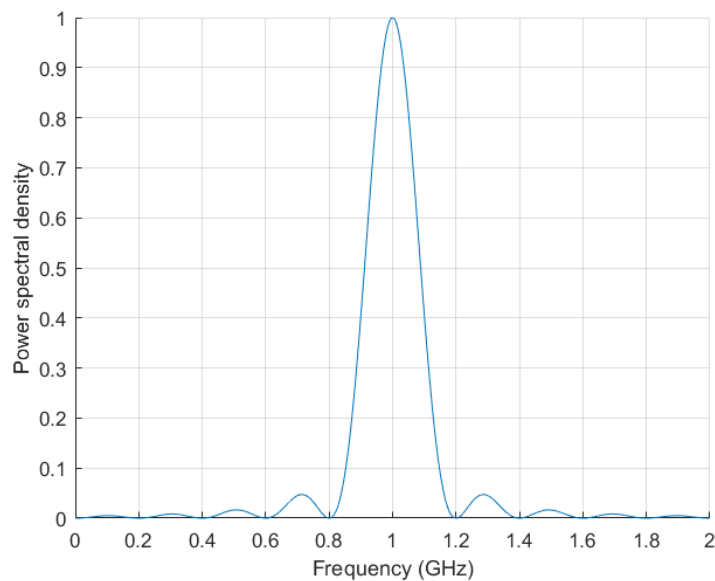


Figure 2.2: Normalized spectral density of a 1 GHz RF beam, modulated with 0.2 GHz, which is a fifth of the carrier frequency.

This issue of spectral spreading is the limiting factor for RF communication known as frequency congestion, since both the channel spacing and the data rate depend on the modulation frequency. The issue of channel spacing is illustrated in Figure 2.3. The spectral content of one channel leaks into the other channel. This makes it increasingly difficult to distinguish the channels as the channel spacing decreases.

The ratio between the modulation frequency and the channel spacing is chosen to be 1.25 in Figure 2.3. This is a tenth of a typical ratio recommended by the International Telecommunication Union (ITU) [6], which is 12.5. For the typical ITU ratio, the effect of spectral leaking is negligible.

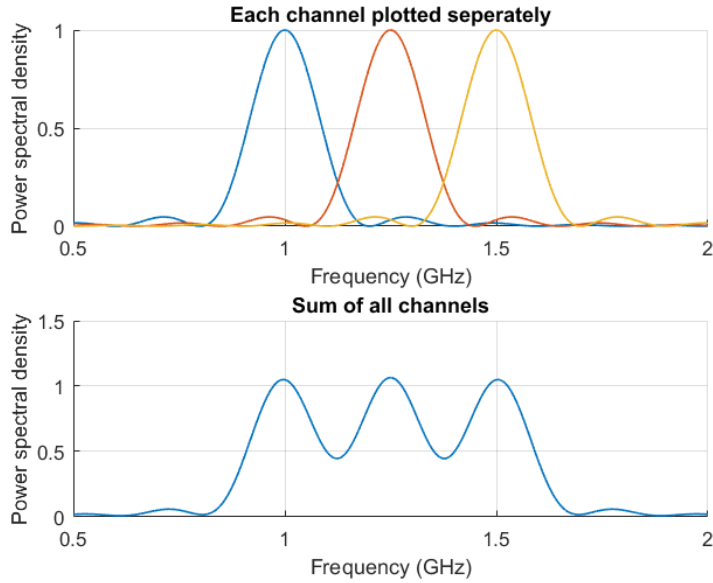


Figure 2.3: Spectral density of five RF beams, modulated with 0.2 GHz, which is a fifth of the first carrier frequency. The channel spacing is 0.25 GHz, which is a factor 1.25 higher than the modulation frequency.

Since for laser communication the carrier frequency is so much higher, this theoretical limit is not the limiting factor. The state-of-the-art modulators and detectors are not able to detect frequencies in the order of magnitude of laser frequencies, which is why for now the modulation rates are much less than a fifth of the carrier frequency.

2.2.2 Less divergence

An electromagnetic wave has the least divergence for a perfect Gaussian profile (for an in-depth analysis of divergence, see Appendix A). Therefore, the divergence calculated for a Gaussian beam can be taken as a theoretical minimum. The propagation of a Gaussian beam is determined by the wavelength and its starting diameter. In the case of satellite communication, this starting diameter is determined by the disc antenna diameter. Thus the divergence is given by the following equation [7]:

$$d = \Phi z = \frac{4 \lambda z}{\pi D} \quad (2.1)$$

Here, d is the far field diameter (in meters), Φ is the divergence angle (in radians), z is the propagation length, λ is the wavelength, and D is the antenna diameter. Thus, for an antenna diameter of 0.6 meters, and propagation to geostationary orbit (thus a propagation length of at least 35,786 km), the divergence angle and far field diameter are as presented in Table 2.1.

EM region	Frequency band	Wavelength band	Divergence angle	Far field diameter
Radio	1 - 40 GHz	7.5 - 300 mm	16 - 636 mrad	569 - 22766 km
Infrared	186 - 196 THz	1530 - 1610 nm	3.25 - 3.42 μ rad	116 - 122 m

Table 2.1: Minimum divergence angle and far field diameter for radio and infrared frequencies.

The considered radio frequencies are those used for satellite communication [8], and the considered infrared frequencies span the 1550 nm band shown in Section 2.3.4. It can be seen that the far field diameter can be over 5 orders of magnitude greater for radio frequencies, compared to infrared. This assumes that both the laser and the radio beams are perfectly pointed at the satellite.

This decrease in divergence has three main benefits. First of all, interference with other stations is more easily prevented. Whereas it might be unrealistic to place every RF station at least 569 kilometers apart, it

is not an issue to place the laser communication stations at least 122 meters apart.

This interference for RF communication is the reason that the RF bands are strictly regulated by a specialized agency of the United Nations: the International Telecommunication Union (ITU) [6]. Because it is not possible to aim a RF wave precisely at a specific target, different users use different bands within the RF spectrum to distinguish their signals. Because there is an ever increasing demand for RF communication, it is becoming ever more challenging to obtain/provide a license.

The second benefit of a smaller divergence is that there are less power losses: much more of the energy arrives at the intended location. Since the far field area scales with the square of the far field diameter, the beam divergence losses can be over 10 orders of magnitude greater for radio frequencies, compared to infrared.

Thirdly, the smaller divergence allows for a much more secure communication link. RF links can easily be intercepted, because the intended user would not notice a difference between that part of the beam being either intercepted or missing the target. For laser communication, however, the beam is so narrow that it becomes much more challenging to intercept. It is no longer sufficient to simply be in the area.

2.2.3 Driver for technology development

Although the main motivation for the development of laser telecommunication is for it to assist RF telecommunication, it can also assist other technologies. This is because the technology of Free Space Optical (FSO) communication (which is another term for laser communication) can also assist the widespread fiber optics communication system (thus serve as the “last mile” communication).

Even though fiber optics has many advantages, it might not always be worth it to invest in such a network. Once FSO technology is fully developed, a communication link can be set up relatively quick and easy, and at low recurring costs [9]. For instance, there is no need to build the cable infrastructure. It can be especially attractive for temporary networks, since the system is fully redeployable.

However, long-term networks can also benefit from FSO communication, because FSO links can serve as a back-up for fiber optic links. FSO links can also be attractive for military applications, when the communicating army does have control of the airspace, but not of the ground.

Finally, the development of laser communication technology is also beneficial for laser technology in general. For instance, some of the technologies that are envisioned and pursued on behalf of laser communication are: single-photon-sensitive detectors, efficient laser transmitters and low-cost large aperture receiving stations.

2.3 Challenges for laser communication

Even though the above-mentioned benefits motivate the pursuit of laser communication technology, there are also significant challenges, especially when the technology is pushed to its limits. The first of which arises from what was earlier stated as a benefit: the divergence. The other main challenges are due to the required atmospheric propagation.

2.3.1 Pointing accuracy

The smaller divergence of IR beams, compared to RF beams, causes the pointing stability requirements to increase significantly. As seen in Table 2.1, the divergence angle for IR beams is a few μrad . This also means that the beam needs to be pointed at the receiving satellite with a much better accuracy.

In fact, there is a trade-off to be made in the link budget of laser communication links. There is an optimal divergence angle for any given pointing error budget [3]. This is because increasing the divergence angle reduces the effect of missing the satellite, but at the same time increases the amount of power lost due to divergence losses. The result is that the pointing accuracy needs to be at least in the same order of magnitude as the divergence angle.

This pointing accuracy is so strict for laser communication that other effects become significant as well. One such effect is the point-ahead-angle.

2.3.2 Point-ahead angle

Suppose the satellite is placed in geostationary orbit, or geosynchronous equatorial orbit (GEO). This means that the angular velocity of the satellite is equal to the angular velocity of the equator of the earth. This is only possible when the satellite is located exactly above the equator. Because of this geostationary orbit, the satellite always appears at the same location in the sky.

However, when sending a light signal to this satellite, it takes some time for the light to arrive at the satellite. This time delay is 0.125 seconds (assuming a ground station latitude of 40° North). In this time, the satellite has moved 385 meters from where it was when the signal was sent. When the satellite then sends a signal back, it again takes 0.125 seconds to arrive at the ground station. So the time it takes for a signal to go up and back is 0.25 seconds in total. In this time the ground station has moved 89.1 meters. The time it takes for a signal to go down and then up is also 0.25 seconds, and in that time the satellite has moved 769 meters.

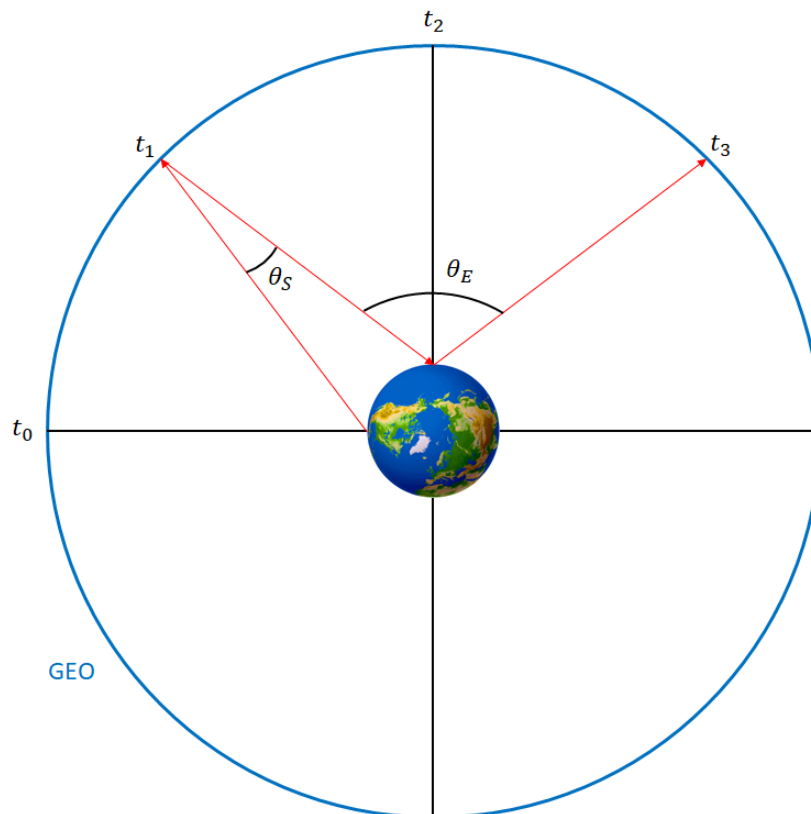


Figure 2.4: Greatly exaggerated visualization of the point-ahead-angle (PAA) for geostationary orbit (GEO). The PAA for the satellite is indicated with θ_S , and the PAA for the ground station is indicated with θ_E .

This effect is visualized in Figure 2.4 by greatly exaggerating the time delay. In this visualization, the time delay is 3 hours rather than 0.125 seconds. The signal is sent towards the satellite at t_0 and arrives at the satellite 3 hours later, at t_1 . The signal is sent back towards the ground station and arrives 3 hours later, at t_2 . Another signal is then sent to the satellite, which arrives there another 3 hours later, at t_3 . In this 9 hour time span, the earth has rotated 120 degrees around its axis, and the GEO satellite has rotated along with it.

The point-ahead-angle for the ground station is equal to $18.2 \mu\text{rad}$, which is almost 6 times the divergence angle. Therefore not accounting for the point-ahead-angle means completely missing the satellite. The point-ahead angle for the satellite is $2.38 \mu\text{rad}$.

2.3.3 Index of refraction turbulence

As mentioned in Section 1.1, the system proposed by TNO uses adaptive optics. This is because of a phenomenon called index of refraction turbulence (IRT) [10]. The index of refraction of the atmosphere is temperature-dependent, and the temperature of the atmosphere is continuously slightly changing both temporally and spatially. This is because the mass density of air is also temperature dependent, thus a package of warm air will rise up and mix with cooler air.

These packages with different indices of refraction are visualized in Figure 2.5. Every part of the beam takes a slightly different time to pass through the atmosphere, due to the fact that the indices of refraction vary slightly. As a result, a phase delay is induced within the beam, thus distorting the wavefront (which is a surface along which the phase of each beam is equal).

This phase delay is a function of the wavelength, the indices of refraction and the distances traveled through the different media. Therefore the same turbulence has a different effect on the number of radians delay that is induced, depending on the wavelength.

The phase delay causes the beam quality to decrease, which leads to losses in the telecommunication link. First of all, the distorted wavefront causes problems when focusing the received signal on the detector. This is because light propagates in a direction orthogonal to its wavefront [11]. So instead of all light being focused in the center of the detector, the light will spread across. This wavefront property of light also causes a phenomenon called beam wander: a beam propagating through a turbulent atmosphere will change direction slightly [10].

These IRT-induced problems can also be noticed in RF communication [12]. However, the phase distortion is much greater for infrared light because the wavelengths of infrared light are orders of magnitude smaller than the RF wavelengths.

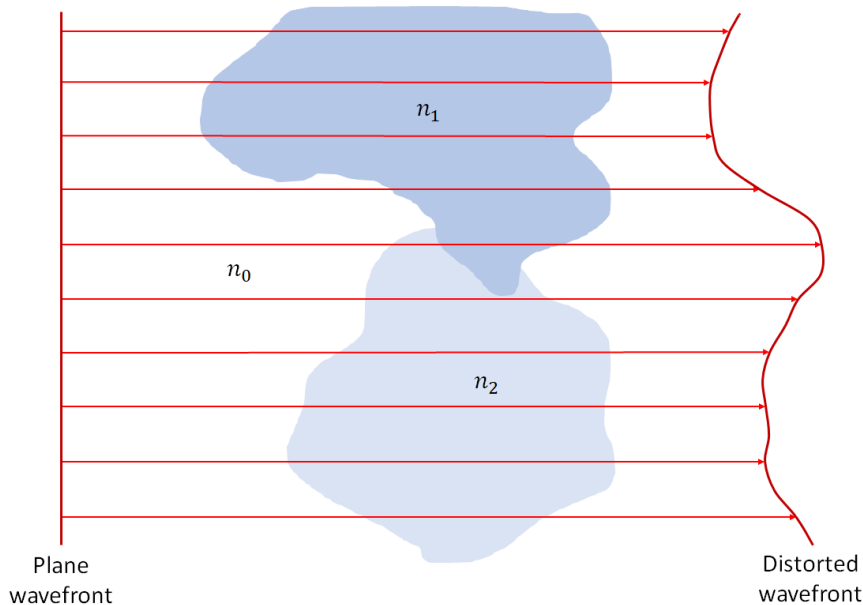


Figure 2.5: Visualization of index of refraction turbulence (IRT). Due to randomly varying indices of refraction (n_0 , n_1 , n_2), every part of the beam takes a slightly different time to pass through the atmosphere, thus turning a plane wavefront into a distorted wavefront through phase delay.

To cope with the wavefront distortion, the incoming beam needs to be split into three separate beams: one for the receiving channel, one for the tip/tilt correction, and one for the higher-order wavefront distortions.

The tip/tilt is measured separately, because these low-order aberrations are expected to be much greater than the higher-order aberrations [13]. This is due to the fact that a misalignment of the beam to the satellite will also cause tip/tilt aberrations. The tip/tilt is measured using a focusing lens with its focus on a position-sensitive photo-detector (the TTS). Any tip/tilt error will cause the position of the focus to shift, and this can then be corrected for using the fine-steering mirror (FSM).

The higher-order aberrations are measured using a Shack-Hartman WFS, see Figure 2.6. Light rays can be considered to travel in the direction orthogonal to its wavefront [11]. Therefore, when a distorted wavefront is sent through a set of micro-lenses, the lenses will focus every part of that beam to a focus point that depends on the local gradient of the wavefront.

This information can then be used to correct the wavefront with a deformable mirror (DM). Such a mirror can be locally deformed such that it matches the negative shape of the aberrated wavefront. Thus the optical path length is different for each part of the beam, such that a flat wavefront is obtained [13].

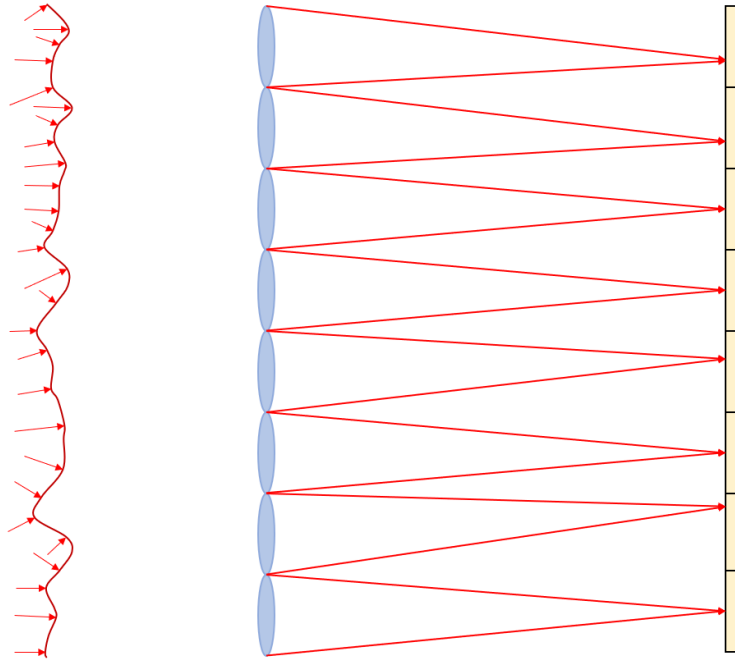


Figure 2.6: Shack-Hartman WFS.

2.3.4 Atmospheric transmittance

The transmittance of the atmosphere per wavelength is shown in Figure 2.7. This transmittance is limited by the absorption and scattering of light by the molecules present in the atmosphere.

As can be seen from the figure, the transmittance is generally lower for smaller wavelengths. This is because the effect of scattering becomes stronger as the wavelength of the light approaches the size of the molecule that scatters it. Since the atmospheric molecules are all smaller than 1 nm, these molecules scatter blue light more than red light. This is also the reason why the sky appears to be blue at day: this is due to the spectral distribution of the scattered light that reaches our eyes (since the wavelength of blue is smaller than that of red).

It can also be seen from the figure that there are multiple bands where the transmittance is very low. This is due to absorption. The contributions of three dominant absorbing molecules are shown along with the total transmittance. This absorption happens at specific wavelengths, because this effect comes from the interaction of the molecule energy states with the energy level of the photons.

This is why for IR waves there are only certain spectrum bands for which the transmittance is acceptable. A popular band for laser communication is the 1550 nm band. This is because the atmospheric turbulence induced wavefront disturbances are smaller for longer wavelengths (as mentioned in Section 2.3.3). Also, there is a good availability and development of the required components for space applications, and the laser eye safety restrictions are 50 times less strict [3, 5].

Even though the transmittance in this band is 70%, the available wavelengths in this band are limited by the atmospheric transmittance and the operational ranges of existing optical components. This poses a design limitation, as only a certain amount of channels fit within this band. As mentioned in Section 2.2.1, both the channel spacing and the data rate depend on the modulation frequency. Therefore the bandwidth

available in this band directly limits the data rate.

The atmospheric transmittance of RF waves is 100% throughout the RF spectrum. Therefore this challenge is unique for laser communication.

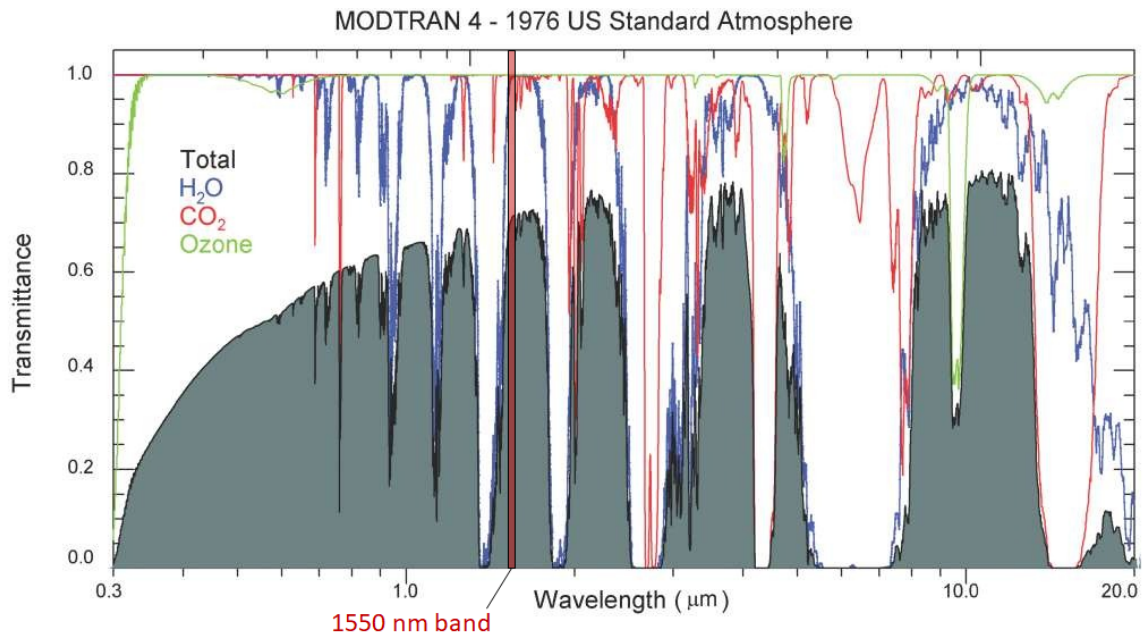


Figure 2.7: Transmittance of the atmosphere per wavelength, limited by absorption and scattering of light by the molecules present in the atmosphere. The contributions of three dominant absorbing molecules are shown along with the total transmittance [14]. The 1550 nm band is indicated in dark-red.

2.3.5 Other atmospheric losses

Scattering also occurs due to particles in the air, which exist in many different typical sizes. Such causes of scattering include (listed from large to small): rain, drizzle, mist, clouds/fog and smog [15]. The wavelengths of RF waves are approximately the size of raindrops, which is why RF communication can be disturbed by precipitation. The wavelengths of infrared (IR) waves are in the order of magnitude of clouds/fog and smog.

The combined effect of absorption and scattering is so severe, that an approach of site diversity is proposed [3]. Instead of relying on one ground station that can be temporally forced offline by cloud coverage, the approach is to select multiple site locations that have a combined online probability of 99.9%.

These site locations are chosen strategically, for instance because the atmospheric losses are greater at lower altitudes (due to thicker air) and in urban environments (due to exhaust gases). Since the satellites are placed in geostationary orbit (which is situated above the equator), it is also desired to choose site locations with a low latitude. There is however a trade-off to be made since remote locations require a longer fiber optic infrastructure.

2.3.6 Background radiation

Another challenge for laser communication is the background radiation. Infrared waves are not only emitted by the lasers, but also by the sun and by the earth. These other waves can interfere with the signal at the receiving end of the signal. This problem can be partially solved by making the signal circularly polarized, which allows for an attenuation of the background radiation of a factor 2 (or 3 dB).

For comparison, the detector sensitivity of the receiving channel is in the order of μW 's. The irradiance of the sun at sea level for a wavelength range of $1550 \pm 0.4 \text{ nm}$ is 0.184 W/m^2 . The power on a telescope is 46 mW , assuming a telescope area of 0.25 m^2 . With the polarization attenuation this is 23 mW . Therefore the solar irradiance is 5 orders of magnitude greater than the detector sensitivity.

When assuming an extreme average temperature of 50 °C for the earth, the irradiance of the earth on the satellite is still estimated to be 0.3 nW/m² (black-body radiation with an atmospheric attenuation factor of 0.7, for geostationary orbital radius). This is therefore 4 orders of magnitude smaller than the detector sensitivity and thus negligible. Note that this analysis is based on the detector sensitivity of the receiving channel. Pointing sensors can be more sensitive to background radiation because their detector sensitivity can be lower.

2.4 State-of-the-art of laser communication

Because of the presented advantages and challenges of laser communication, there have been numerous demonstrations, prototypes and proof-of-concepts developed and tested in the past few decades. The types of laser communication links show a great variety, ranging from inter-satellite to satellite-to-ground and ground-to-ground connections.

2.4.1 European Data Relay Satellite

One of the most recent inter-satellite laser communication links is between the Alphasat TDP1 GEO and Sentinel-1A low-earth orbit (LEO) satellites. Because the LEO satellite is not geostationary, the link distances vary significantly. Between 2014 and 2016, over 180 successful links have been established with link distances of up to 45000 km. The achieved bit error rate (BER) is less than 10⁻¹⁰, for a laser power of 1.1 W and a data rate of 1.8 Gbit/s. This BER leaves a large margin for increasing the data rate, and a scaling to 7.2 Gbit/s is already envisioned [16].

This envisioned data rate is still much lower than the 1 Tbit/s aimed for by the T0mCAT project. Also, the acquisition time is much greater, with the worst achieved time being 55 seconds, and the best 19 seconds. Of this 19 seconds, 7 are required for spatial acquisition. This is required because there is always some uncertainty as to where the satellite is exactly. The spatial acquisition is done by dithering within the cone of uncertainty with a laser and measuring the laser beam at the receiving satellite. This satellite then sends back a laser beam which is measured at the transmitting satellite. This feedback is used in a feedback loop in a process called pointing, acquisition and tracking (PAT). The other 12 seconds are used for frequency acquisition. This is done by matching the frequency of the receiving satellite oscillator to that of the transmitting satellite oscillator.

Since this link is inter-satellite, it is not bothered by atmospheric disturbances. However, for low grazing altitude (meaning the LEO satellite is close to the horizon as seen from the GEO satellite), the impact of the atmosphere on the link performance was observed.

The data obtained from the Alphasat TDP1/Sentinel-1A link was used for the European Data Relay Satellite (EDRS) system. This is a system where multiple GEO-satellites are used to relay data from LEO-satellites to the ground, in cases where the LEO-satellites are not able to send the data directly to the ground.

The LEO-GEO links in the EDRS system achieves a similar performance to the Alphasat TDP1/ Sentinel-1A link. The LEO-LEO links achieves a lower data rate, 5.625 Gbit/s, for smaller link distances (< 5100 km), but also a third of the transmitted power [17, 18].

The bottleneck of the EDRS system is identified to be in the RF link between the GEO-satellites and the ground stations. The achieved data rate for this RF link is only 600 Mbit/s, which is why a laser communication link would be interesting. Even though there has been a successful optical LEO-ground link, the optical GEO-ground link is still being developed. This is because the GEO-ground link requires adaptive optics (AO), whereas the LEO-ground link does not.

This can be understood from the longer link distance. Due to divergence, the LEO-ground link requires a 60 mm diameter aperture, whereas the GEO-ground link requires a 200 mm diameter aperture. In combination with the Fried parameter (which describes the typical size of the atmosphere within which the index of refraction can be considered more or less constant), this means that the 60 mm aperture has a more or less constant incoming phase, while the 200 mm aperture has significant distortions [17].

2.4.2 Lunar Laser Communication Demonstration

In 2013, NASA performed the Lunar Laser Communication Demonstration (LLCD), which established an optical link between ground stations and a satellite on lunar orbit [19]. This shows that laser communication can be used for extremely large distances (approximately 384,400 km). The maximum data rate that was achieved was 622 Mbit/s.

The used satellite telescope diameter is 100 mm, which would give a divergence angle of 5 μ rad for a perfect Gaussian beam without beam spread/wander. The achieved divergence angle is 15 μ rad instead. The laser power from moon to ground is 0.5 W.

The ground terminal telescope is an array of four 150 mm telescopes for uplink, and four 400 mm telescopes for downlink. The uplink laser power is 10 W.

Chapter 3

Bulk Multiplexer

3.1 Introduction

As mentioned in Section 1.1, the main focus of this thesis is on a laser communication subsystem developed by TNO. This subsystem is called the bulk multiplexer, and is initially intended to be part of a new optical ground station, see Figure 3.1. The bulk multiplexer needs to combine multiple laser beams into one beam, such that they can be projected unto sky using the proposed telescope design.

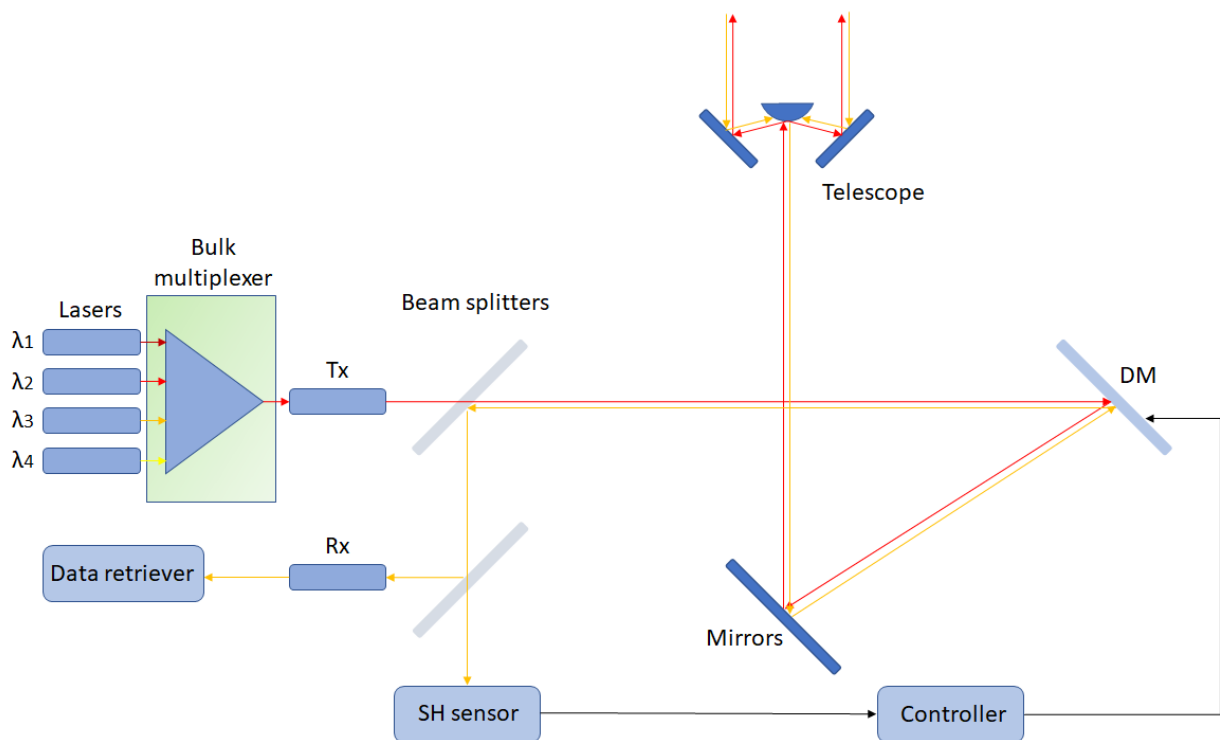


Figure 3.1: Bulk multiplexer as a subsystem of an optical ground station.

This chapter presents the main concepts considered for the bulk multiplexer, the optical design of this subsystem, and a thermo-mechanical issue with the chosen concept, thus answering the following research questions:

- How does wavelength beam combining work in general and what concepts exist?
- What is the proposed design challenge within the bulk multiplexer project?
- How can thermal deformations influence the optical performance of the bulk multiplexer?

3.2 Wavelength beam combining

Three main types of beam combining exist: incoherent beam combining (IBC), coherent beam combining (CBC) and wavelength beam combining (WBC). In order to be compliant with the rest of the optical/system design, the beams should have the same polarization and should already overlap in the near field. These restrictions rule out the IBC and CBC concepts. Therefore only WBC concepts are considered for the bulk multiplexer project.

There exist three main types of WBC, based on the wavelength dependency of either refraction, interference orders or reflectance.

3.2.1 Combination using wavelength dependency of refraction

The wavelength dependency of the index of refraction is well known, as it is the driving phenomena of rainbows. A rainbow is created by splitting white light (consisting of many different wavelengths) into its separate wavelengths. This effect can however also be reversed to combine different wavelengths into one beam, as shown in Figure 3.2.

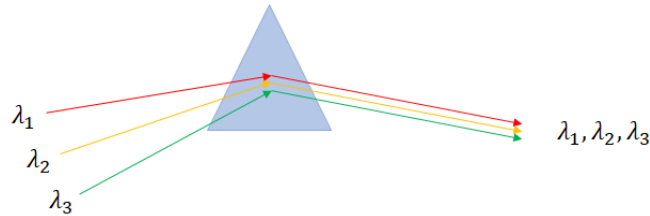


Figure 3.2: Wavelength beam combining using a prism.

The index of refraction of a material is determined by the phase velocity of light in that material. This velocity is limited because the photons excite the electrons of the material into a higher energy state, after which the electrons return to a lower energy state and release a photon again. This causes a phase delay for each photon, and thus causes the overall phase velocity to reduce.

This phase delay is wavelength dependent, and so the index of refraction is wavelength dependent. When taking a fused-silica glass as an example (see Figure 3.3), the index of refraction n within the 1500-1600 nm wavelength (λ) range can be linearized to the following equation [20]:

$$n(\lambda) = 1.4446 - 1.2 \cdot 10^4(\lambda - 1500 \cdot 10^{-9}) \quad (3.1)$$

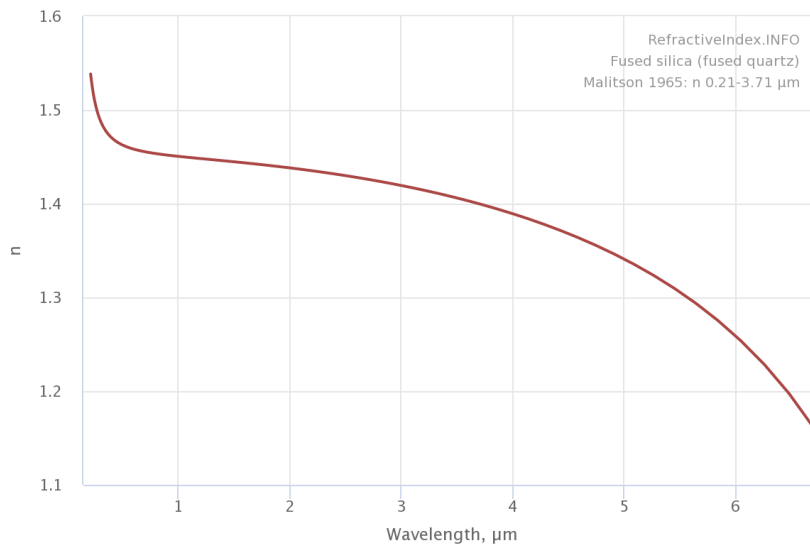


Figure 3.3: Index of refraction of a fused-silica glass example [20].

When taking a simple prism as shown in Figure 3.4, the refracted angles θ'_0 and θ'_1 can be calculated from Snell's law, and the angles of interest θ_1 and θ_2 can be derived using trigonometry:

$$\begin{aligned}\theta'_0 &= \arcsin\left(\frac{1}{n} \sin \theta_0\right), & \theta_1 &= \alpha - \theta'_0 \\ \theta'_1 &= \arcsin(n \sin \theta_1), & \theta_2 &= \theta'_1 - \alpha\end{aligned}\tag{3.2}$$

Where n is the refractive index of the prism. Since this refractive index is wavelength-dependent, different wavelengths are refracted at different angles. When taking a prism with an apex angle α of 30° , and an incidence angle θ_0 of 15° , the achieved dispersion is $7 \mu\text{rad}/\text{nm}$ (see Figure 3.5). This is 2 orders of magnitude smaller than the intended dispersion. Therefore the use of a prism with this geometry would require a 100 times greater wavelength dependence of the index of refraction.

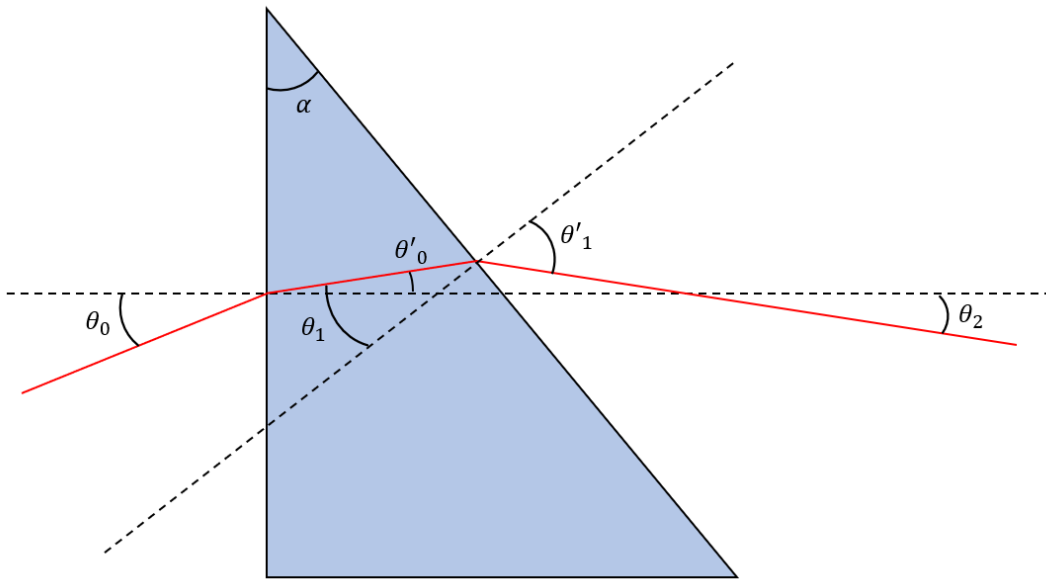


Figure 3.4: Angle definitions for a prism.

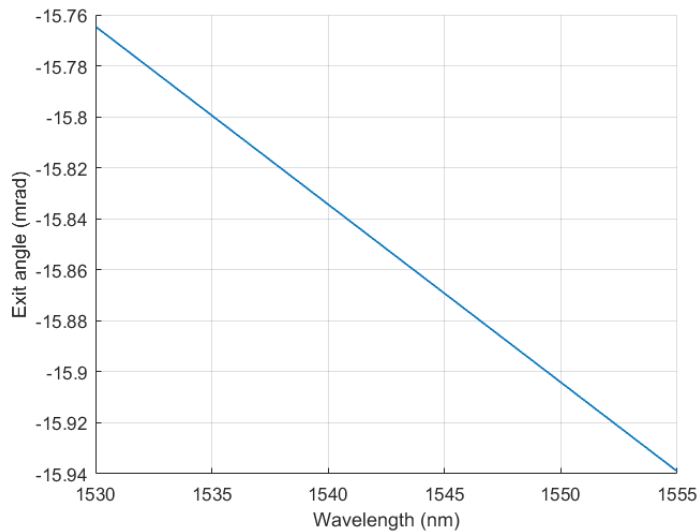


Figure 3.5: Dispersion of the prism shown in Figure 3.4, with an α of 30° , and θ_0 of 15° .

3.2.2 Combination using the wavelength dependency of interference orders

The second concept available for wavelength beam combining uses an interference grating to combine the different wavelengths into one beam in the -1th interference order, see Figure 3.6.

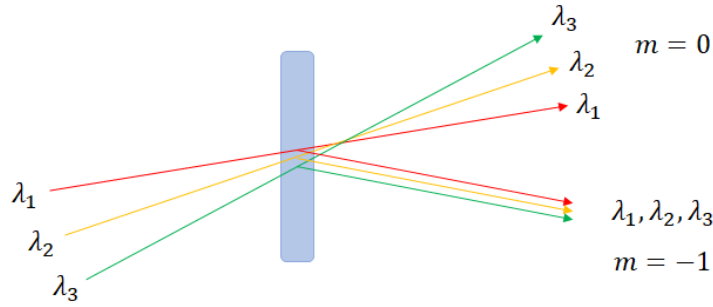


Figure 3.6: Wavelength beam combining using an interference grating.

The wavelength dependency of interference orders can be understood from Figure 3.7, showing the general concept of interference. Light waves can either interfere constructively or destructively, depending on the phase shift between those waves. When this phase shift is a multiple of 2π , the waves interfere constructively, and when the phase shift is a multiple of 2π with an extra π shift, the waves interfere destructively.

When two coherent sources are placed next to each other, these specific phase shifts are achieved at specific locations, because the phase shifts are related to the wavelength of the light. When the optical path length from one source to a point in space is exactly a multiple of the wavelength λ longer than the optical path length from another source to that same point, the waves from these two sources constructively interfere at that point. This is what is shown in Figure 3.7.

The angle at which this constructive interference is achieved is thus wavelength dependent, and given by the following equation:

$$\sin \theta_m = \frac{m\lambda}{d} \quad (3.3)$$

Where m is the interference order, d is the spatial separation of the grating apertures, and θ_m is the constructive interference angle for the m th order. The first order constructive interference angle is plotted against the wavelength range in Figure 3.8. It can be seen that this dispersion can be considered linear for this range. The spatial separation d was tuned to $2.1 \mu\text{m}$, which gives the targeted dispersion coefficient of $700 \mu\text{rad}/\text{nm}$ (the derivative of the plot in Figure 3.8).

The first order constructive interference angle for this value of d is 47.6° . This is confirmed by the interference pattern plotted in Figure 3.9. This figure shows the field intensity at one specific time stamp, where d is $2.1 \mu\text{m}$, and λ is 1550 nm . The fields are plotted for 1, 3, 5, 6 and 7 sources in Appendix B, showing that the angular width of the orders decreases as the amount of sources increases. The sources are placed in the origin, and are spatially separated in the y -direction.

Note that for this configuration there is no second order, since Equation (3.3) would lead to complex angles for $m > 1$. This allows for less losses in the system, since a larger portion of the light is projected into the first order.

The grating can also be optimized to achieve a maximum grating efficiency in the first order. Such an optimized grating is called a blazed grating. Here, the grating is designed as a saw-tooth profile with a blaze angle θ_B of 21.7° according to the following equation:

$$\theta_B = \arcsin \frac{m\lambda}{2d} \quad (3.4)$$

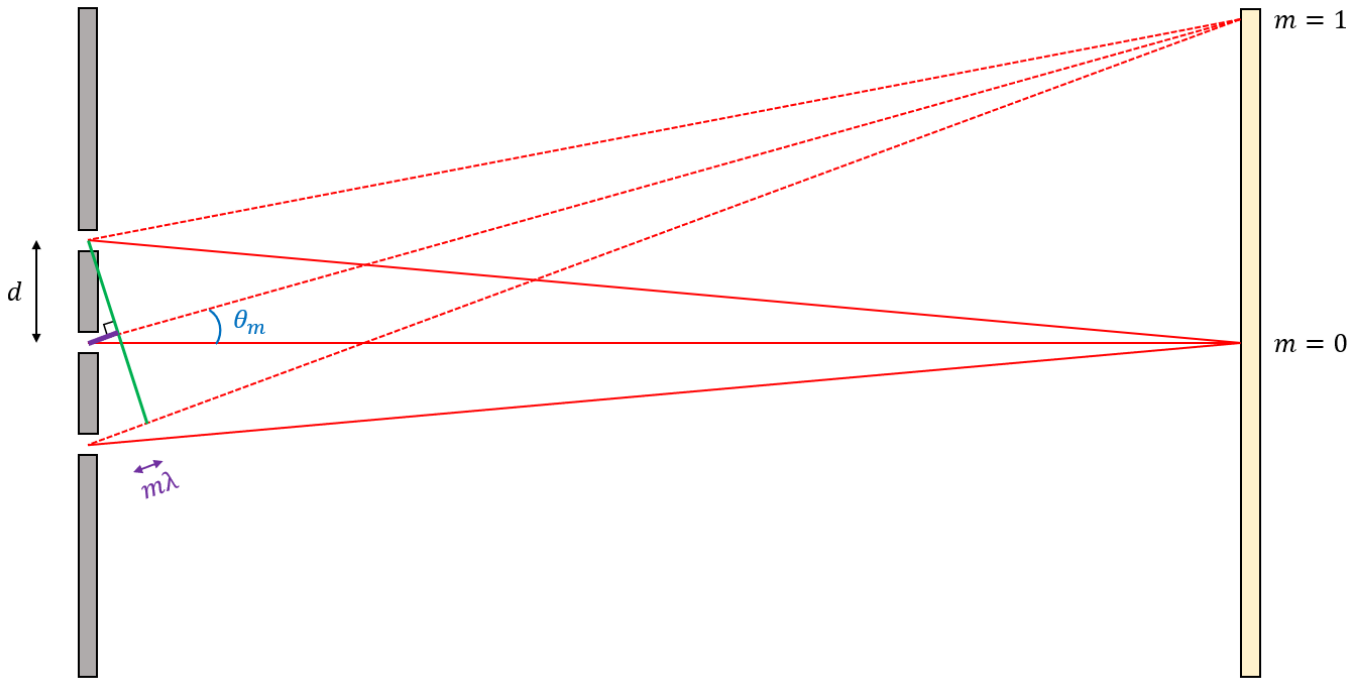


Figure 3.7: Constructive interference after a diffraction grating.

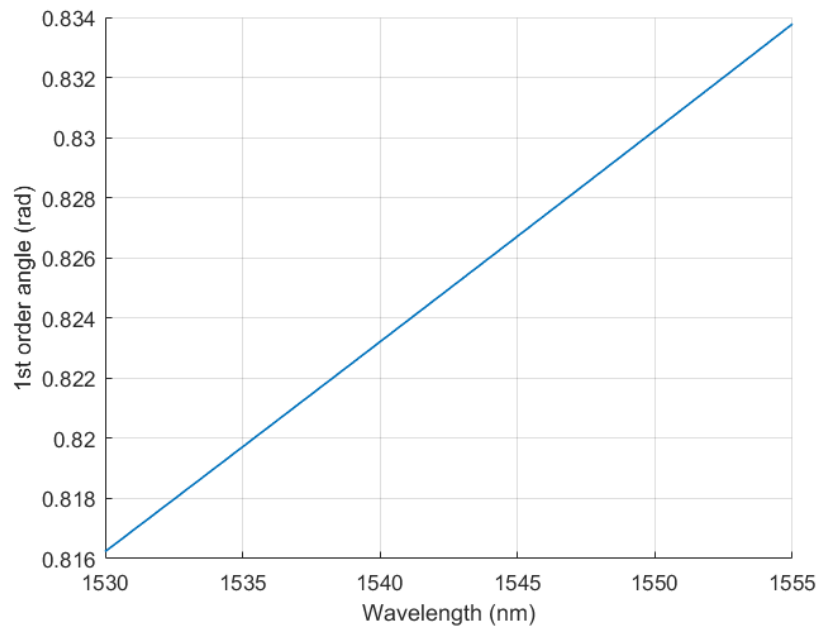


Figure 3.8: First order constructive interference angle as a function of the wavelength.

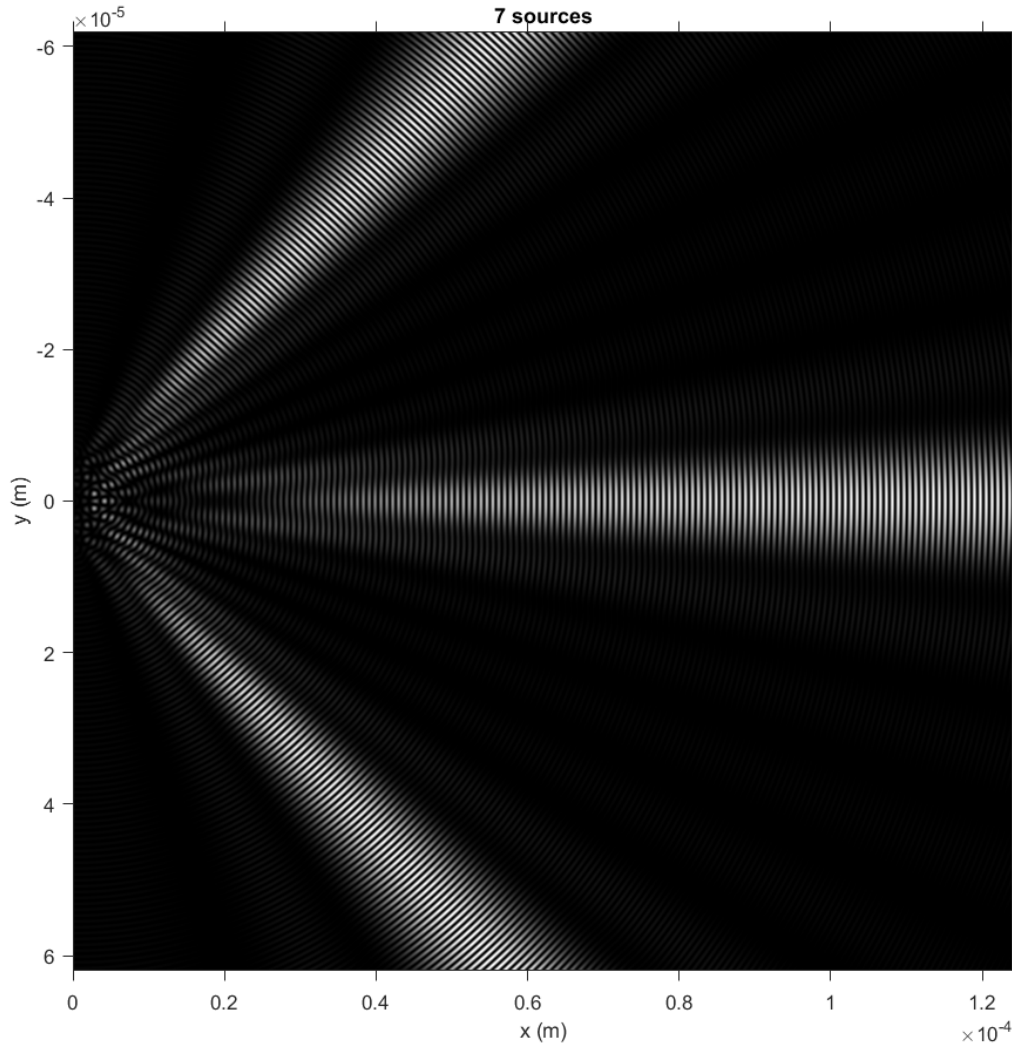


Figure 3.9: Intensity distribution for 7 sources, at one time frame. The 0th order can be distinguished as the horizontal beam around $y = 0$. The +1th and -1th orders can be distinguished as the diagonal beams moving up or down from the 0,0 point.

The theoretical grating presented in Figure 3.7 is an amplitude grating, meaning that the interference pattern is a result of local amplitude differences. This inherently comes with limited efficiency, because approximately half of the light is blocked by the grating [21].

The gratings considered for the bulk multiplexer are phase gratings, meaning the interference pattern is a result of local phase differences. Again, there are two options: reflection gratings and transmission gratings, of which the latter are chosen for the bulk multiplexer.

Reflection grating

As the name suggests, a reflection grating reflects the light after which the interference patterns result in diffraction and dispersion. The interference pattern results from the differences in optical path length induced by the grating pattern. This grating pattern is often a saw-tooth profile with a certain spatial separation d . The optical path difference is then equal to $d(\sin \theta_i - \cos \theta_m)$, where θ_i is the incidence angle and θ_m is the diffraction angle.

As mentioned in Section 3.2.2, constructive interference occurs when the optical path difference is equal to a multiple of the wavelength λ , and thus Equation (3.3) for an arbitrary incidence angle becomes:

$$\sin \theta_m = \sin \theta_i - \frac{m\lambda}{d} \quad (3.5)$$

The maximum multiplexing efficiency is achieved for the special Littrow/blaze angle, see Equation (3.4). This is in part because when the incidence angle is equal to this blaze angle, only the -1 -th and 0 -th order are reflected. This does assume that the ratio λ/d is between $2/3$ and 2 [21]. For a wavelength of 1550 nm, these ratio boundaries translate to grating resolution boundaries of 1290 and 428 lines/mm.

The other reason that the efficiency is maximized for this blaze angle, is that for this blaze angle the light has a normal incidence on the saw-tooth profile because this profile is made with this same blaze angle. Therefore the light is reflected in the direction from which it came, which is also the direction of the -1 -th order, see Figure 3.10. Since the light is reflected in the direction of the -1 -th order, the efficiency is optimized.

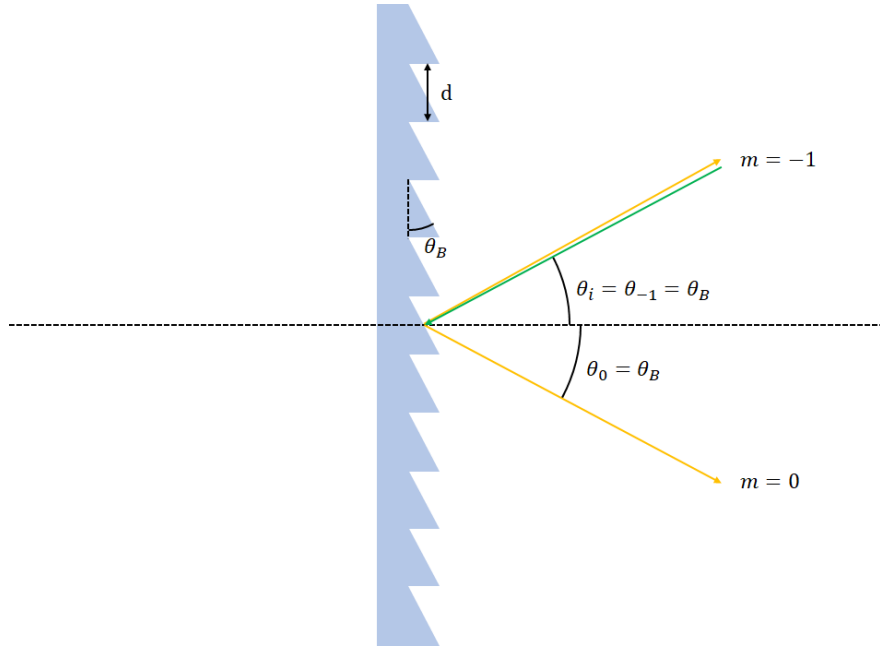


Figure 3.10: Reflection grating optimized for its blaze angle θ_B . θ_0 and θ_{-1} are the 0 -th and -1 -th order diffraction angles, respectively.

The optical path difference for a blaze angle configuration is illustrated in Figure 3.11. This optical path difference is equal to $2d \sin \theta_B$ in the direction from which the light comes. Since this optical path difference should be equal to a multiple of λ , Equation (3.4) can be derived from this illustration.

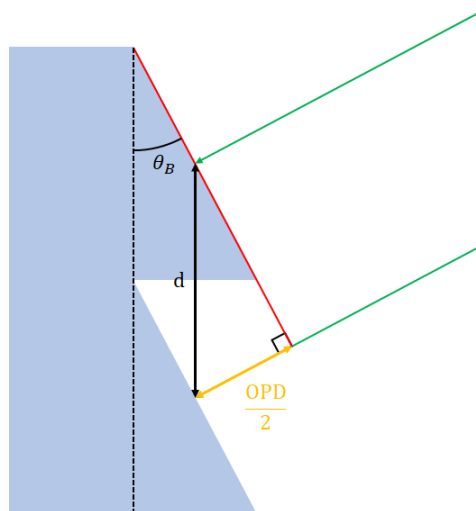


Figure 3.11: Illustration of the optical path difference (OPD) in a reflection grating.

Transmission grating

The presented blaze angle configuration can optimize the efficiency of the -1 -th order, but in reality there is always some spatial separation required between the incident and diffracted beam. Therefore transmission gratings are more suitable for multiplexing applications, because for transmission gratings the incident beam is on the other side of the outgoing beam.

A transmission grating for normal incident light is shown in Figure 3.12. The principle of this grating can be understood from Figure 3.7, because the same equations apply. Again, the light is split into many spatially separated point sources, and these point sources interfere to form the interference orders in the far field.

However, in this case there are two sets of point sources. The first set originates from the tips of the grating, while the other set originates from between these tips. The point sources that originate from the tips have traveled an extra distance h (which is the height of the grating tips) through the glass, which gives them a phase delay with respect to the point sources that originate from between the tips. This phase delay is given by the optical path difference and the wavelength:

$$\Delta\phi = \frac{2\pi}{\lambda}h(n_{glass} - n_{air}) \quad (3.6)$$

Where $\Delta\phi$ is the phase delay in radians, and n_{glass} and n_{air} are the indices of refraction of the glass and the air, respectively. When h is chosen such that the phase delay is a multitude of 2π rad, the interference pattern is as expected from a grating with half the slit spacing d (see Figure 3.14). However, when h is chosen that $\Delta\phi$ is not a multitude of 2π rad, the interference pattern is as expected from a grating with the channel spacing d (see Figure 3.15, which shows the result for a phase delay of $\pi/2$ rad).

From this model it can also be understood how such gratings can be optimized for certain diffraction orders. For instance, when the phase delay is chosen to be π rad, the 0-th order completely disappears due to destructive interference (see Figure 3.16). This effect can be used to create an effective beam splitter [21].

The effect of the Bragg angle on the transmission grating efficiency can be understood from Figure 3.13. Again, the Bragg angle is the angle for which the incidence angle is equal to the diffraction angle (in this case for the -1 -th order). Therefore the intended diffraction angle coincides with the angle of reflection on the surface of the transmission grating tips, thus improving the efficiency of that order.

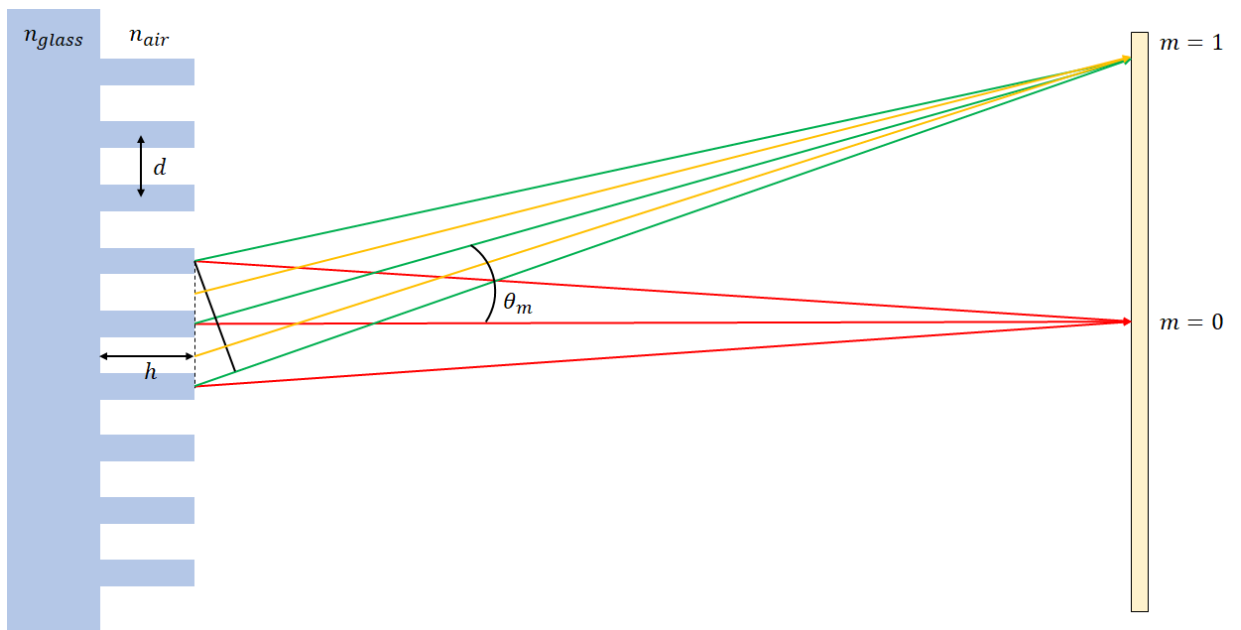


Figure 3.12: First interference order for a transmission grating with normal incident light.

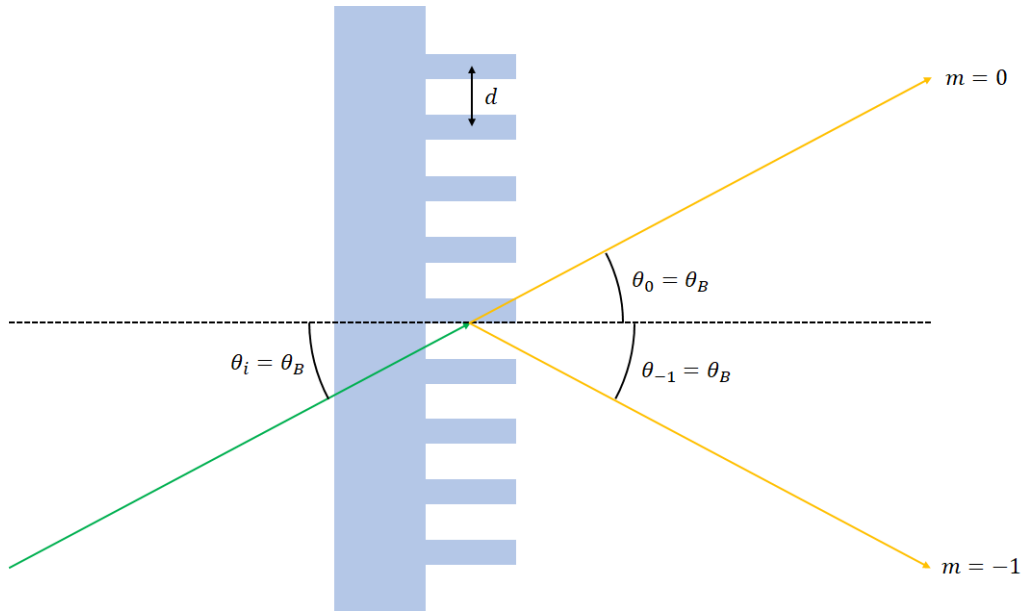


Figure 3.13: Schematic showing the efficiency effect of the Bragg angle on a transmission grating.

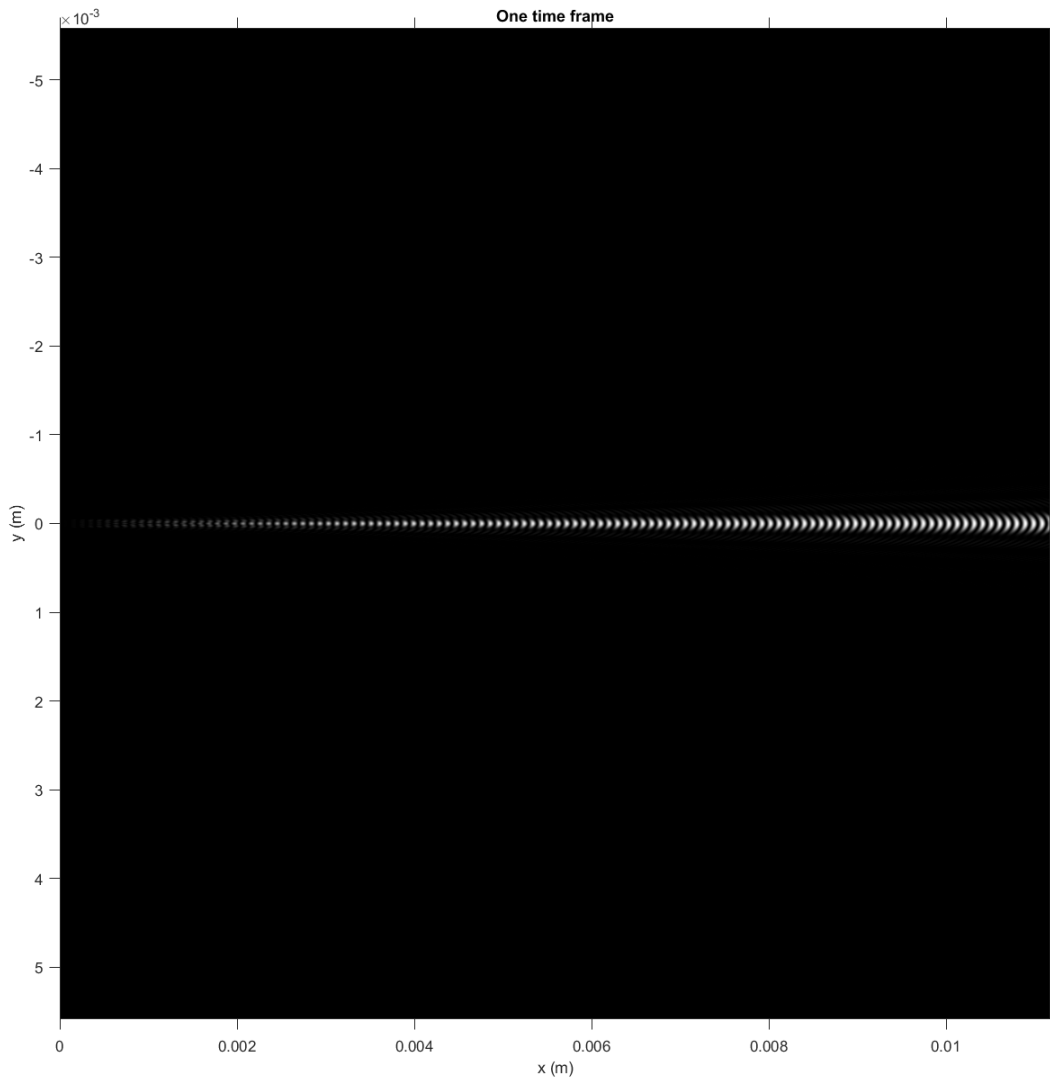


Figure 3.14: Interference pattern for a phase delay of 2π rad.

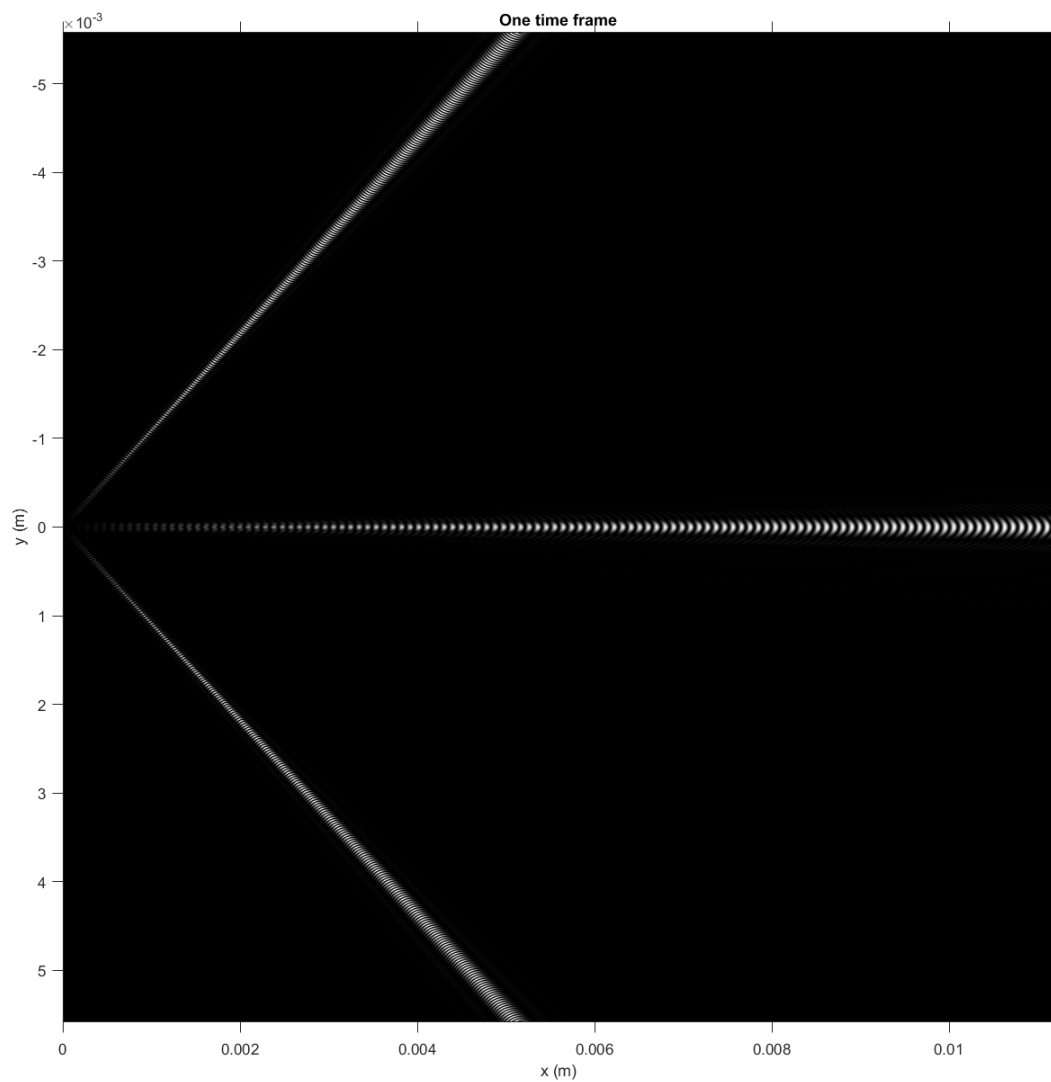


Figure 3.15: Interference pattern for a phase delay of $\pi/2$ rad.

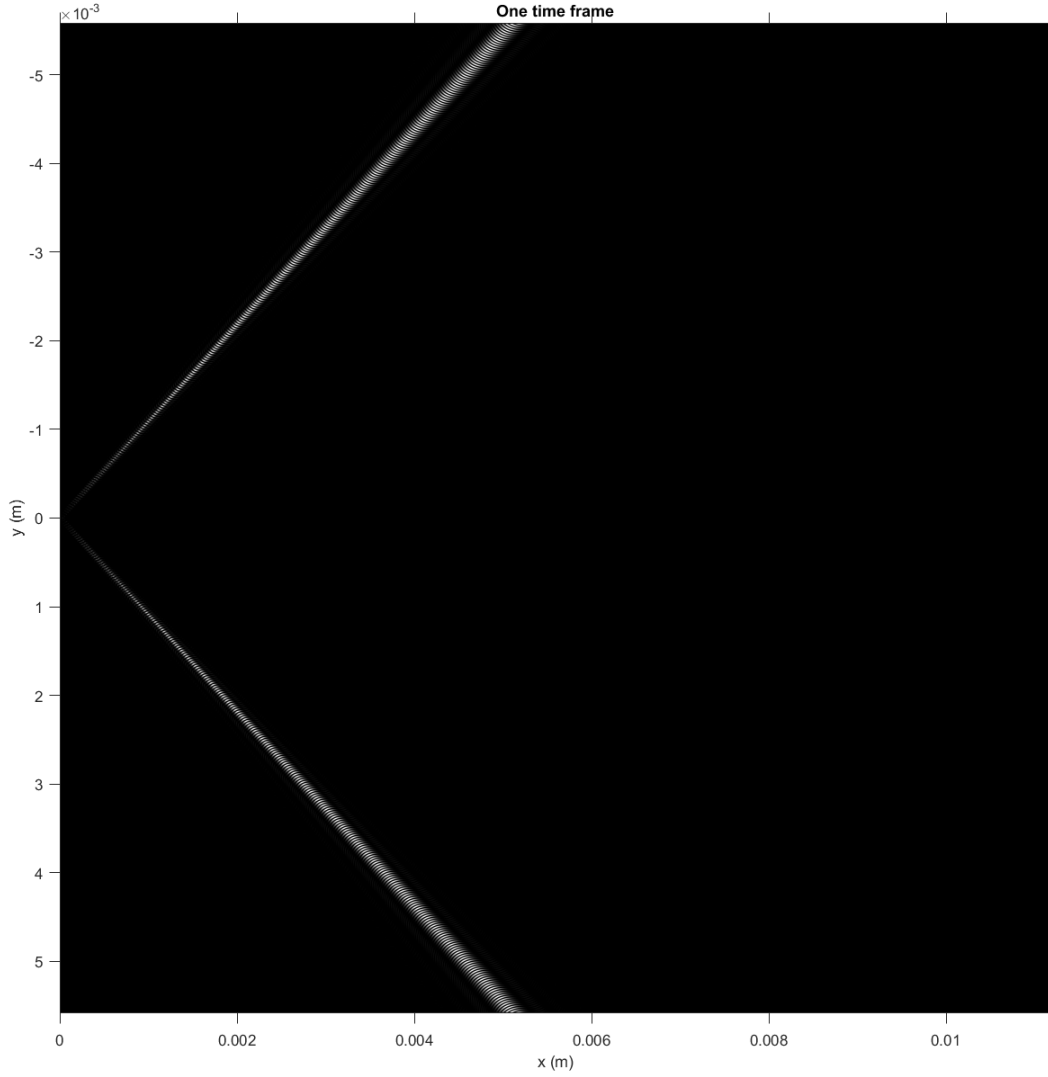


Figure 3.16: Interference pattern for a phase delay of π rad.

Non-zero incidence angle

When introducing a non-zero incidence angle to the model, the situation for the bulk multiplexer application can be represented. This expanded model can be understood from Figure 3.17. The incident beam first diffracts on the glass due to Snell's law, resulting in a propagation angle θ_g in the glass. This angle induces a phase delay $\Delta\phi_{angle}$ on the exiting surface of the grating, which can be calculated using the following equation:

$$\Delta\phi_{angle}(y) = \frac{2\pi}{n_{glass}\lambda} y \sin(\theta_g) \quad (3.7)$$

Where y is the coordinate along the grating. Thus the point sources at the exit of the grating are modeled with a phase delay gradient. The phase delay due to the grating tips can be calculated as well, assuming the optical path passes through a grating tip either completely or not at all. Then the phase difference $\Delta\phi_{grating}$ between a tip or a valley is given by the following equation:

$$\Delta\phi_{grating} = \frac{2\pi h}{\lambda} \left(\frac{n_{air}}{\cos(\theta_i)} - \frac{n_{glass}}{\cos(\theta_g)} \right) \quad (3.8)$$

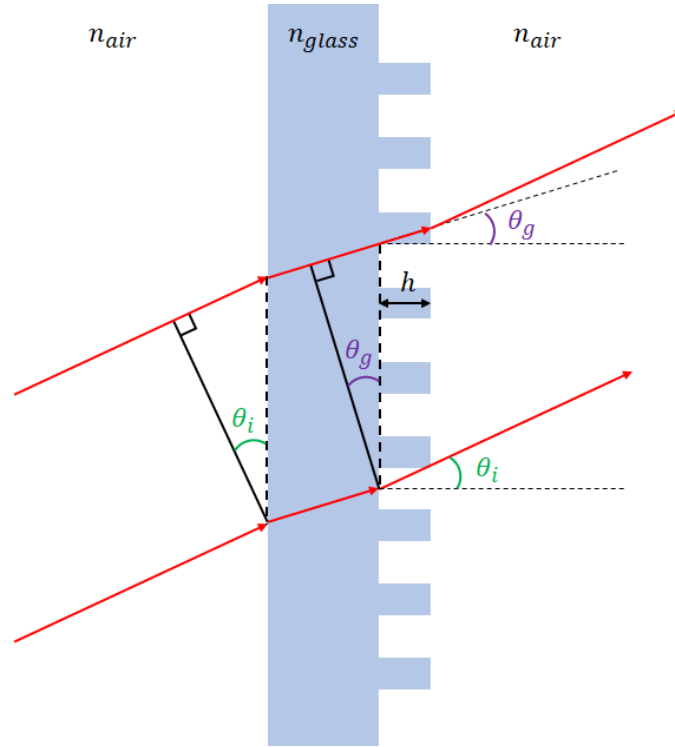


Figure 3.17: Schematic showing a transmission grating for a non-zero incidence angle.

As discussed in the supporting document, a low dispersion coefficient is favorable for the signal integrity and link budget. For the bulk multiplexer, a grating with a resolution of 600 l/mm is chosen, which results in a grating spacing of 1.67 μm and a Bragg angle of 27.7°. The chosen angle of incidence is 25°. These parameters give the interference pattern shown in Figure 3.18, which shows both the 0-th and the -1-th order under the expected angles.

This pattern assumes a phase delay due to the grating tips of $\pi/2$ rad. When a phase delay of π rad is chosen, the interference pattern is as shown in Figure 3.20. This phase delay is achieved for a grating tip height of 1.9 μm . It can be seen that the 0-th order is canceled, and only the -1-th order is transmitted.

The relative intensity in the far field for a phase delay of $\pi/2$ is shown in Figure 3.19, which shows two peaks. The first represents the 0-th order, while the second peak represents the -1-th order. Note that the resolution is limited. The same plot is shown for a π phase delay in Figure 3.21, which shows only the -1-th order peak. Therefore, in this simplified model according to Figure 3.12, an efficiency of 100% is achieved.

In reality the -1-th order efficiency achieved for such a grating is typically 93% [21]. This is in part due to the fact that the simplified model breaks down for incidence angles greater than zero. Other losses could be explained by manufacturing tolerances.

Note that this model approximately confirms the 700 $\mu\text{rad}/\text{nm}$ dispersion coefficient calculated using Equation (3.9) [21]. The diffraction angles and dispersion coefficients calculated using this equation are shown in Figure 3.22. Note that here the dispersion coefficient is a little lower than 700 $\mu\text{rad}/\text{nm}$ for an incidence angle of 25°.

$$\frac{d\theta_m}{d\lambda} = \frac{\sin(\theta_i) - \sin(\theta_m)}{\lambda \cdot \cos(\theta_m)} \quad (3.9)$$

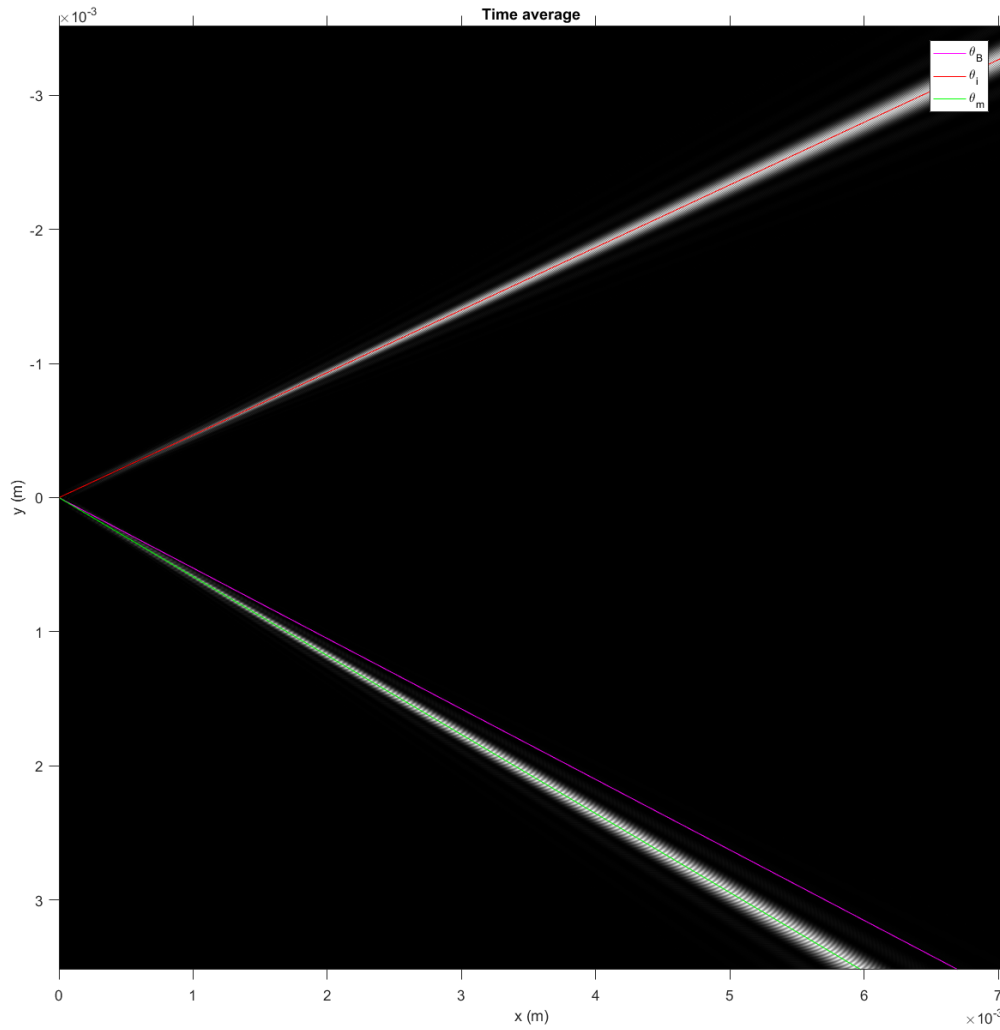


Figure 3.18: Interference pattern for the bulk multiplexer grating with a phase delay due to the tips of the grating of $\pi/2$ rad. The 0-th order is transmitted under the incidence angle θ_i , while the -1 -th order is transmitted under the diffraction angle θ_m . The Bragg angle θ_B is also indicated.

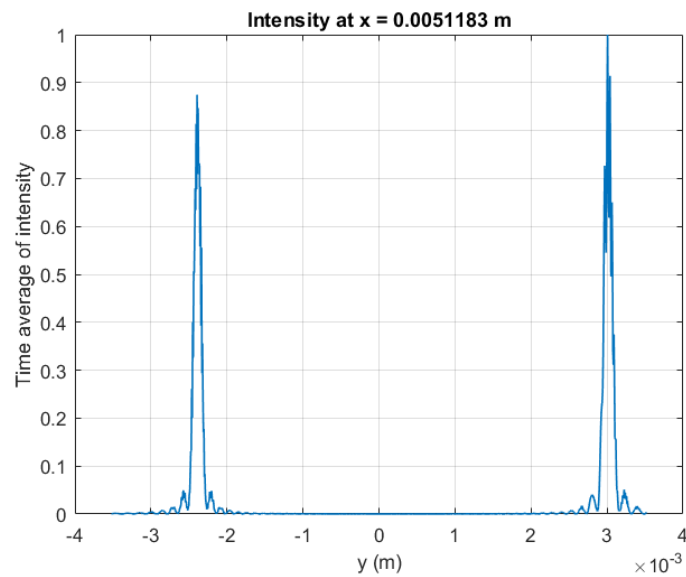


Figure 3.19: Far field intensity due calculated for a phase delay due to the grating tips of $\pi/2$.

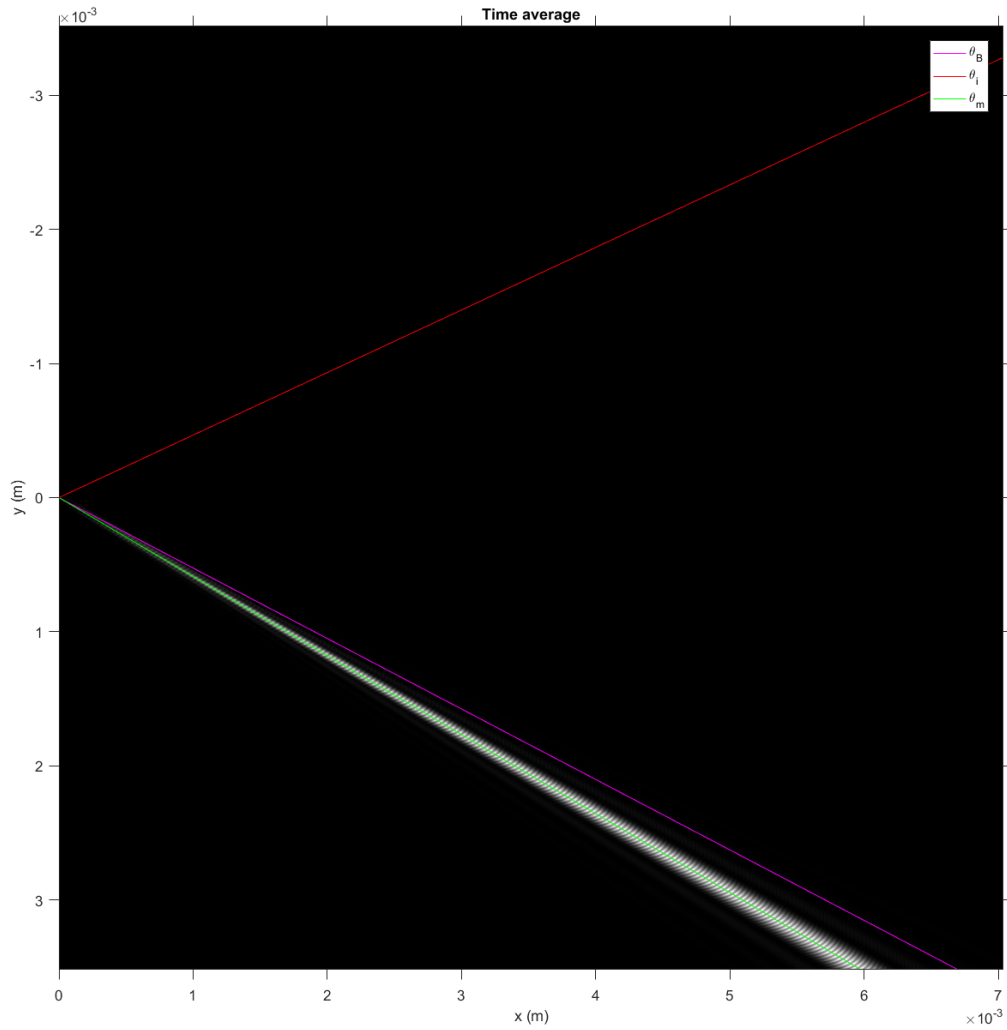


Figure 3.20: Interference pattern for the bulk multiplexer grating with a phase delay due to the tips of the grating of π rad. The 0-th order is transmitted under the incidence angle θ_i (but canceled out in this case), while the -1 -th order is transmitted under the diffraction angle θ_m . The Bragg angle θ_B is also indicated.

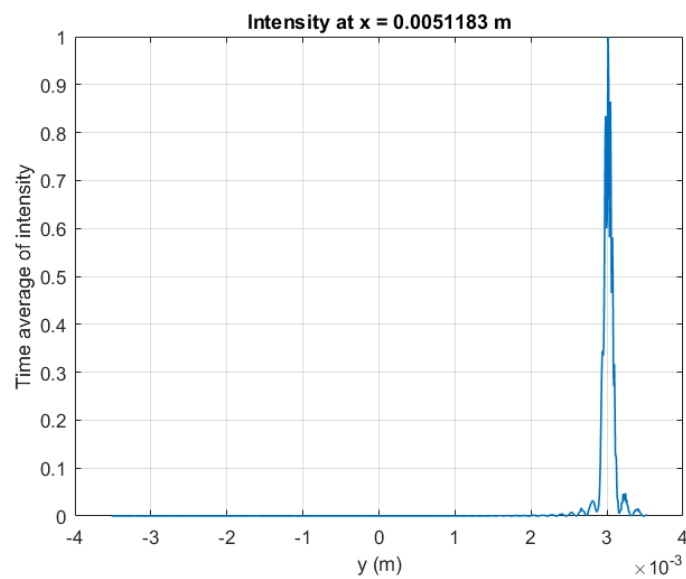


Figure 3.21: Far field intensity due calculated for a phase delay due to the grating tips of π .

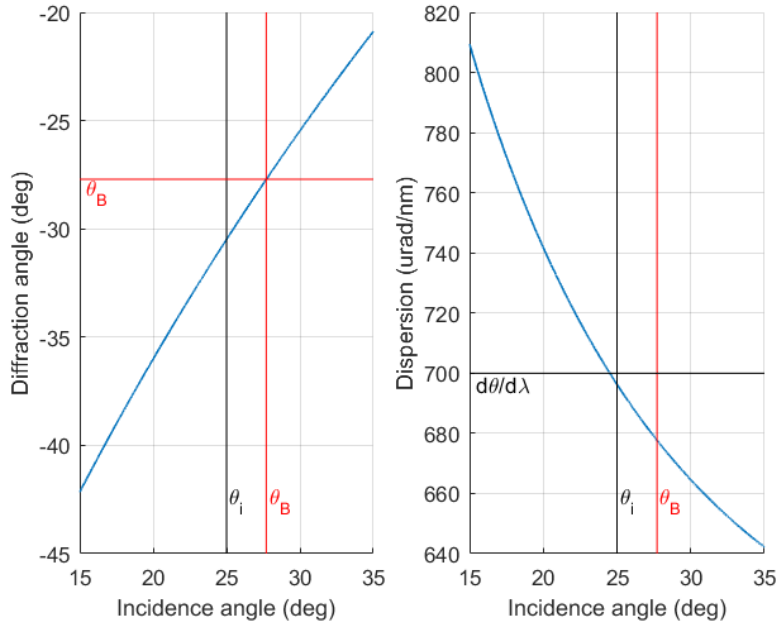


Figure 3.22: Algebraic diffraction angles and dispersion coefficients for the bulk multiplexer transmission grating, calculated using Equation (3.5). The Bragg angle θ_B is indicated, as well as the chosen incidence angle θ_i and the chosen dispersion coefficient $d\theta/d\lambda$.

3.2.3 Combination using the wavelength dependency of reflectance

As mentioned, reflectance can also be wavelength dependent. Special filters, called dichroic filters, are designed to transmit one particular range of wavelengths while reflecting another range. As shown in Figure 3.23, these filters can be used to combine lasers of different wavelengths. However, as discussed in the supporting document, the proposed bulk multiplexer has a channel spacing and spectral spread in the order of nanometers. This means that the transition region between transmitted and reflected wavelengths should be smaller than approximately 1 nm.

Thorlabs shortpass filters have a transition region of at least 50 nm (see Figure 3.24), which is an order of magnitude larger than required. More importantly, a total of 12 dichroic filters would need to be designed and manufactured, each with slightly different optical properties. Therefore this concept is not chosen for the bulk multiplexer.

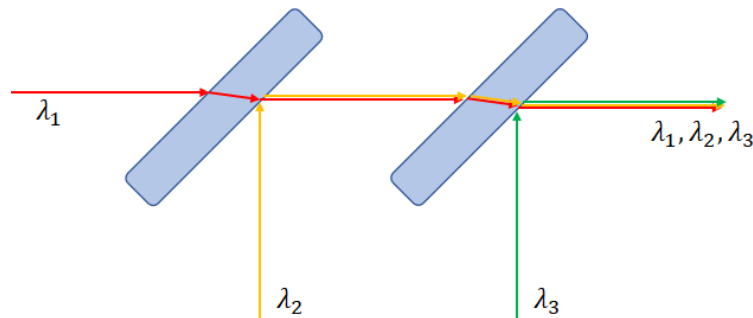


Figure 3.23: Wavelength beam combining using dichroic filters.

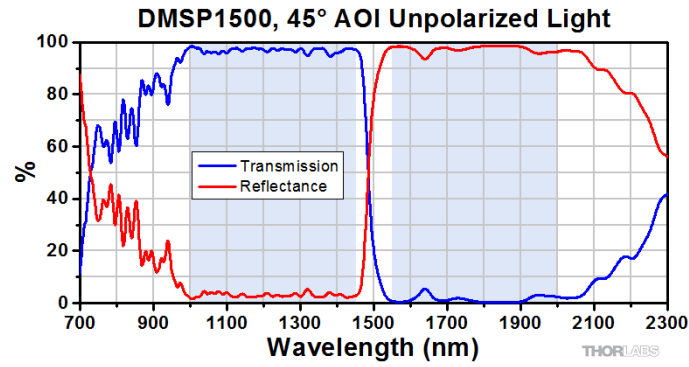


Figure 3.24: Shortpass dichroic filter transmission/reflectance per wavelength.

3.3 Proposed design challenge

As mentioned, the chosen optical concept for the bulk multiplexer is the transmission grating. The complete design of the bulk multiplexer and the TOMCAT project is analysed in the supporting document. However, the part of the optical design that is most relevant for the design challenge is shown in Figure 3.25.

This thesis focuses on designing the collimator alignment assembly for the 7 lasers indicated in Figure 3.25. As motivated in the supporting document, these lasers need to be placed next to each other with 14 mm spatial separation, based on the used dispersion coefficient and the available propagation distance of 6.3 m.

The collimator width is set to be 11 mm. This can not be reduced any further, because this would decrease the clear aperture size. A smaller aperture size would lead to more clipped power, and more divergence (see the supporting document). As a result the spatial separation of the collimators is 3 mm, as shown in Figure 3.26.

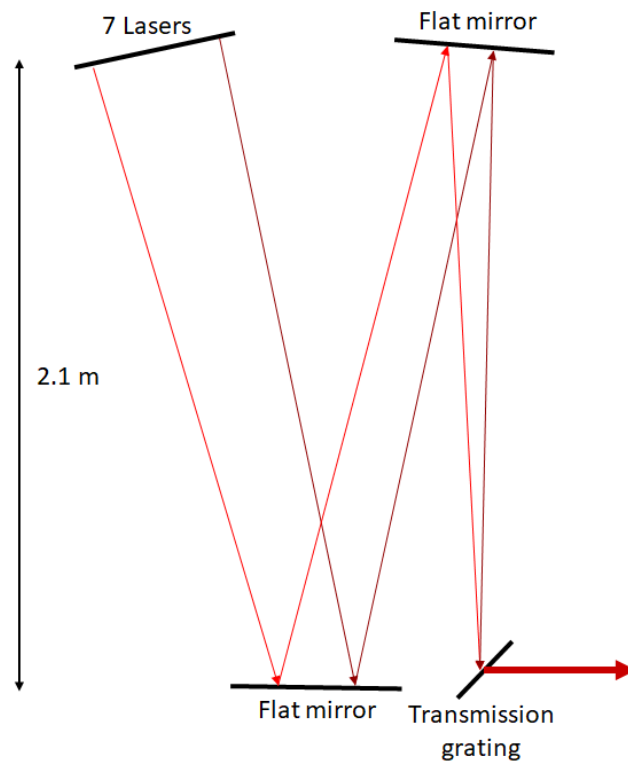


Figure 3.25: Bulk multiplexer optical design. Seven lasers are combined using a transmission gratings after a propagation length of 6.3 m.

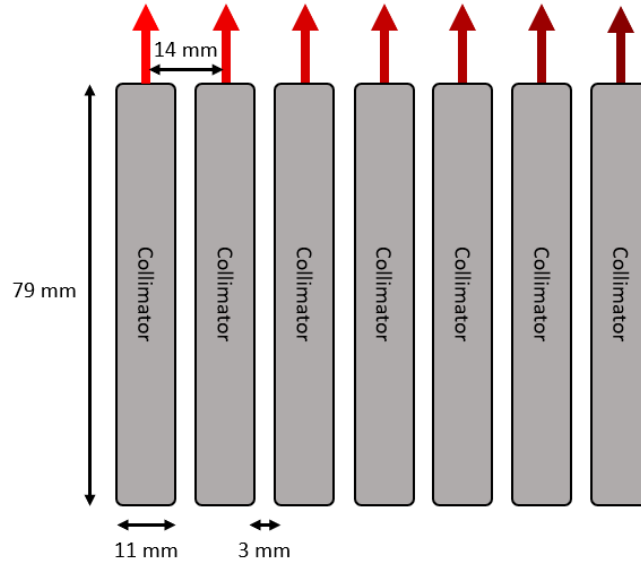


Figure 3.26: Dimensions of collimators and their separation.

3.4 Thermo-mechanical challenge

The use of high-power lasers brings forth a thermo-mechanical challenge in the grating. The calculated dispersion coefficient and diffraction angles assume a constant grating spacing. In reality, however, this is not achieved because the grating absorbs part of the laser light that is directed through it. As a result, the grating heats up and expands, causing the grating spacing to increase locally.

The heating of the grating is shown in Figure 3.27. A Gaussian beam with a $1/e^2$ radius r and incidence angle θ_i hits the anti-reflective coating of the grating, after which it propagates through the fused silica (which is the main material of the grating).

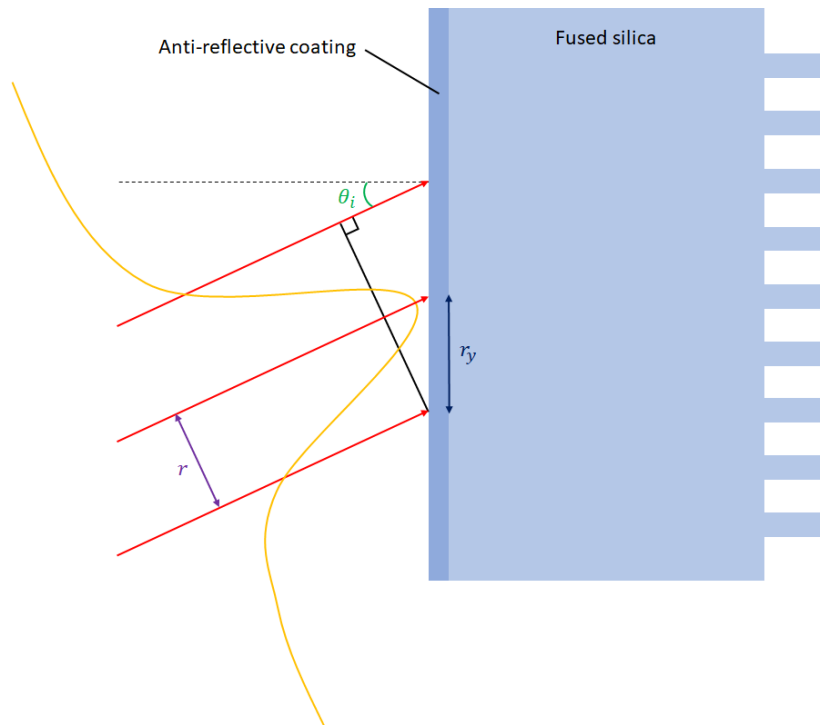


Figure 3.27: Schematic drawing of incoming laser beam heating the grating. The beam has a $1/e^2$ radius of r and an incidence angle of θ_i , causing a cross section radius in the orthogonal direction r_y .

Note that the absorption per meter of the coating can be up to 70 times the absorption of the fused silica. However, this coating is also much thinner (300 nm) than the fused silica thickness (625 μm). Therefore the power dissipated in the fused silica is still 30 times the power dissipated in the coating.

The cross-section of the beam at the coating interface is not a perfect circle due to the angle of incidence. Instead it is an ellipse with the radius along the grating lines being the $1/e^2$ radius r , and the radius in the orthogonal direction r_y being given by the following equation:

$$r_y = \frac{r}{\cos(\theta_i)} \quad (3.10)$$

As mentioned, the heating causes the grating to expand and the grating spacing to increase locally. A schematic depiction of an undeformed grating is shown in Figure 3.28, along with its deformation graph.

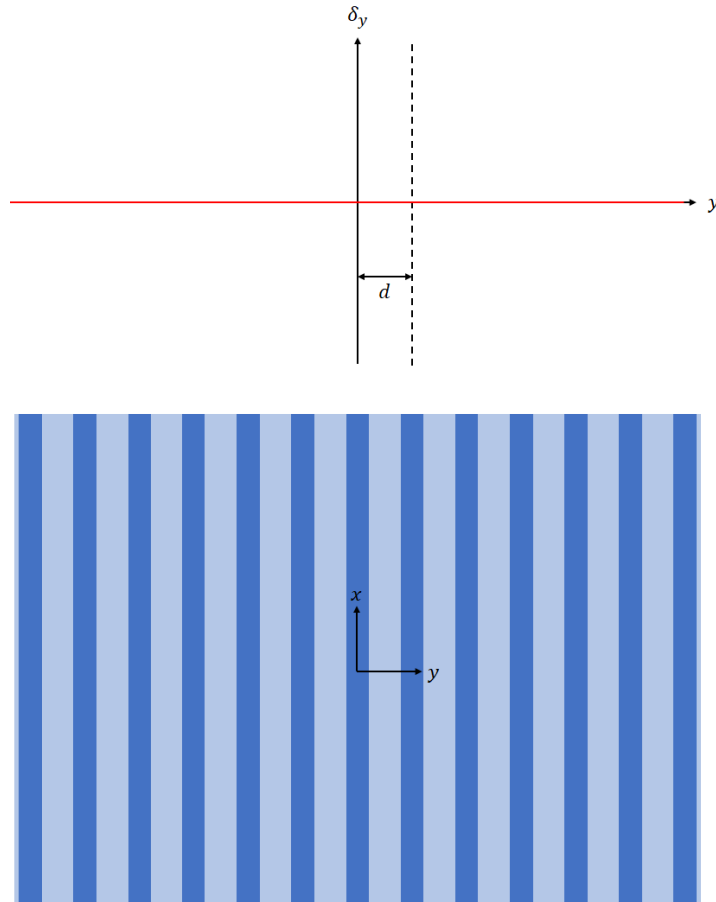


Figure 3.28: Schematic drawing of an undeformed grating with its deformation graph above. The grating spacing d is also indicated.

For this undeformed grating, the grating spacing is constant and equal to d :

$$d(y) = y_2 - y_1 = d \quad (3.11)$$

Where y_1 is the y -coordinate of one grating line, and y_2 is the y -coordinate of the grating line next to it. Figure 3.29 shows a schematic depiction of a deformed grating with a sketch of its deformation graph. The deformation is chosen greater in the center of the grating to match the expected temperature gradient (since the heat source is in the center). The same graph is also shown with the horizontal axis being the sum of the y -coordinate and the deformation. The new grating spacing d' is no longer constant but given by the deformation:

$$d'(y) = y'_2 - y'_1 = (y_2 + \delta_{y_2}) - (y_1 + \delta_{y_1}) = d + \delta_{y_2} - \delta_{y_1} = d + (y_2 - y_1) \cdot \frac{\partial \delta_y}{\partial y} = d \cdot \left(1 + \frac{\partial \delta_y}{\partial y}\right) \quad (3.12)$$

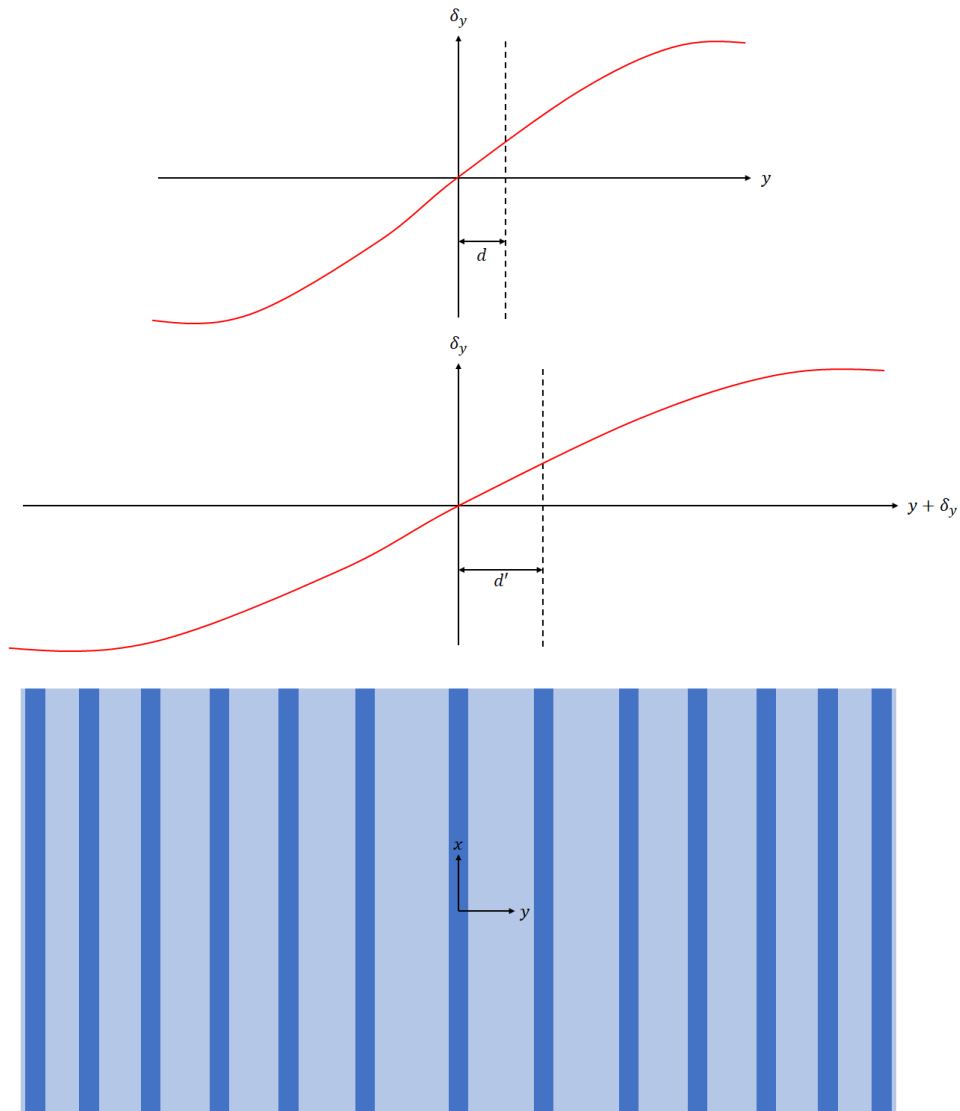


Figure 3.29: Schematic drawing of a deformed grating with its deformation graph above, including the same graph where the horizontal axis is the sum of the y -coordinate and the deformation. The grating spacing d and the new grating spacing d' are also indicated.

Chapter 4

Alignment Mechanisms

4.1 Introduction

As presented in the supporting document, one of the most important limiting factors of the TOMCAT system is the pointing accuracy. The dynamic part can be mostly attributed to the atmospheric beam wander. The static part of the pointing accuracy can be mostly attributed to the opto-mechanical limitations of the ground station, and thus in part to the alignment of the collimators on the bulk multiplexer.

This chapter explains the typical design features for an alignment mechanism, presents some state-of-the-art for such mechanisms, and concludes with an overview of all the design parameters set for this thesis.

4.2 Alignment features

The presented typical design features for alignment are: resolution, range, actuation, guiding, locking stability, thermal stability, creep stability and stiffness.

4.2.1 Resolution

Resolution simply means the step size with which an optical component can be aligned. Therefore this design parameter directly flows from the required alignment accuracy. Sometimes this required accuracy can also be achieved on mechanical tolerances alone. The boundaries for which technique should be used depends on the situation (e.g. instrument size), but roughly the following rules-of-thumb apply [22]:

Larger than 1 mm/mrad	: Assembling tolerances
Between 10 $\mu\text{m}/\mu\text{rad}$ and 1 mm/mrad	: Shims/manufacturing tolerances
Between 300 nm/nrad and 10 $\mu\text{m}/\mu\text{rad}$: Manual alignment mechanism
Between 2 nm/nrad and 300 nm/nrad	: Active alignment mechanism

As presented in the supporting document, the static part of the pointing accuracy translates to approximately 40 μrad at the bulk multiplexer level, due to the magnification factor. However, the other sub-systems of the ground station also take up part of this budget. Furthermore, any misalignment of the collimators with respect to each other can no longer be compensated for in the rest of the system.

Therefore a pointing accuracy budget of 10 μrad is allocated to each individual collimator. This places it exactly at the boundary of the rules-of-thumb between shims/manufacturing tolerances and manual alignment mechanisms. However, note that the instrument size is very small in this case due to the required spatial separation of 14 mm. Therefore the anticipated solution for the required alignment accuracy is the design of a manual alignment mechanism. The footprint constraints also limit the use of standard COTS components.

Also note that the alignment in the other DOFs is much less critical (due to the propagation distance of 6.3 m, and an allowed uncertainty in polarization axis of ± 3 degrees). Therefore these DOFs can be aligned on manufacturing tolerances.

4.2.2 Range

Range simply means the largest deviation possible from the nominal alignment. This design parameter is determined by the expected uncertainty in the alignment due to opto-mechanical tolerances. For this thesis, the focus lies on the alignment of the collimators with respect to each other. Therefore the tolerance loop goes from the optical axis to the mounting block (see Figure 4.1).

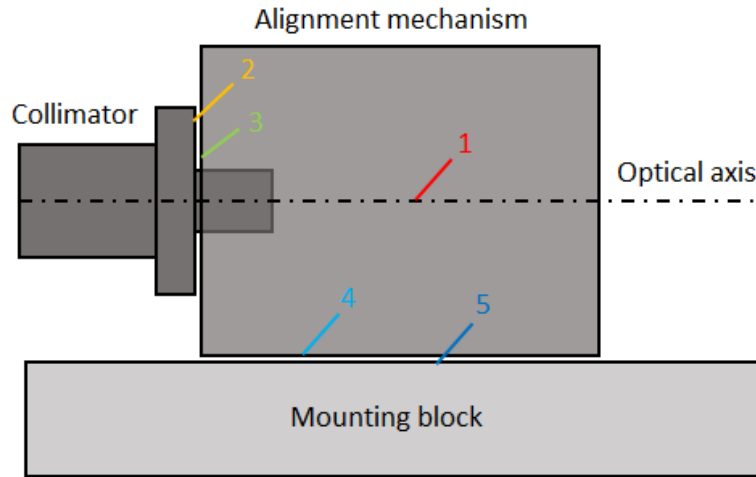


Figure 4.1: Overview of the tolerance loop from the optical axis to the mounting interface.

The tolerance loop with individual tolerances is shown in Table 4.1. The main contributor is the orthogonality of the optical axis to the collimator mounting interface, because the lens of the collimator is small and therefore difficult to align and glue. The other contributors are the three mechanical interfaces in the system. The manufacturing tolerance for this was estimated to be ± 2 arcminutes (or 0.033°) per interface. Adding these tolerances quadratically (assuming them to be independent) results in a total tolerance of $\pm 0.12^\circ$.

Therefore the required range for the designed alignment mechanism is this $\pm 0.12^\circ$ (or 2.1 mrad). Combined with the required resolution this gives a required dynamic range of 420, meaning the mechanism needs to make 420 steps of 10 μ rad (assuming the mechanism is linear across its range).

Interface	Tolerance
1-2	$\pm 0.1^\circ$
2-3	$\pm 0.033^\circ$
3-4	$\pm 0.033^\circ$
4-5	$\pm 0.033^\circ$

Table 4.1: Mechanical tolerances per interface.

4.2.3 Actuation

The aforementioned 420 steps need to be made with some form of actuation. This actuation needs to be compatible with both the required resolution and range.

Shims

The use of shims can be an attractive form of actuation because of its inherent stability. The basic working principle can be seen in Figure 4.2 (where the thickness of the shims is highly exaggerated), but there are other options available.

The smallest available shim thickness is 5 μ m, which would be the limiting factor for the resolution of shims. Rather than using 420 shims of 5 μ m thick, one would use different thicknesses to cover the full

dynamic range of 2100 μm . The used thicknesses for a binary system would be: 5, 10, 20, 40, 80, 160, 320, 640 and 1280 μm . Any thickness between 0 and 2100 μm can then be created by either using or omitting the available shims. When using the 1-2-5 system also used in many valuta systems the number of different thicknesses is reduced to 8: 5, 10, 25, 50, 100, 250, 500 and 1000 μm . These thickness are also more often available off the shelf. A drawback could be that one might need two of the same, depending on the required total thickness.

The required arm length to translate the 5 μm sensitivity (where sensitivity is defined as the step size of the actuation method) into 10 μrad resolution would be 500 mm. This can be reduced to 100 mm if a sensitivity of 1 μm is achieved. This can be done by ordering shims of for instance 100 μm thick and a tolerance of $\pm 10 \mu\text{m}$. These shims can then be measured for their exact thickness and be divided into groups of 100 μm , 101 μm , 102 μm , etc.

The result is that alignment using shims would be a relatively labor intensive actuation method, compared to the other options available. This also means that continuous alignment is more difficult. However, the main advantage is that the use of shims inherently also locks the system. Furthermore, the thermal resistance of the stack of shims is potentially much lower compared to the alternatives, allowing for smaller temperature gradients.

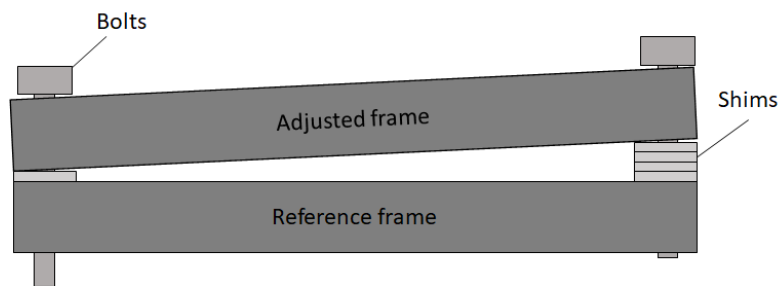


Figure 4.2: Schematic depiction of using shims for tip/tilt correction.

Alignment screw

Rather than using shims for actuation, an alternative is using alignment screws. The achieved sensitivity depends on the pitch of the screw and the rotations made by the human operator. Typically, 5 to 10 degrees steps can be made when alternating between measuring and actuating. However, when there is a live measurement signal then 0.5 degrees are typically achievable [22].

If the available arm length is long enough, then even regular screws can be used. However, there are also screws available with a finer pitch than the standard screws used for mounting mechanics. Therefore a sensitivity in the order of 0.5 to 5 μm is possible.

For even smaller sensitivities, a special type of screw can be used, called the differential screw. This screw uses two opposite moving threaded ends with a small difference in pitch. The sensitivity is then determined by this difference in pitch, and is typically in the range of 0.1 μm .

Note that the use of alignment screws requires a pre-load spring to push the actuated lever against this screw since the screw can not pull the lever towards itself.

Active components

As mentioned, there are also options available for active alignment. A motorized alignment screw has a relatively high holding force and a sensitivity between 0.1 and 1 μm .

For really demanding systems it might be worth it to use Piezo steppers. Typical sensitivities for such steppers are in the order of 20 nm, but these steppers have a low holding force, are slow in positioning and have a limited lifetime [22].

Joy stick

An alternative to the above-mentioned actuation methods is the use of a joy stick. This can be used to move a component around, where the sensitivity can be improved using a lever ratio. After the operator has found the right position, it can then be locked. This method is however typically used for translation and rotation around the optical axis and not for tip/tilt.

4.2.4 Guiding

The actuation force should be guided such that only the intended DOF is actuated. The cross-talk that occurs when an unintended DOF is actuated can significantly complicate the alignment process. Despite the fact that in this design challenge the other 4 DOFs are much less critical than the tip/tilt DOFs, it is still desirable that there is for instance no significant focus error as a result of the alignment.

The cross-talk into the other aligned DOF can be compensated for with an iterative alignment. However, an alignment mechanism with strong cross-talk is less intuitive than a mechanism with orthogonal, independent actuation. Therefore the required alignment time can potentially be reduced by designing for minimal cross-talk, making this option desirable.

Rails systems

One obvious solution for guiding a specific motion is the use of a rails system. Such systems allow for motion in one translation DOF, while restraining the other 5 DOFs.

However, rails systems have a major drawback noticed increasingly in sensitive systems. Limitations in manufacturing tolerances means there needs to be some play between the moving parts. The result is that a certain part can be anywhere within these tolerances at any given moment, giving positional uncertainties (and thus hysteresis) at least in the order of micrometers. Furthermore, rails systems are typically used for translation and not for rotation.

Kinematic mounts

A popular design in COTS systems is called a kinematic mount. In such systems, all 6 DOFs are restrained only once by using 3 sliding ball contacts. This allows for a relatively repeatable design, since there should be only one orientation possible. Two main variations exist: the first uses three different sliding ball contacts restraining 1, 2 and 3 DOFs, respectively. The second variation uses three identical sliding ball contacts restraining 2 DOFs each.

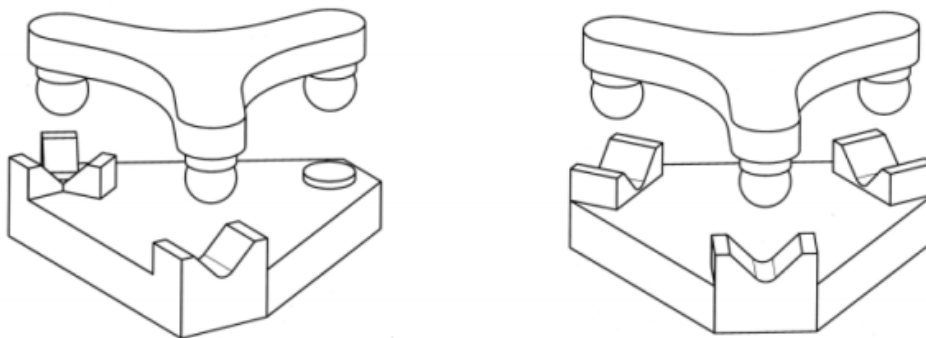


Figure 4.3: Two popular examples of kinematic mounts [23].

The DOFs can be actuated by pushing the balls against their contact surfaces, for instance using an adjustment screw with a ball tip. The two structures can be held together using pre-tension springs.

Such kinematic mounts still have some drawbacks however. First of all, the exact position in the mount depends on the sequence with which it is placed in the mount. This is because the friction between the ball and the contact surface causes a small mechanical deformation, known as virtual play. This also means that

a shock or thermal cycle can change the exact position in the mount. The virtual play can be reduced by reducing the friction coefficient between the ball and contact surface.

Another issue arises due to the fact that the balls make a point contact with their contact surfaces. This means that locally the Hertzian stresses cause the balls and contact surfaces to deform plastically. This can be partially avoided by choosing hard materials, or by designing for the use of line contacts rather than point contacts.

Flexures

A popular alternative to ball contacts is the use of flexures, which allows for a monolithic design. Since there are no longer moving parts involved, and the mechanism can be made out of one block of material, issues as play and hysteresis no longer play a role. Furthermore, the lack of thermal contact resistance makes the mechanism better at conducting heat (and also in a more predictable manner).

However, the main drawback of flexures is that they introduce stiffness. This means that the actuation force tends to increase, and also the required pre-tension force. The subsequent extra internal stresses could decrease the stability of the system, for instance due to creep.

4.2.5 Locking stability

An aligned system can be locked to avoid further drift and to make the system more robust to shocks or thermal cycles. For instance, when using an alignment screw the play within the screw gives some positional uncertainty. If the screw becomes oriented slightly differently, this can lead to drift in the system. However, locking a system actually also introduces drift, resulting in a trade-off and many different solutions for optimizing to either cost, ease-of-use or drift.

As mentioned, a system using shims inherently also locks the alignment. Furthermore, active alignment systems should not be locked. Therefore the solutions explored here focus on systems with alignment screws and joy-sticks.

Adhesives

One obvious solution is to simply glue the mechanism into the aligned state. One such method is called Liquid Pinning [24]. Here, the optical component is placed on three loosely fitting Dowel pins. After the component is aligned, the space between the Dowel pins and their respective holes is filled with epoxy. Asymmetric shrinking effects can be reduced by filling the holes fully. This locking method is however most suitable for translation, especially in combination with a joy-stick as actuation method.

Another locking method using adhesives could be to glue the alignment screw into place. A main drawback for this locking method is however that it is unpractical to use iterative locking/alignment (should this be necessary), since the glue needs to be removed between every iteration.

Perpendicular screw

Locking an alignment screw can also be done with another, smaller screw mounted perpendicular to the alignment screw. This perpendicular screw can push against the alignment screw to lock into place, based on friction. A main drawback of this system is that the alignment screw could be damaged due to wear, which can be reduced by using a plastic screw for locking.

Another drawback is that the stability of this system is limited, because the lock could still be sensitive to shocks or thermal cycles. Furthermore, the moment introduced by the locking screw can introduce significant drift in the alignment.

Counter nut

An alignment screw can also be locked using a counter (or jam) nut. The nut can be tightened against the bushel of the alignment screw, thus locking the screw based on friction. This can also lead to significant drift during locking, but this drift can be reduced by increasing the pre-tension force on the alignment screw.

Thus the thread of the screw is pushed in the thread of the bushel and the friction between the surfaces increases.

Split nut

A locking method that reduces the effect of locking drift is the split nut. Here, the nut is modified into a U-shape and the two ends of the U are clamped towards each other with a locking screw. The result is that the moment of the locking screw is not applied on the alignment screw.



Figure 4.4: Example of a split nut [22].

Push/pull pair

Another option is to use two parallel screws, one of which pushes against the aligned surface and the other pulls it in the other direction. This can be done in an iterative process until the mechanism is aligned and the tension in both screws is so high that they are locked based on the friction in the thread. A such, a controlled adjustment below $0.3 \mu\text{m}$ is achievable [22].

Leaf spring

The last option discussed here is to place a leaf spring (with one hole and a slot in it) parallel with the alignment screw. The dimensions of the holes can be chosen such that there is sufficient play to allow for the entire range of the alignment mechanism. After alignment the leaf spring can be bolted into place, thus locking the system. Again, the moment of these bolts can cause locking drift. This drift can be reduced by placing an extra leaf spring over the first one, as shown in Figure 4.5. This second leaf spring will act as a moment release plate, thus absorbing the drift-inducing moment.

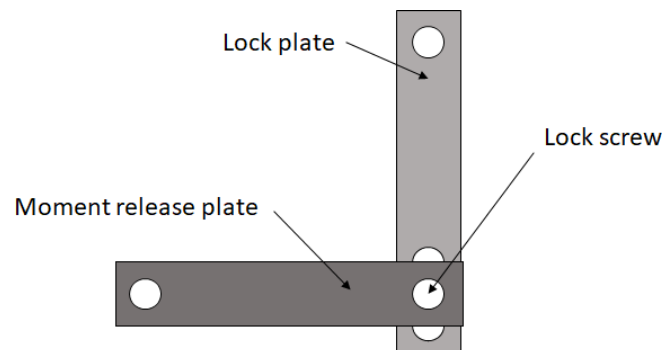


Figure 4.5: Two leaf springs used as locking plates.

4.2.6 Thermal stability

The thermal stability of an alignment mechanism is defined as the potential drift in any of the DOFs due to differences in temperature. The temperature of the mechanism can increase due to an increasing ambient temperature or due to local heat sources.

Ambient temperature

The operating ambient temperature for this design challenge is set at 20 ± 1 °C. However, the survival ambient temperature is set at 20 ± 30 °C (during transport). This means that if the system needs to be aligned before transport, this alignment needs to survive extreme thermal cycles. This means that components that are fixed based on friction can expand with respect to each other and snap into a different position.

If the system is aligned after transport, the temperature variations can still introduce drift. This can be either due to a difference in thermal time constants, or in coefficients of thermal expansion.

If the time that it takes for the mechanism to reach a new equilibrium (thermal time constant) is on a larger or similar time scale as the temperature variations, then some parts of the mechanism might warm up to the new ambient temperature quicker than other parts. This difference in temperature leads to a difference in thermal expansion, potentially leading to internal stresses/deformations.

Such differences in thermal expansion can however also occur in the new equilibrium, when the mechanism consists of different materials with different coefficients of thermal expansion. For instance, when the alignment screw is made of some type of steel and the rest of the mechanism of some type of aluminium, the screw will expand approximately half as much as the rest of the mechanism. The result is that the screw becomes relatively shorter, and thus the alignment drifts.

Local heat sources

Even if the entire mechanism can be made from one material, there still is the issue of local heat sources. In this design challenge there is a clipped power of up to 0.6 W introduced in the aligned component. This heat will flow through the mechanism, and eventually reach an equilibrium where there are thermal gradients inside the mechanism. This again leads to differences in thermal expansion, potentially leading to internal stresses/deformations.

4.2.7 Creep stability

Many materials deform elastically when exposed to internal stress, and this deformation can often be predicted (especially if it scales linearly with the induced stress). However, when this stress exceeds a certain level (depending on the specific material properties) it can continue to deform (plastically) over time. This is especially true if the material is heated. If the exact length of this piece of material is critical to the alignment, this relatively small deformation can still lead to significant drift in the mechanism.

For example, when using the locking plates described above, the continued deformation of these plates directly influences the alignment. One way to prevent such drift is to keep the internal stress well below the micro yield stress of the material.

4.2.8 Stiffness

The last feature highlighted here is the stiffness of the alignment mechanism. Often the alignment is done by hand, and the forces that come with touching the mechanism should not lead to drift or failure. Furthermore, the mechanism should be robust to potential shocks and vibrations. The Eigen-frequencies of the system scale with the stiffness of the mechanism, and any undesired dynamics can be reduced/prevented by increasing these frequencies.

4.3 State-of-the-art

Many different designs of alignment mechanisms are presented in the appendix of the supporting document, but the most relevant designs are presented in this section.

4.3.1 GAIA collimator mount

In a previous TNO project, a design was made for the GAIA OPD (Optical Path Difference) Testbench. In this design, many different alignment mechanisms are used for all the different optical components. On such component is the collimator, which converts a fiber laser into a free space laser beam using lenses.

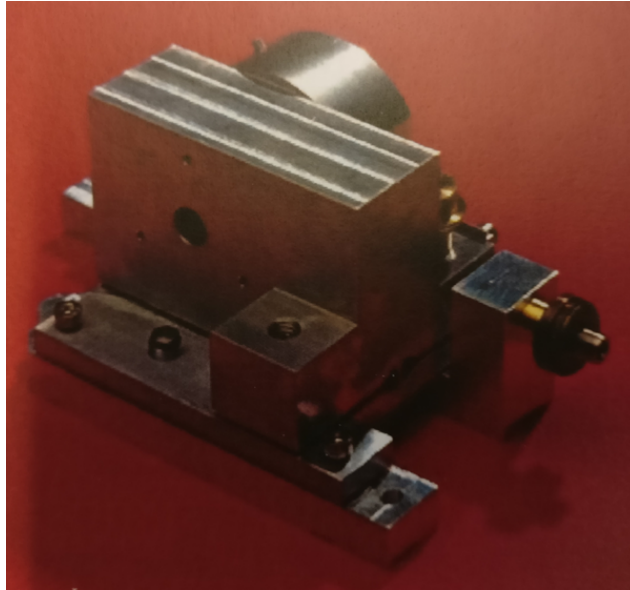


Figure 4.6: Alignment mechanism for the collimator used in GAIA [25].

This mechanism (see Figure 4.6) uses micrometer screws and hinges to adjust the tip and tilt DOFs of the collimator, and mounts the collimator in a rotatable bush used for aligning the polarization direction of the beam. The tip alignment is done using a flexural hinge and an arm length of 21.25 mm, while the tilt alignment is done using a shaft hinge and an arm length of 41.25 mm.

The achieved tip/tilt range is over ± 5 mrad, and the resolution 24 μrad . The flexural hinge was later modified to reduce its stiffness.

4.3.2 GAIA fine mirror mount

The alignment mechanisms for two of the mirrors used in GAIA achieve a better resolution by using a mechanical reduction ratio, see Figure 4.7. The hinge that connects the mirror to the fixed world is located 13 mm lower than the hinge that connects the lever to that fixed world. At the same time, the mirror is connected to the lever with a leaf spring, which is located 26 mm above the mirror hinge. This gives a reduction ratio of 2:1. Combined with the longer arm length this gives the resolution of 4 μrad , and the range is ± 10 mrad.

Although the initial alignment can be achieved within 1 μrad uncertainty, the locking resulted in 10 μrad drift. This was compensated for by iterative aligning/locking. Also, removing the alignment screw caused several μrad drift.

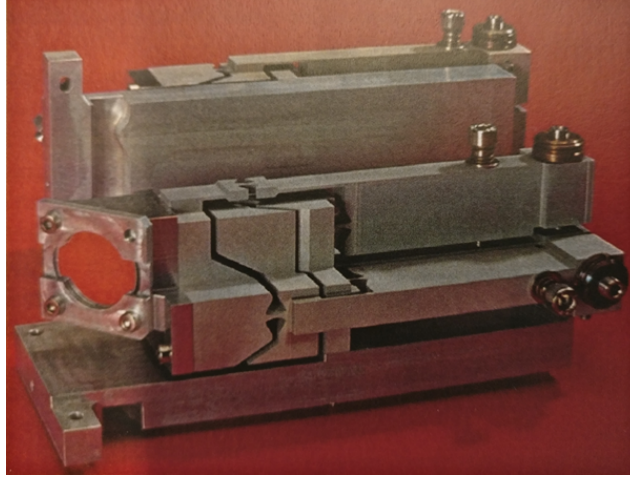


Figure 4.7: Alignment mechanisms for two mirrors used in GAIA [25].

4.3.3 Elastic lever mirror mount

A similar resolution of 1-5 μrad is achieved by the mechanism shown in Figure 4.8. Here, the alignment screws are used to elastically deform the thin plates. As a result, the mirror rotates far less than the tip of the thin plates. Thus the resolution is better than would be possible with thicker plates/levers. However, the design is under constrained and sensitive to dynamics.

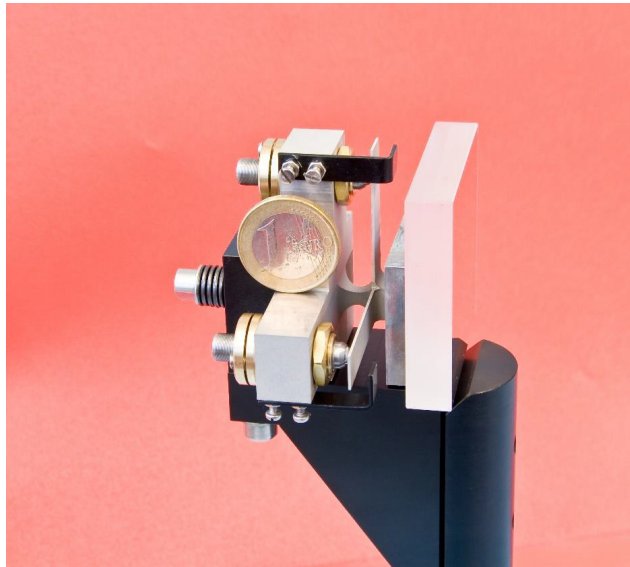


Figure 4.8: Elastic lever mirror mount [22].

4.4 Design parameters overview

In the previous chapters and sections, all the design parameters for the required alignment mechanism have been presented. In this section, a brief overview is given of all these values along with their source.

The resolution of 10 μrad is part of the total pointing error budget. The importance of a low pointing error is in part shown in the signal integrity analysis of the supporting document.

The range of $\pm 0.12^\circ$ is determined by the manufacturing tolerances presented in Section 4.2.2. The main contributor here is the misalignment of the collimator lens.

The stability requirement of $\pm 5 \mu\text{rad}$ is also part of the total pointing error budget, meaning that together with the resolution it forms the total allowed pointing error for the alignment mechanism during operation.

The heat source of < 0.6 W is due to the expected clipped power in the collimator, as discussed in the collimator analysis presented in the supporting document. Note that the 0.6 W is a worst-case estimate, based on the worst-case mode field diameter of the fiber. The nominal clipped power is 0.4 W, whereas the best-case clipped power is 0.3 W.

The operating temperature of 20 ± 5 °C is defined for the average temperature of the collimator, and is also based on the collimator analysis presented in the supporting document. Note that the temperature requirement is coincidentally most stringent for the mode field diameter associated with a clipped power of 0.3 W. This is because the temperature range is based on the beam radius tolerance, which is also determined by the mode field diameter. For the nominal design, the operating temperature can be 20 ± 15 °C.

The lateral separation of 14 mm is based on the dispersion coefficient of the used transmission grating, and the propagation distance between the grating and the collimators. The lateral positioning of 50 μ m is part of the telescope aperture budget, meaning that the beams should overlap within this budget such that they can be positioned as one beam in the telescope aperture.

The angular separation of 2.24 mrad is also based on the dispersion coefficient of the used transmission grating, and the propagation distance between the grating and the collimators. The angular positioning of 0.033° is based on the tolerance budget presented in Section 4.2.2. More specifically, it is the tolerance set on interface 4-5.

And the exit pupil diameter of 9 mm is set to avoid additional clipping, which would also mean extra divergence of the beam. In other words, it is ensured that the collimator lens is the limiting aperture in the system.

Parameter	Value	Source
Resolution	10 μ rad	Part of pointing error budget
Range	$\pm 0.12^\circ / 2.1$ mrad	Manufacturing tolerances
Stability	± 5 μ rad	Part of pointing error budget
Heat source	< 0.6 W	Clipped power in collimator
Operating temperature	20 ± 5 °C	Nominal design and beam radius tolerance
Lateral separation	14 mm	Dispersion coefficient of grating and propagation distance
Lateral positioning	50 μ m	Telescope aperture
Angular separation	2.24 mrad	Dispersion coefficient of grating and propagation distance
Angular positioning	$0.033^\circ / 0.6$ mrad	Tolerance budget for range
Exit pupil diameter	9 mm	Avoid additional clipping

Table 4.2: List of requirements

Part II
Design

Chapter 5

Conceptual Design

5.1 Introduction

The first part of this thesis presented the background of the design assignment, and motivated all the requirements. These requirements are summarized in Section 4.4. The second part of this thesis presents the actual design of the required alignment mechanism. For this design, four main concepts are presented in this chapter. The first three concepts are based on adjusting the orientation of the collimator, while the fourth concept is based on steering the laser beam.

5.2 Single lever concept

The first concept can also be considered the most basic, and is drawn schematically in Figure 5.1. The adjusted frame is connected to the reference frame by a hinge. An adjustment screw is mounted in the reference frame and pushes the adjusted frame to rotate around the hinge. The pre-tension spring pushes the adjusted frame against the adjustment screw, which allows the adjustment screw to adjust in both directions.

An adjustment screw was chosen over the other actuation methods, because it has a greater potential for achieving the required resolution. Furthermore, the limited available footprint means that shimming would be even more complicated and time consuming than in typical alignment procedures, especially when the mentioned trick should be used for obtaining sensitivities below 5 μm .

The resolution of this concept is given by the somewhat trivial equation (where the small angle approximation is applied):

$$\text{Resolution (urad)} \approx \frac{\text{Sensitivity (nm)}}{\text{Arm length (mm)}} = \frac{\text{Screw pitch (um)} \cdot \text{Rotation (deg)}}{\text{Arm length (mm)}} \cdot 1000/360^\circ \quad (5.1)$$

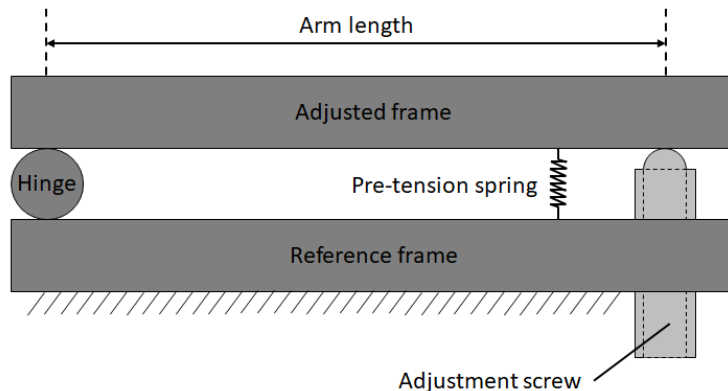


Figure 5.1: Schematic depiction of the single lever concept.

Because of the limited available footprint, the adjustment screws are selected based on their total dimensions, as well as their pitch. Most typical adjustment screws are not compatible since their bushel diameter exceeds practical dimensions. Therefore two main candidates remain.

The first is a fine pitch screw supplied by Thorlabs (see Figure 5.2), which exceeds class 3 tolerances with a pitch of $250\ \mu\text{m}$. In order to reach the desired $10\ \mu\text{rad}$ resolution for 0.5 degree rotations of the screw, a $35\ \text{mm}$ arm length is required. The bushel diameter is $4.5\ \text{mm}$, its length $5\ \text{mm}$, and the screw has a length of $8\ \text{mm}$.

The second is an ultra fine pitch screw supplied by Kozak Micro Adjusters, which exceeds the thread class 6g-6H by 45% with a pitch of $50\ \mu\text{m}$. Therefore the required arm length is $7\ \text{mm}$. The other dimensions are equal to the Thorlabs alternative. Since screws with this pitch are currently only made by this specific supplier located in the USA, for now the choice between these screws is left open.

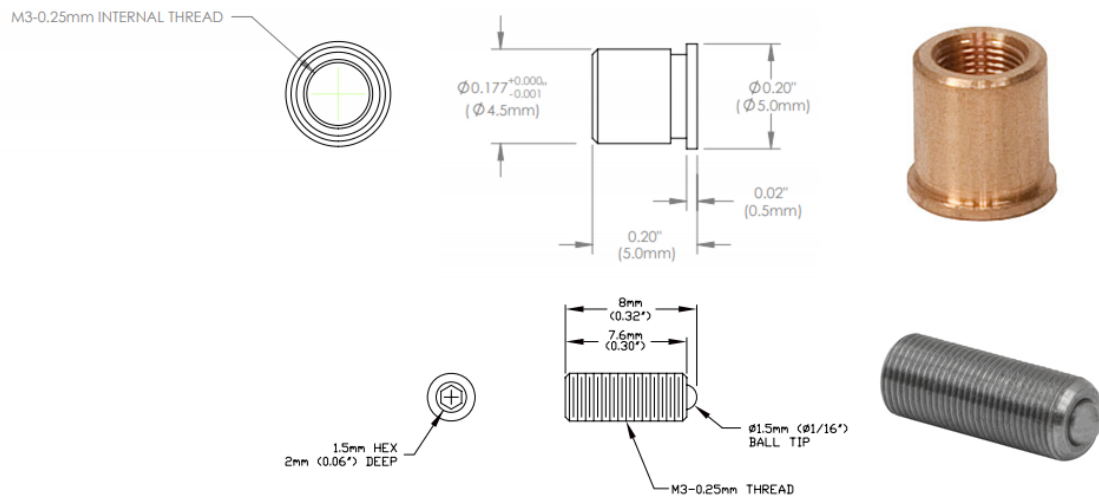


Figure 5.2: Thorlabs screw with $250\ \mu\text{m}$ pitch.

Note that the schematic drawing in Figure 5.1 is for only one DOF, either tip or tilt. However, the design challenge is to align both tip and tilt. This can be achieved by stacking two similar mechanisms on top of each other, as shown in Figure 5.3. Here, the orientation of these mechanisms is chosen such that multiple collimators can be placed next to each other (as also required for the design challenge), as can be seen in Figure 5.4.

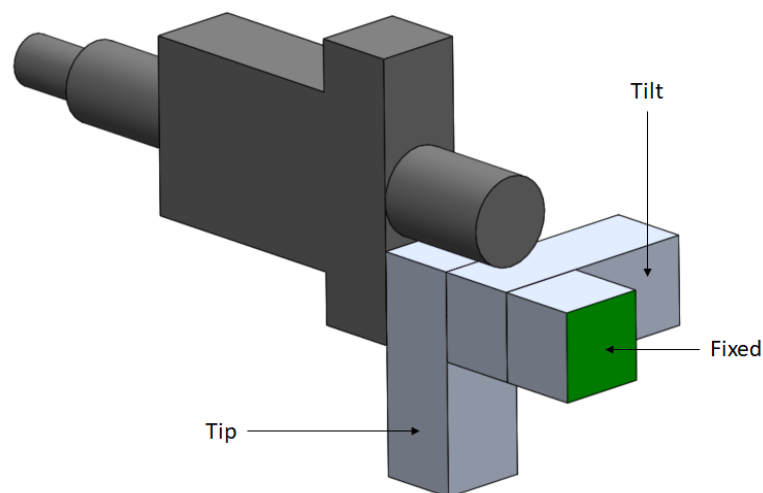


Figure 5.3: 3D depiction of the 2 DOF single lever concept.

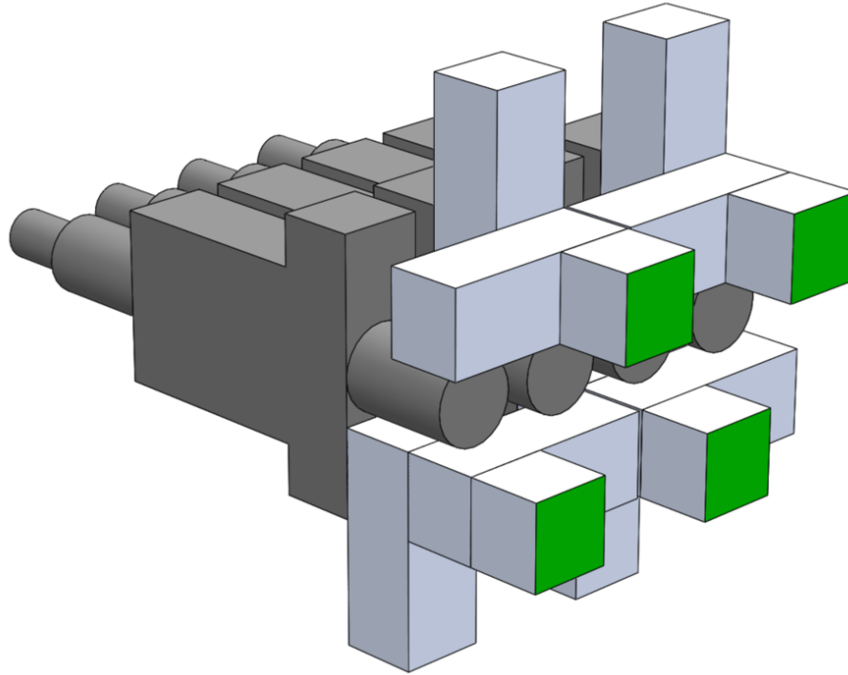


Figure 5.4: 3D depiction of the 2 DOF single lever concept, showing how multiple mechanisms can fit into each other.

In this orientation, however, the available arm length is limited to twice the spatial separation, thus 28 mm. Furthermore, the accessibility of the adjustment screws is very limited. Especially those on the bottom of the assembly are hard to reach without blocking the laser beam with the hand of the operator. This is very inconvenient, because the 0.5 degree screw rotations are only realistic if the operator has a live feedback signal. Also, if the alignment would be done at full power this poses a threat to the health and safety of the operator.

These problems can be prevented by designing an alternative mechanism, where the frames are folded (see Figure 5.5). This allows for a more compact design, because the arm length of the mechanism is achieved in a direction that is not restrained by the limited footprint.

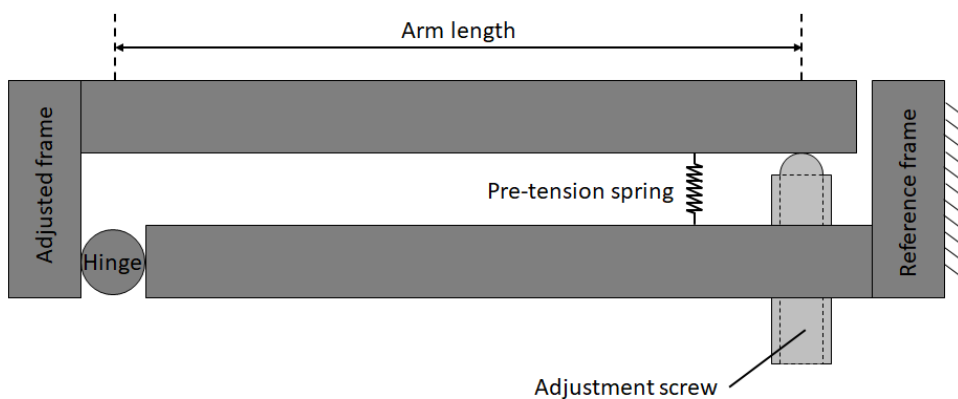


Figure 5.5: Schematic depiction of the folded single lever concept.

As shown in Figure 5.6, this means that there is no longer a need for an alternating pattern, which allows for a design where all the alignment screws are positioned above the collimator.

However, there is also another problem with these designs: the reference frame of the tip mechanism is attached to the adjusted frame of the tilt mechanism. This means that the tilt is unstable during the tip alignment. A solution would be to lock the tilt mechanism during the tip alignment, but this makes

the alignment procedure more complicated and thus more time-consuming. Also, any potential cross-talk between the tip and tilt adjustments can more easily be corrected for if tip and tilt can be adjusted at the same time.

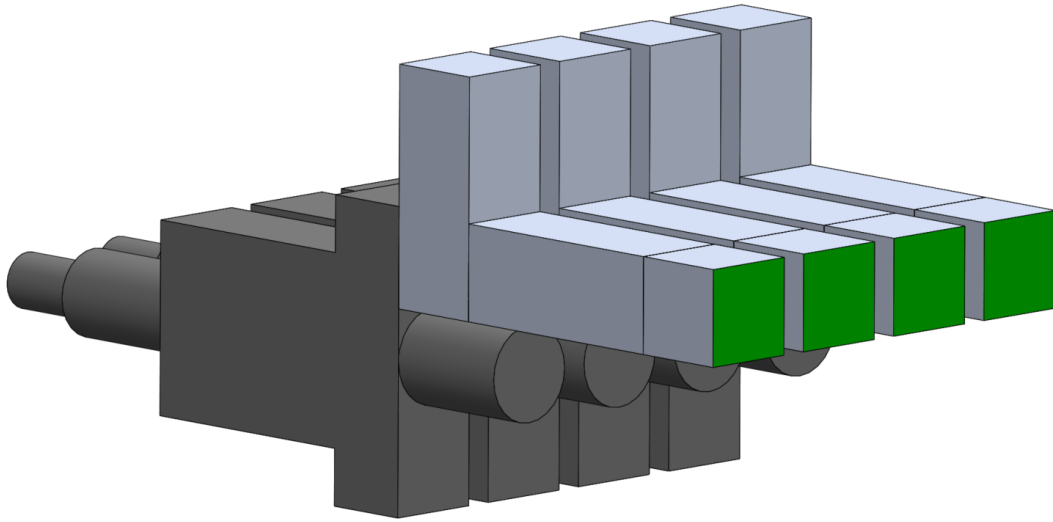


Figure 5.6: 3D depiction of the 2 DOF single lever concept, Where the tilt mechanism is replaced with a folded version.

Therefore the final conceptual design of the single lever concept uses a combined reference frame for both tip and tilt, see Figure 5.7. Note that the adjusted frame of the tip mechanism is attached to the adjusted frame of the tilt mechanism. However, these adjusted frames are not supposed to be touched during alignment. This design is also potentially more compact than the previous designs, because the lever arms are placed in parallel rather than in series.

Note that there are two sets of screws depicted. The left screw of each set is the adjustment screw shown in Figure 5.2. The right screw is equipped with a compression spring locked between the screw head and the main block. This screw pulls the lever arm towards the adjustment screw to provide the required pre-tension. This conceptual design does not yet include a locking system, which is discussed in Section 5.6.

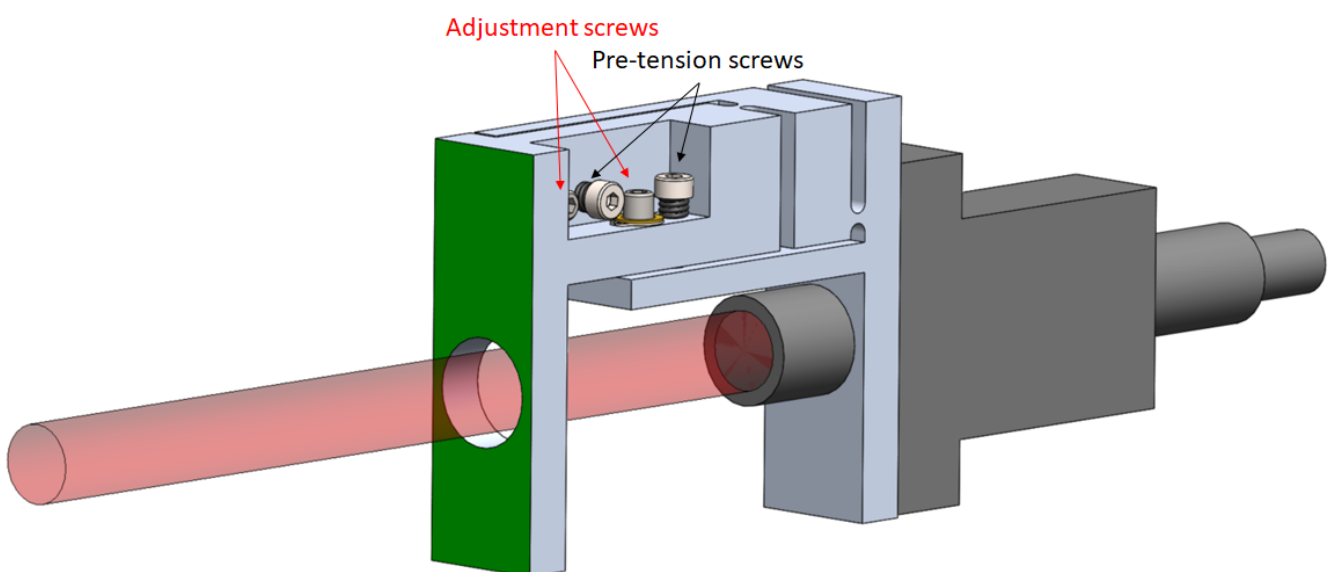


Figure 5.7: Conceptual design of the single lever concept, with a combined reference frame.

5.3 Stiffness ratio concept

The single lever concept can theoretically achieve the required resolution with both considered adjustment screws. However, since the required arm length (for the Thorlabs screw) of 35 mm is 2.5 times the available width of the mechanism, it is worth considering concepts that achieve a higher resolution with a smaller arm length. The effective arm length can be increased using reduction ratios.

The stiffness ratio concept (see Figure 5.8) is based on a low-stiffness beam: the beam will deform elastically when pushed against by the adjustment screw (see Figure 5.9). This means that a large movement of the screw will result in a relatively small rotation around the hinge. This can be tuned by choosing a specific ratio in stiffness between the beam and the hinge.

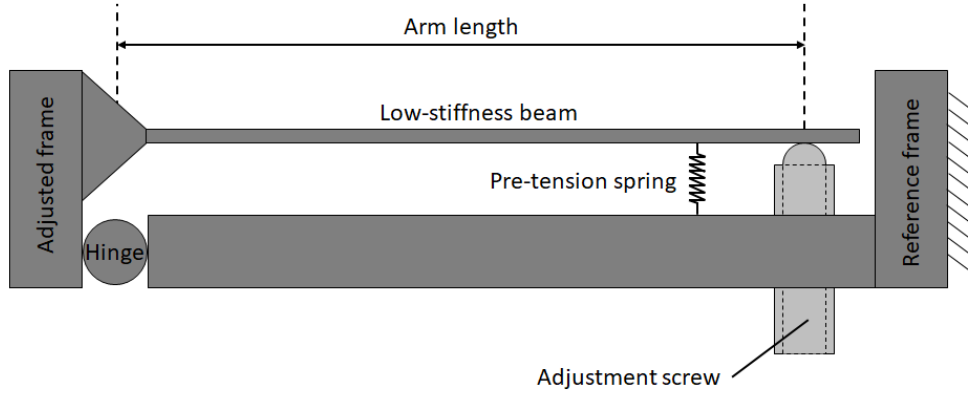


Figure 5.8: Schematic depiction of the stiffness ratio concept.

The rotational stiffness c of a typical compliant hinge is given by the following equation:

$$c = \left(\frac{Ebt^2}{12} \right) \cdot \left(-0.0089 + 1.3556 \sqrt{\frac{t}{2R}} - 0.5227 \cdot \left(\sqrt{\frac{t}{2R}} \right)^2 \right) \quad (5.2)$$

Where E is the Young's modulus, b is the out-of-plane dimension of the hinge, t is the thickness of the neck of the hinge, and R is the radius of the hinge holes. These and the other geometries used in the following equations are defined in Figure 5.9. Note that this figure also shows the expected combined effects of a rotated and deformed beam.

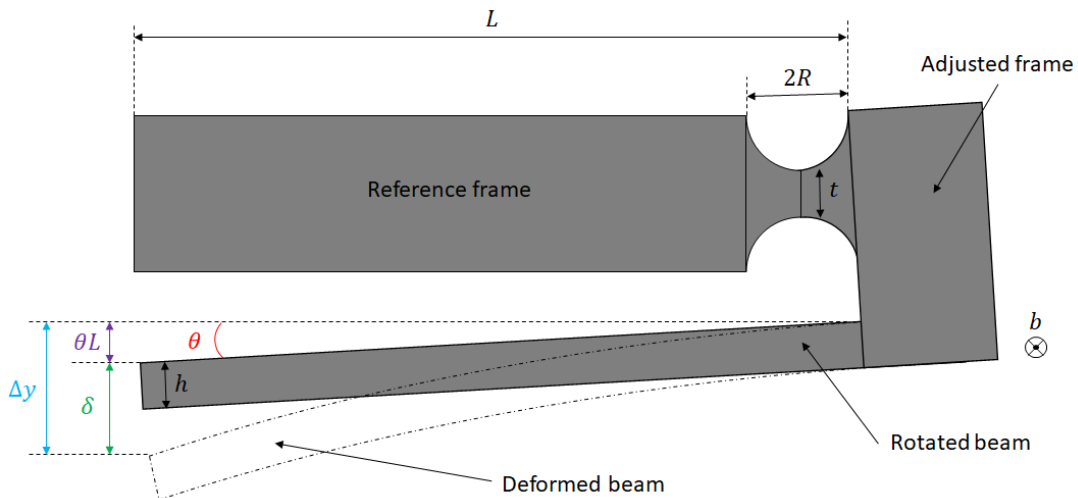


Figure 5.9: Geometries defined for the stiffness ratio model. The out of plane dimension is b .

The low stiffness beam is modeled using the following equations:

$$\Delta y = \delta + \theta L, \quad \delta = \frac{FL^3}{3EI}, \quad I = \frac{1}{12}bh^3 \quad (5.3)$$

Where Δy is the sensitivity of the adjustment screw, δ is the elastic deformation of the low-stiffness beam, θ is the desired resolution, L is the arm length of the beam, F is the force applied by the alignment screw, I is the moment of inertia of the beam, and h is height of the beam. Note that the deformations and displacements are assumed to be small.

When assuming that $R \ll L$, the moment equilibrium around the compliant hinge can be expressed as:

$$M = FL = \theta c, \quad F = \frac{\theta c}{L} \quad (5.4)$$

Where M is the moment. Substituting this equation for F into the equation for δ yields:

$$\delta = \frac{\theta c L^2}{3EI} \quad (5.5)$$

Substituting this result in the equation for Δy yields:

$$\Delta y = \theta L \cdot \left(1 + \frac{cL}{3EI}\right), \quad \frac{\Delta y}{\theta L} = 1 + \frac{4cL}{Ebh^3} \quad (5.6)$$

And from this the required hinge stiffness can be determined, based on the other design parameters:

$$c = \left(\frac{Ebh^3}{4L}\right) \cdot \left(\frac{\Delta y}{\theta L} - 1\right) \quad (5.7)$$

Substituting the hinges stiffness for the expression in Equation (5.2) yields the design equation for resolution:

$$\theta = \frac{\Delta y}{\left(-0.0089 + 1.3556\sqrt{\frac{t}{2R}} - 0.5227 \cdot \left(\sqrt{\frac{t}{2R}}\right)^2\right) \cdot \left(\frac{t^2 L^2}{3h^3}\right) + L} \quad (5.8)$$

The effect of each parameter on the resolution is plotted in Figure 5.10.

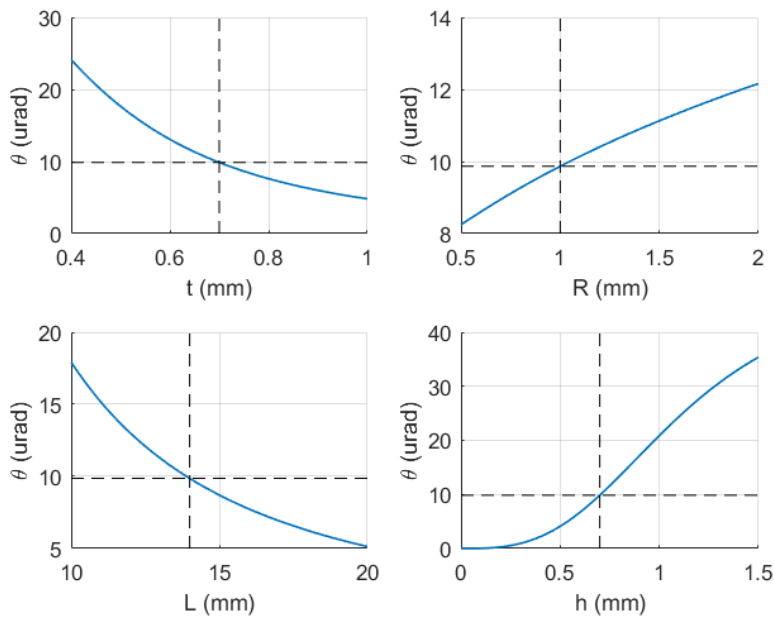


Figure 5.10: Resolution as a function of the design parameters. The chosen parameters are indicated with dotted black lines. Note that here Δy is 700 nm, based on 1 degree rotations of a 250 μm pitch screw.

The design is however also limited by the required total range. If the material is deformed too much, the stress in either the beam or hinge exceed the allowed margin. The stress in the beam σ_{beam} is given by the following equation:

$$\sigma_{beam} = \frac{3Eh}{2L^2} \cdot \delta = \frac{3Eh}{2L^2} \cdot (\Delta y - \theta L) \quad (5.9)$$

The stress in the hinge σ_{hinge} is given by:

$$\sigma_{hinge} = \theta E \cdot \left(-0.0028 + 0.6397\sqrt{\frac{t}{2R}} - 0.0856 \left(\sqrt{\frac{t}{2R}} \right)^2 \right) \quad (5.10)$$

The stresses are plotted in Figure 5.11.

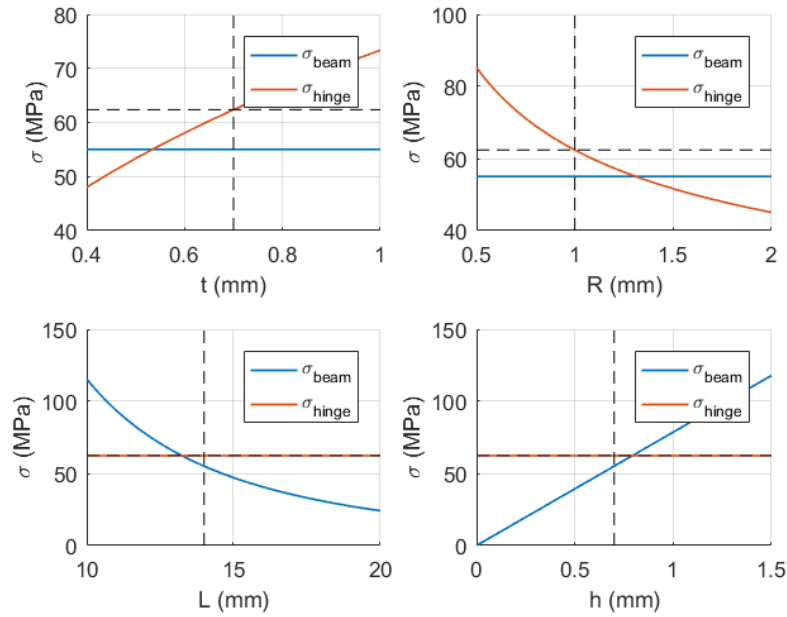


Figure 5.11: Maximum stress levels for 0.15° adjustments, as a function of the design parameters. The chosen parameters are indicated with dotted black lines.

Note that the results for resolution and stress can be verified in a quick FEM study using Solidworks. The design with the parameters as presented in Figure 5.11 yields a result of 63 MPa maximum stress instead of the anticipated 62 MPa (1% deviation). For the resolution the result is $9.4 \mu\text{rad}$ resolution instead of $9.9 \mu\text{rad}$ (4% deviation). These deviations are assumed to be due to limited simulation resolution, as well as errors in the used algebraic equations.

Even though the presented conceptual design achieves a reduction ratio of 5:1, it does have two major disadvantages. For one, a stiffness ratio concept inherently has low stiffness elements (which is bad for stability). Secondly, the mechanism is not geometrically defined, which means that the motion depends on the stiffness of and strain in the non-stiff beams and compliant hinges. This makes it sensitive to manufacturing errors and creep effects.

5.4 Lever ratio concept

A reduction ratio can also be achieved using a geometrically defined design with stiff beams. The schematic depiction in Figure 5.12 shows a design that achieves a reduction ratio of A:B. The rotation of the lever arm causes the top two hinges to move by a distance equal to B times the rotation. This movement is then translated to the adjusted frame, where the rotation of the adjusted frame is now the moved distance divided by A.

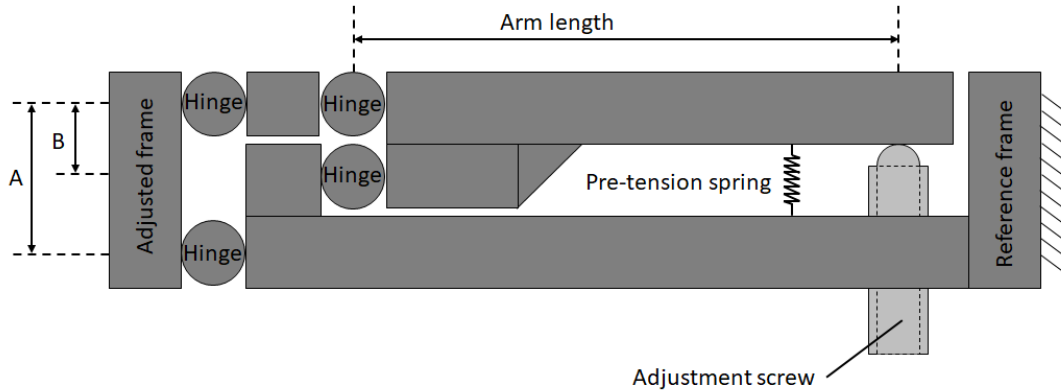


Figure 5.12: Schematic depiction of the lever ratio concept.

The result is that the adjusted frame rotates less than the lever arm, thus improving the resolution. This is summarised in the following equation:

$$\text{Resolution (urad)} \approx \frac{\text{Sensitivity (nm)}}{\text{Arm length (mm)}} \cdot \frac{B \text{ (mm)}}{A \text{ (mm)}} \tag{5.11}$$

The downside however is that increasing this reduction ratio also increases the stress in the mechanism. This is because the lever arm needs to rotate more with respect to its hinge as the reduction ratio increases. This is shown in Figure 5.13. In fact, doubling the arm length reduces the required ratio A:B (and thus also the stress levels) by a factor of 2.

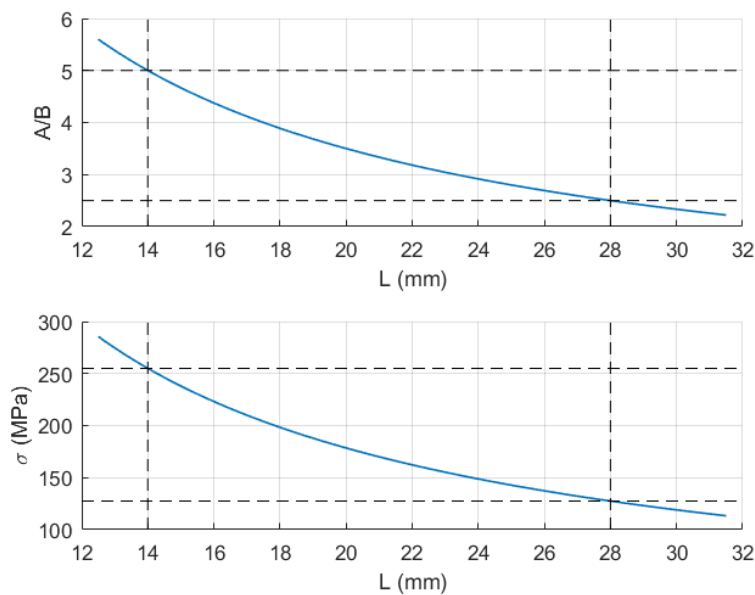


Figure 5.13: Trade-off plots for the lever ratio concept. Note that the sensitivity is again chosen to be 700 nm, based on 1 degree rotations of a 250 µm pitch screw.

5.5 Double wedge concept

As mentioned, the fourth concept is not based on aligning the collimator, but on steering the beam. This is done using two optical wedges that can be used in combination with each other to steer the beam anywhere inside a given circle, see Figure 5.14.

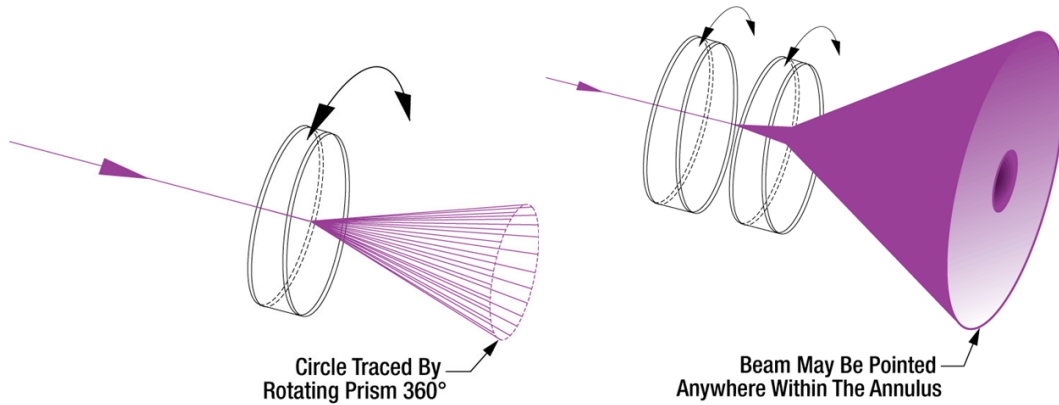


Figure 5.14: Beam steering as proposed by Thorlabs [26].

Note that the annulus has a hole in the middle where the beam can not be steered. This can be understood from Figure 5.15. In the top left figure, the wedges are rotated such that they cancel each others effect on the beam. However, during the propagation from wedge to wedge, the beam gains a spatial offset, which causes the hole in the center of the annulus.

In this design challenge, however, the required range is much smaller than in typical applications. Therefore the apex angles can be much smaller. Furthermore, the large propagation distance after the wedges mean that any spatial offset between the wedges is negligible compared to the spatial offset after the wedges.

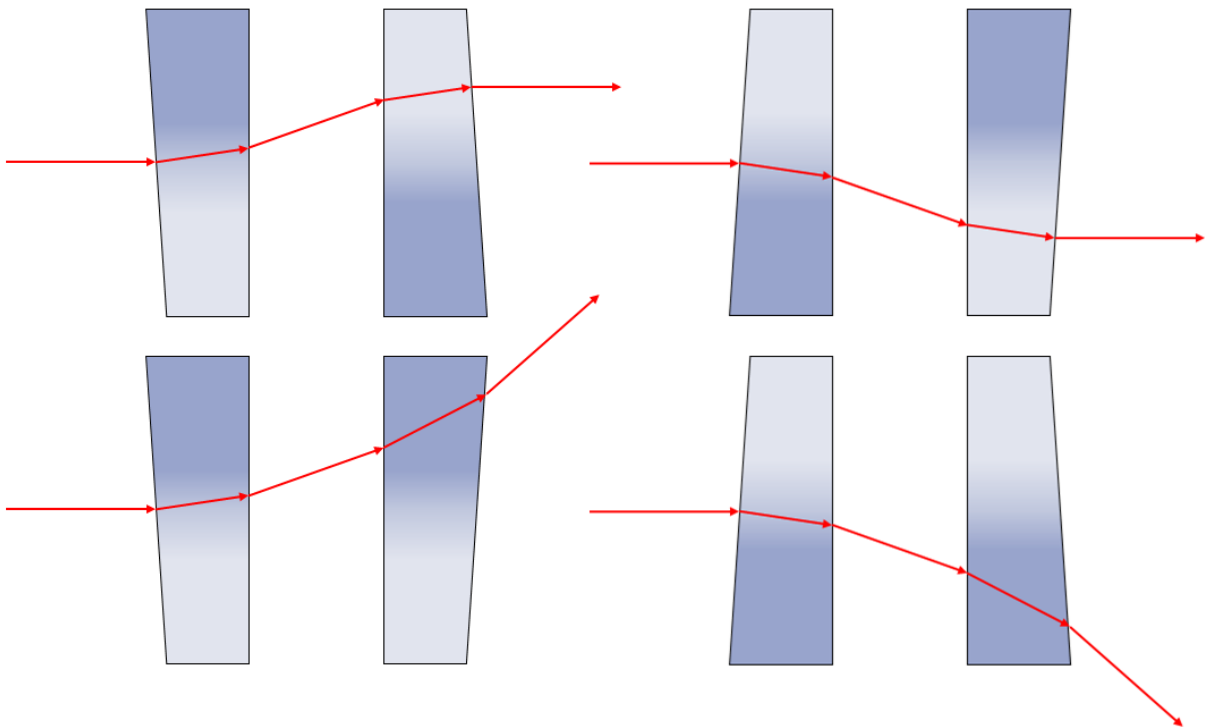


Figure 5.15: Schematic depiction of two wedges used for beam steering. The second wedge can double or cancel the effect of the first (and anything in between), depending on their rotation.

Figure 5.15 also shows how the two wedges can be used to achieve the different angles. As mentioned, they can be rotated such that they cancel each others angular offset. However, they can also be rotated such that they double each others angular offset. This double angular offset can be tuned to correspond to the total required range. When rotating the wedges in any other rotation than the depicted extremes, the total range can be covered.

The model used to calculate the resolution and range of the system is based on the assumption shown in Figure 5.16. The wedge will always maximally steer the beam in one direction, while not affecting the beam in the other direction. This can be used to trace the beam with two variables: the angle with respect to the optical axis and the rotation around the optical axis.

These variables can be calculated by splitting up their values in the steered and unaffected parts, based on the local horizontal axis of the wedge with respect to the global horizontal axis (see Figure 5.17). The results can then be recombined into a new set of variables, which are then sent through the second wedge.

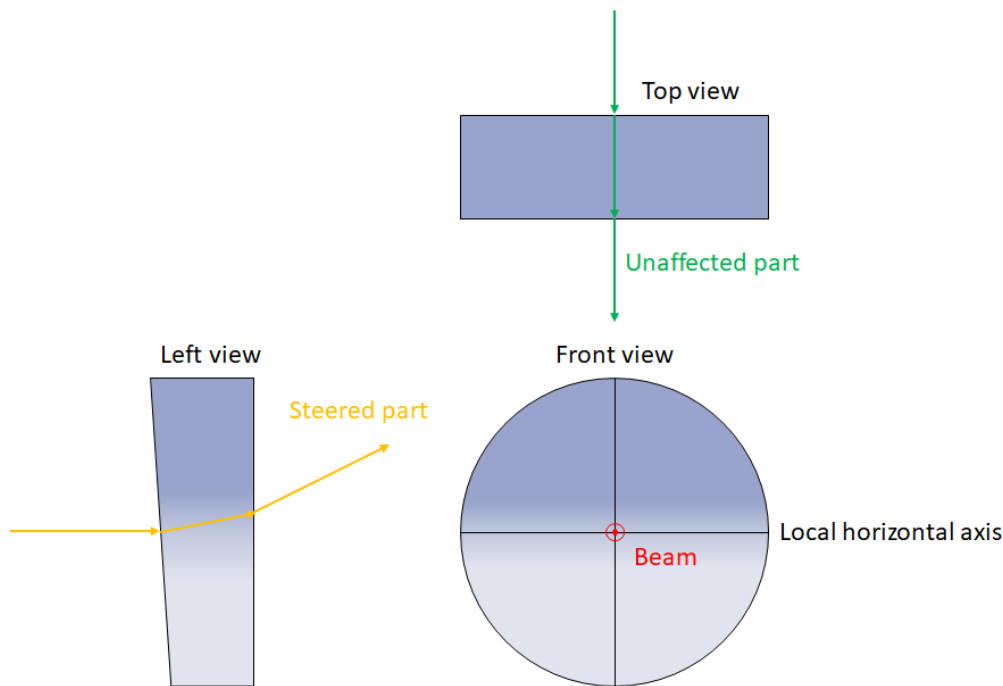


Figure 5.16: Schematic depiction of a wedge with three views, showing that only the part of the beam that is orthogonal to the local axis is affected.

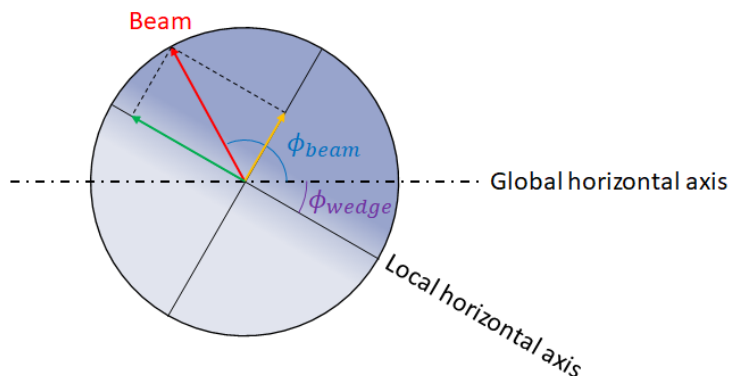


Figure 5.17: Schematic depiction of a wedge, showing the local and global horizontal axes. Only the part of the beam that is orthogonal to the local horizontal axis is affected.

Therefore the model can give the angular deviation of the beam, based on the rotation of the two wedges. This is shown in Figure 5.18, where the wedges are rotated in the opposite direction with respect to each other. The result is that the beam travels in the tilt direction in a straight line. This is because the tip contributions of the wedges are canceled by each other.

The step size for the rotations is chosen to be 2.5 degrees here, to clearly show the distinct spots. The distance between these spots is considered the resolution of the alignment system. Note that this resolution is not constant across the range. Therefore the maximum distance between the spots is chosen as the limiting resolution. This maximum distance is in the center of the range, near the 0,0 point (depicted as a red dot).

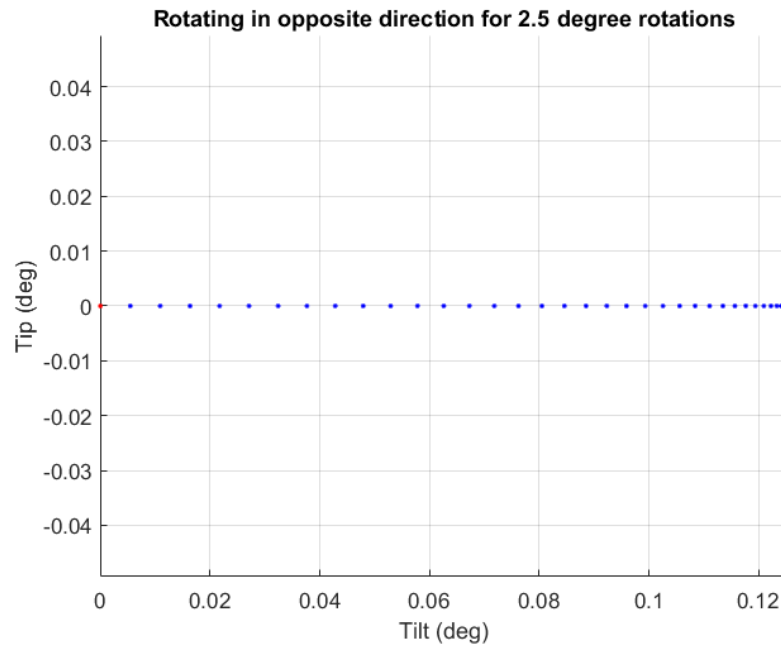


Figure 5.18: Beam steering by rotating wedges in opposite direction in steps of 2.5 degrees.

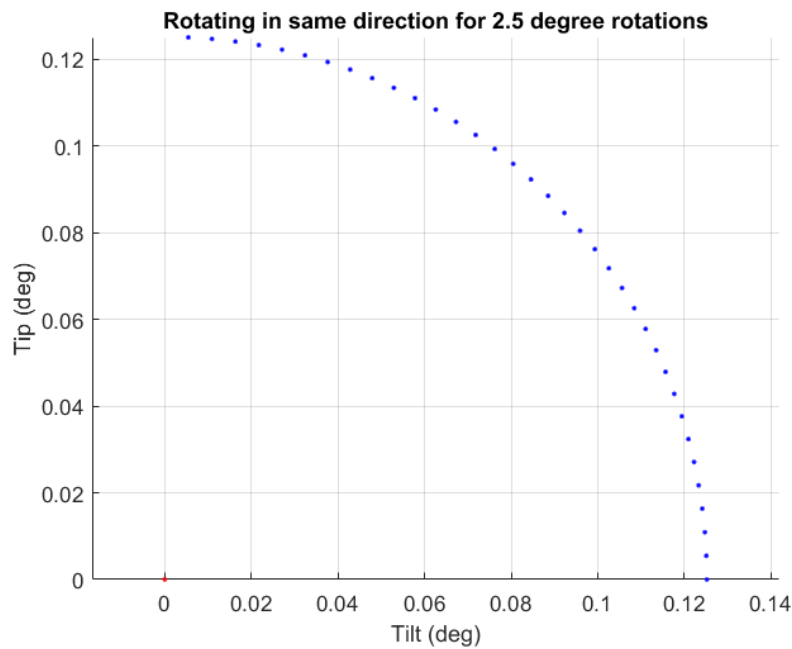


Figure 5.19: Beam steering by rotating wedges in same direction in steps of 2.5 degrees.

When instead of 2.5 degrees rotation steps, the model is run of 0.25 degrees rotations, the desired dynamic range is achieved. The model is run for three apex angles, in order to determine the sensitivity to tolerances. For an apex angle of $0.141 \pm 0.008^\circ$, the resolution is $9.5 \pm 0.5 \mu\text{rad}$ and the range $0.125 \pm 0.007^\circ$.

The proposed alignment strategy is to turn the wedges in the opposite direction for setting the radius, and turn the wedge in the same direction to set the angle (see Figure 5.19). This gives two independent alignment variables which makes for an intuitive alignment.

5.6 Concept choice

The presented four concepts were designed to match the required range and resolution. However, the setting resolution and range is only the first half of the design challenge. The second half is the stability of the system limited by locking drift, thermal loads, creep effects and stiffness. The last two stability factors were discussed already, but the first two will be discussed in more detail.

5.6.1 Locking stability

The available locking systems and their effectiveness are severely reduced due to the footprint constraints. The solutions that are anticipated to meet the strong sensitivity requirements are the split nut, the push/pull pair and the leaf spring. The split nut would increase the dimensions of the alignment screw, while these dimensions are already at their maximum. The accessibility of this nut would be a limiting factor as well.

The push/pull pair could be combined with the pre-tension solution shown in Figure 5.7. However, the accessibility of the pre-tension screw is very limited once the seven mechanisms are placed next to each other and these screws might not be realistically achieved with existing spring dimensions. One solution would be to implement a separate pull screw (distinct from the pre-tension solution), but this would further complicate the design as there is already limited space available.

Therefore the anticipated solution for locking is the leaf spring, equipped with the mentioned moment-release plate (see Figure 4.5). The sensitivity of these locking plates are in the order of $1.4 \mu\text{m}$ for simple leaf springs, and in the order of $0.3 \mu\text{m}$ for leaf springs equipped with moment-release plates [25, 27].

Therefore the required effective arm length for allowing a locking drift of $5 \mu\text{rad}$ is 60 mm. This means that the preferred strategy would be to lock the lever beam itself, to prevent introducing a separate locking beam. Since the lever beam of the stiffness ratio concept is inherently not stiff, this beam is not suited for locking.

It is however worth the effort to introduce a reduction ratio, since a lever beam of 60 mm is very long compared to the available width of 14 mm. This long lever beam would also have a limited stiffness, making it also unsuitable for locking.

Thus based on the locking stability, the only remaining collimator adjusting concept is the lever ratio concept. This uses a reduction ratio with a limited lever beam length and thus allows for a stiff locking.

For the double wedge concept, a locking concept similar to the split nut can be used around the wedges. This leads to minimal locking drift, and therefore this concept can not be crossed out on the basis of locking stability.

5.6.2 Thermal stability

When it comes to thermal stability, there is a clear distinction to be made between the first three concepts and the double wedge concept. In the first three concepts, the heat is conducted through the alignment mechanism (including the hinges) which causes thermal gradients. In the double wedge concept, however, the collimator can be mounted directly to the fixed world (and thus the heat sink). Therefore the double wedge concept inherently scores better for thermal stability.

In the first three concepts, a distinction can be made between the single lever concept and stiffness ratio concept on one side, and the lever ratio concept on the other. In the first two concepts, the adjusted frame is connected to the reference frame with a single hinge. This means that the thermal gradient across this

hinge only causes a translation along the optical axis of the collimator. Since this error is not critical, this is no problem.

In the lever ratio concept, however, the adjusted frame is connected with two separate thermal paths to the reference frame. The result is that this concept gives more thermal drift than the other concepts. The full effect is further analysed in Chapter 7.

5.6.3 Conclusion

Based on these considerations only two concepts remain. The lever ratio concept is chosen based on the limiting factor of the locking stability, but as mentioned there is some concern regarding the thermal stability.

The double wedge concept scores well on both locking and thermal stability, but has a limited dynamic range based on realistic rotation step sizes. Furthermore, the introduction of new optical components also introduces secondary issues such as wavefront errors, back-scattering, and a greater risk for required maintenance.

Therefore no conclusive concept choice can be made between the lever ratio concept and the double wedge concept. Despite this, the lever ratio concept is chosen as the main concept because the lead time (15 weeks) for the required custom optical components would push the project beyond its deadline. Furthermore, the optical concerns led to the lever ratio concept being the preferred option on system level.

The double wedge concept is analysed in parallel to combat some of these optical concerns, and will serve as a backup concept if the lever ratio concept does not meet the requirements. This also makes for an interesting trade-off between mechanical and optical solutions, which adds to the academic value (especially in the field of Opto-Mechatronics) of this thesis.

Chapter 6

Detailed Design

6.1 Introduction

As mentioned in the previous chapter, this thesis presents a detailed design of both the lever ratio concept and the double wedge concept. Because the lever ratio concept is chosen to be the main concept, this is worked out to a directly manufacturable design. The other presented designs are intended to answer open standing questions about how the concepts can be implemented in one design, while not getting distracted with minor details.

6.2 Double wedge concept

As mentioned, the double wedge concept is intended to steer the laser beam after it has left the collimator. This is achieved by rotating the two wedges that make up the optical design, and these wedges need to be rotated with steps of at most 0.25° . After alignment, the wedges need to be locked with a minimum amount of lock drift.

Furthermore, to avoid an increase in maintenance, the design needs to make sure that there is an equal amount of exposed optical surfaces as the other concepts. This can be done by shielding of the collimator lens, and only exposing one surface of the last wedge.

Also, the mechanisms need to be mounted to a mounting block (or breadboard) within the tolerances set at $\pm 0.033^\circ$, with a spatial separation of 14 mm (defined between the collimator lenses) and an angular separation of 2.24 mrad.

And finally, the mechanisms need to guide away the heat from the collimator in order to stay within the set temperature range.

6.2.1 Single collimator design

These design requirements are met in the detailed design presented in Figure 6.1. The design consists of three aluminium blocks, two wedge assemblies, one collimator and various fasteners.

The main block is also shown in Figure 6.2 and serves as the interface towards the mounting block (or breadboard). This interface is controlled using a set of 2 dowel pin holes. One dowel pin hole is round and is located directly underneath the collimator lens. The other dowel pin hole is a slot and is located as far as possible from the round dowel pin hole. This constellation is designed to position and align the mechanism to the other mechanisms within the tolerance budget. The main block is also used as the mounting interface for the collimator, the other two aluminium blocks and one of the wedge assemblies.

The locking block is used to lock the wedge assemblies into place once they are aligned properly. The block surrounds the wedge assemblies within a tolerance fit, meaning there is little play between the wedge assemblies and the locking block. The remaining play can then be taken away by tightening the locking bolts, after which the wedge assemblies are locked based on friction.

The guiding block simply acts as the mounting interface for the second wedge assembly, and thus prevents the wedge assembly to deform during alignment.

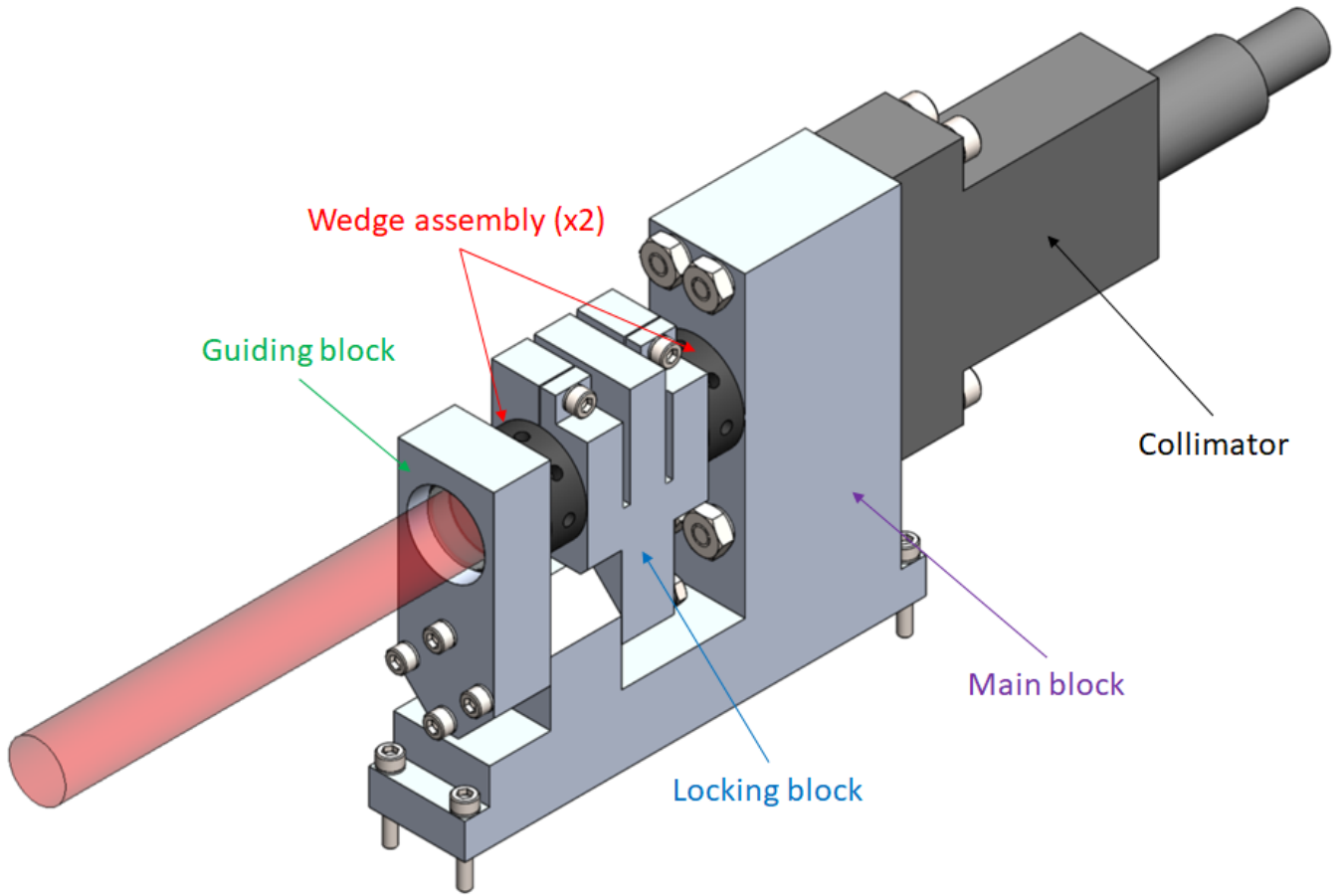


Figure 6.1: Detailed design of the double wedge concept.

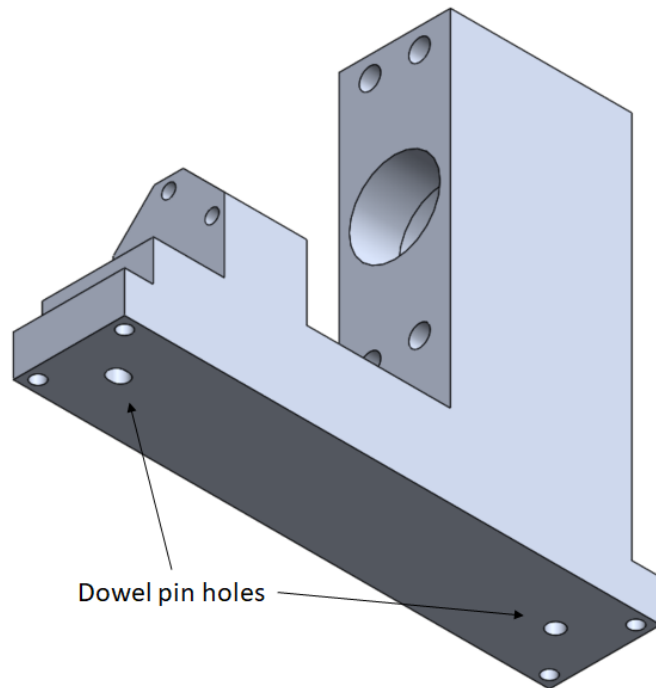


Figure 6.2: Detailed design of the main block of the double wedge concept, with the dowel pin holes indicated.

The wedge assembly is also shown in Figure 6.3, and consists of an aluminium bushel and a fused silica optical wedge. The wedge is mounted in the bushel using three small glue spots in the glue holes. This mounting technique is expected to give thermal stresses well below acceptable margins for the anticipated temperature range.

The bushel is equipped with alignment tool holes that are designed to match the dimensions of the dedicated alignment tool. This tool is a rod with a small tip that fits into the holes, and can be used to align the wedge assembly using the long lever arm of the rod. The alignment tool is shown in Figure 6.5.

Note that the design in Figure 6.1 is designed for assembling. The parts are dimensioned such, that the guiding block and locking block can rotate along the optical axis (which is the central axis of the wedge assemblies).

This allows for the following assembling procedure: first of all, the first wedge assembly is placed into the main block. Then the locking block is placed around the first wedge assembly (rotated approximately 90 degrees compared to how it is depicted). Then the second wedge assembly is placed into the locking block. And finally the guiding block is placed around the second wedge assembly. Then the locking block and guiding block are rotated into position, and everything can be mounted.

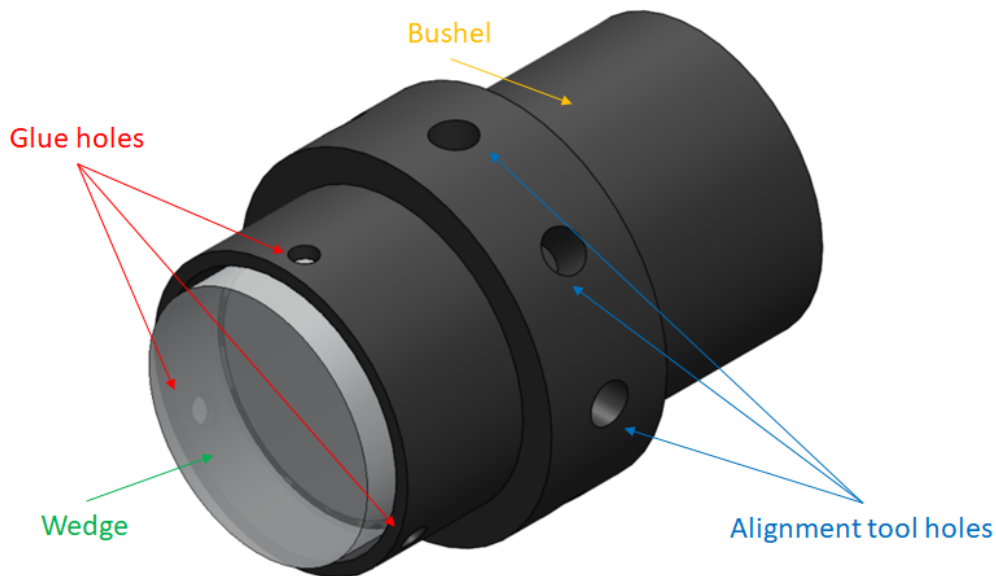


Figure 6.3: Detailed design of the wedge assembly.

6.2.2 Breadboard design

As mentioned, the mechanisms are mounted on a mounting block (also called a breadboard). This breadboard is designed for this specific application and consists of 14 dowel pin holes, 28 threaded holes and 4 larger holes (see Figure 6.4). The dowel pin holes will be filled with dowel pins and will then be used to align the mechanisms. The threaded holes will be used to fix the mechanisms to the breadboard. And the larger holes match the dimensions of typical optical tables, such that the breadboard itself can be mounted as well.

Mounting all seven mechanisms to the breadboard results in the breadboard assembly shown in Figure 6.5. Note that the locking block is flipped for 3 of the 7 mechanisms, to allow for better accessibility of the locking screws. This locking block is designed such that it can be used in both the original and the flipped orientation (and thus no mirrored version is required).

The alignment tool is also shown, which as mentioned is a long thick rod with a small thin tip that fits into the alignment tool holes of the wedge assemblies. Two alignment tools are required, to align both wedges at the same time. This simultaneous alignment allows for the alignment strategy presented in the conceptual design. The alignment tool can not make a full rotation in one go, but instead needs to be taken out of the used alignment tool hole and placed into another to continue.

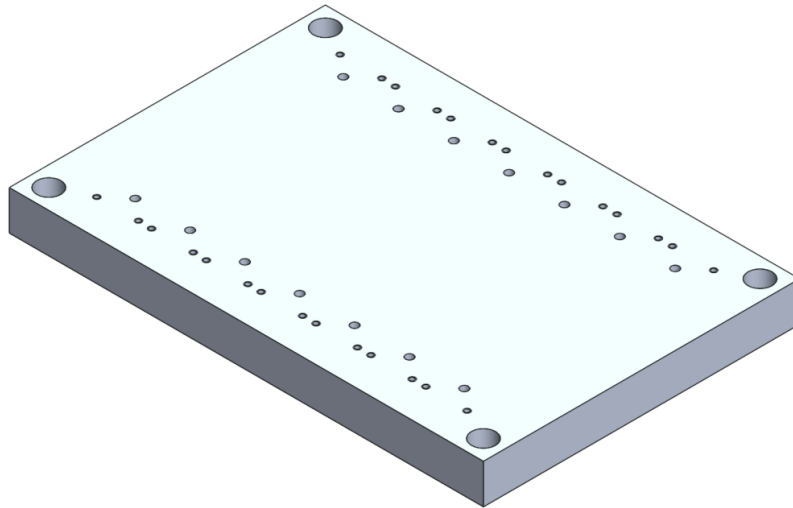


Figure 6.4: Detailed design of the dedicated breadboard.

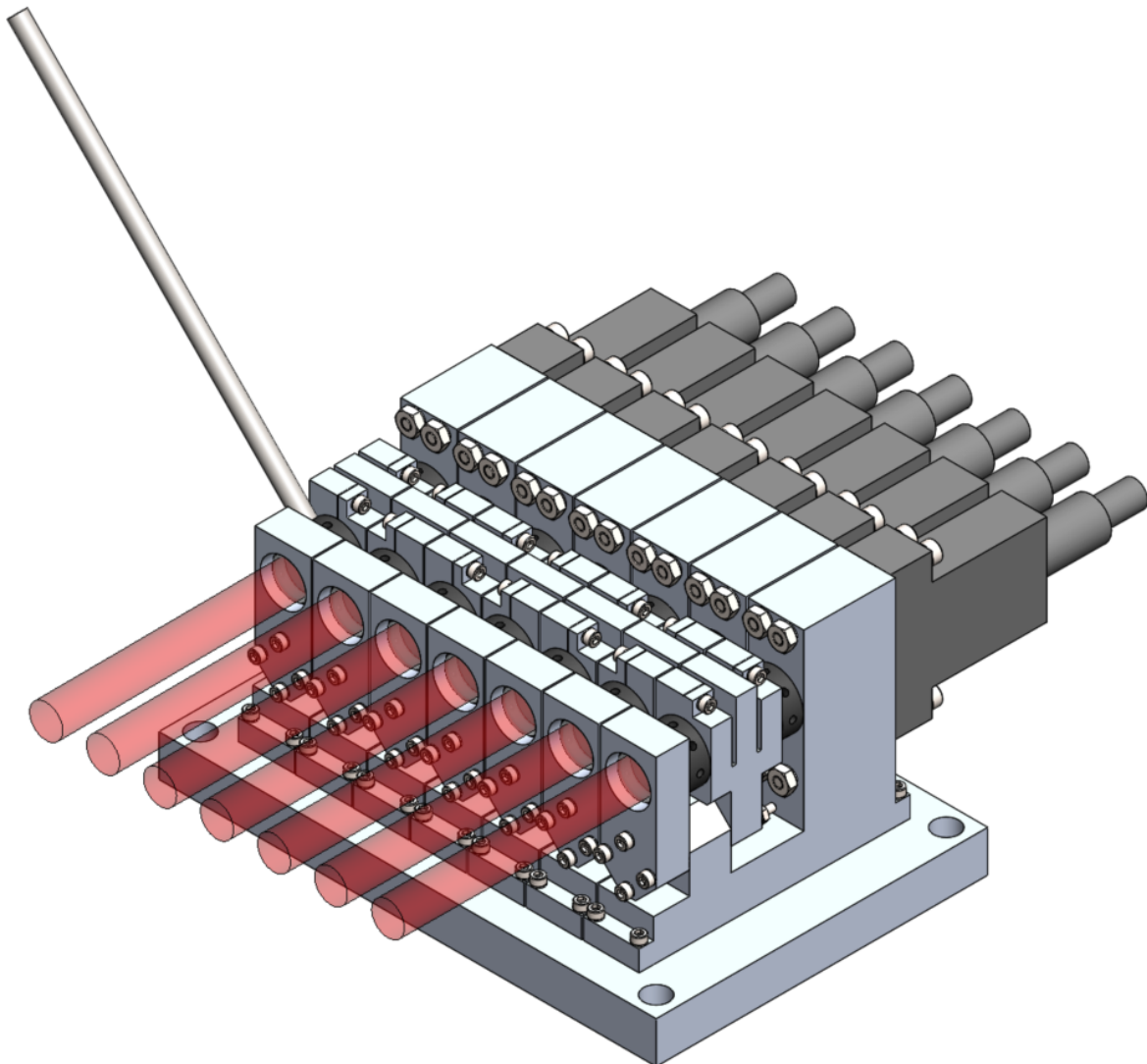


Figure 6.5: Detailed design of the breadboard assembly of seven collimators. Note that the locking block is flipped for 3 of the 7 mechanisms, to allow for better accessibility of the locking screws. The alignment tool is also shown.

6.2.3 Material selection

All parts are chosen to be aluminium, except for the alignment tool, the fasteners, and the wedges. Aluminium is chosen to match the material of the collimator, which will also be aluminium. As such, there is no difference in coefficients of thermal expansion which is beneficial for the stability of the mechanism. Furthermore, aluminium is good heat conductor, readily available and easily machinable. The machinability is especially useful for the wedge assemblies and locking blocks, since they have a relatively complicated geometry.

The alignment tool is chosen to be steel, because it is readily available, somewhat easily machinable, and a high Young's modulus is desired. Also the fasteners are chosen to be steel, but any readily available type of fastener is allowed. Note that a mismatch in coefficient of thermal expansion can easily be compensated for by choosing a sufficiently high pre-tension force.

The wedges are chosen to be fused silica, because it has good optical properties for the desired wavelength range, including low absorption and low dispersion. The wedges are quoted by an optical manufacturer for a surface flatness of less than $\lambda/10$ (at 1550 nm), a surface quality of 40-20 SCRATCH-DIG, and an anti-reflective coating for 1050-1700 nm. The total costs for 30 wedges are expected to be below 10K euros with a lead time of a few months.

6.3 Lever ratio concept

For the lever ratio concept, the conceptual design is very similar to the conceptual design presented for the single lever concept in Figure 5.7. Again, the reference frames are combined, and the adjustment screws are placed in a single cavity. Note that the 50 μm pitch adjustment screws (discussed in Section 5.2) are chosen to maximize the setting resolution and reduce the screw play (see Section 7.5). The conceptual design is expanded upon by adding a locking solution and an additional heat sink. Also, the arm length is set to 32.5 mm and the lever ratio is set to 2 to reduce the stress levels in the flexures and to design for the screw play sensitivity (see Section 7.5). Two main manufacturing techniques are considered: spark erosion and rapid prototyping.

6.3.1 Spark erosion design

The spark erosion design (shown in Figure 6.6 and Figure 6.7) consists of two aluminium blocks, two alignment screws, two pre-tension springs, two locking plates, two moment-release plates and many fasteners. The main block contains the lever ratio mechanism, and the mounting interfaces for all the other components. This block is not changed with respect to the conceptual design, except for the interface for the heat sink and the locking solution.

The heat sink was added to improve the thermal stability, as well as increase the eigenfrequencies of the mechanism. The heat sink block is shown separately in Figure 6.8. It has an aperture of 9 mm, to comply with the design requirements. Furthermore, it has a feature that extends into the main block, and which can be used to bolt the main block to the heat sink block. The heat sink block can also be bolted to the main block at the front.

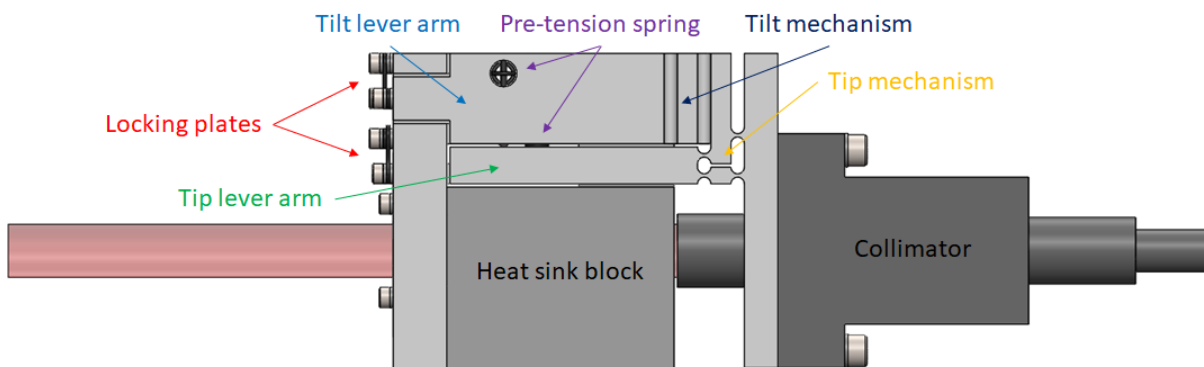


Figure 6.6: Spark erosion design for lever ratio concept, as seen from the right side.

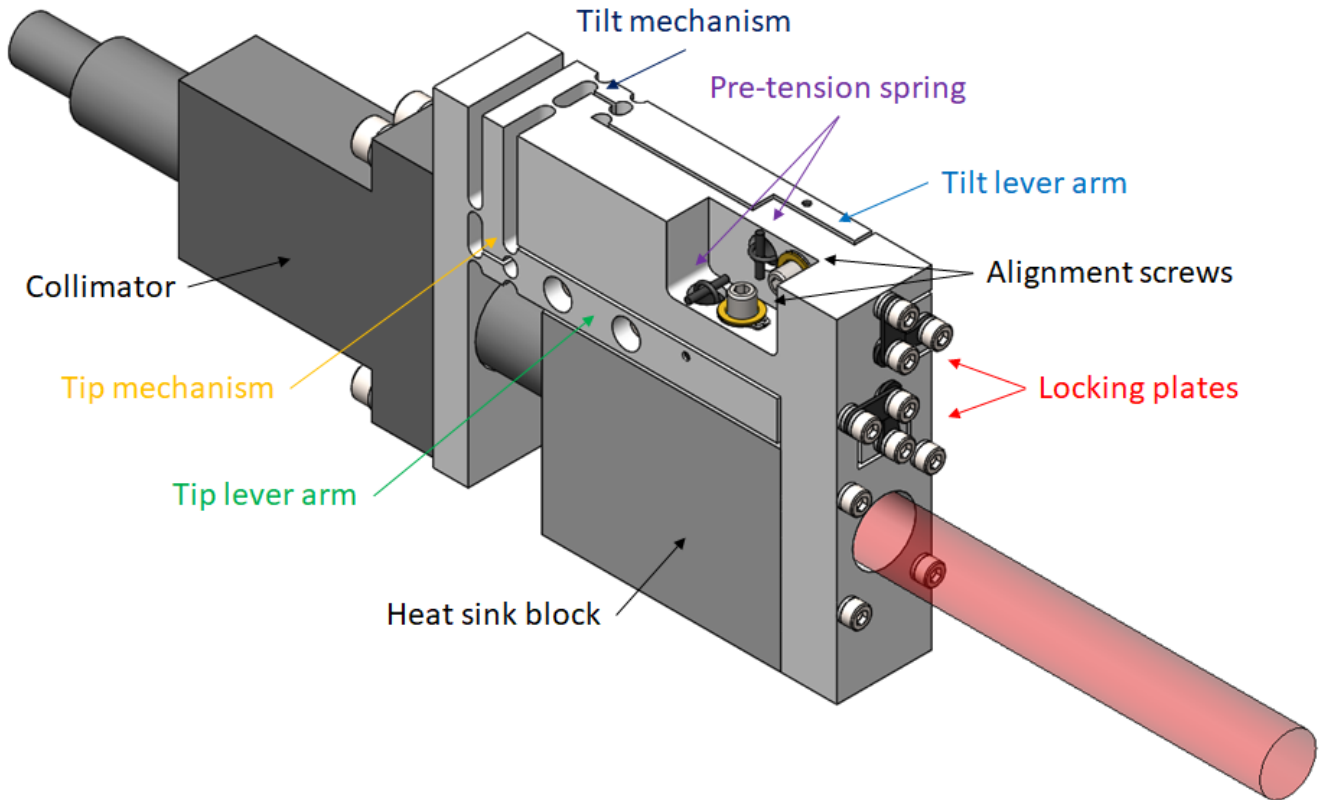


Figure 6.7: Spark erosion design for lever ratio concept, in the isometric orientation.

Note that this design has some major manufacturing challenges. This is because there are multiple small cavities that do not go all the way through. Therefore wire erosion is not possible, and instead an iterative process is required due to an expected wear of the spark erosion tool. The manufacturing challenges also mean that the proposed heat sink needs to be a separate block, instead of part of one monolithic block. This reduces the effectiveness of the heat sink.

Nevertheless, it was possible to obtain a quotation from a spark erosion supplier for an acceptable price. Even though spark erosion would be the preferred option for mass production, instead it was chosen to make the parts using rapid prototyping. This technique allows for a monolithic design with a much shorter lead time.

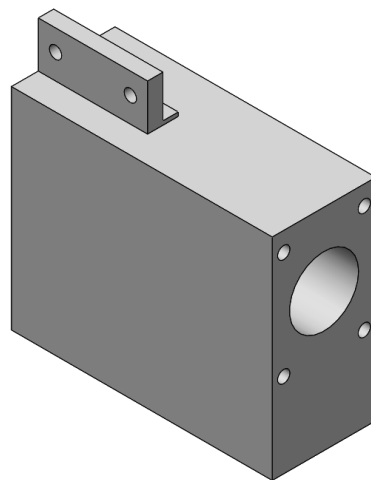


Figure 6.8: Heat sink block for the spark erosion design.

6.3.2 Rapid prototyping design

The rapid prototyping design is shown in Figure 6.9. As mentioned, the heat sink block and main block can be combined into a single, monolithic block. However, note that this new main block is modified with respect to the spark erosion and conceptual designs. This is because the previously designed parts are not printable due to overhanging features, meaning that support structures would need to be printed. Removing these support structures would again be very challenging, so this is not the preferred strategy.

Instead, the main block is re-designed to use 45 degree angle features that replace overhanging features and to further comply to the other design constraints provided by the manufacturing company (shown in Table 6.1). During the printing process, one of the six sides of the mechanism will be situated at the bottom. The initial block was analysed for all six options, and it was concluded that the best option was to print up from the mounting surface of the collimator. This is because as such the flexures and lever arms can be printed as up-standing walls, thus preventing them to be overhanging features. The same could have been achieved when printing from the locking plates surface, but this would lead to conflicts with the nuts used for mounting the collimator.


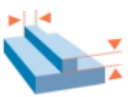
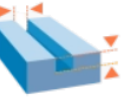


Feature:	Wall thickness	Embossed details	Engraving details	Hole diameter	Play
Definition:					
Minimal size:	0.7 mm	0.5 mm	0.5 mm	1 mm	0.3 mm

Table 6.1: Design constraints provided by the manufacturing company [28].

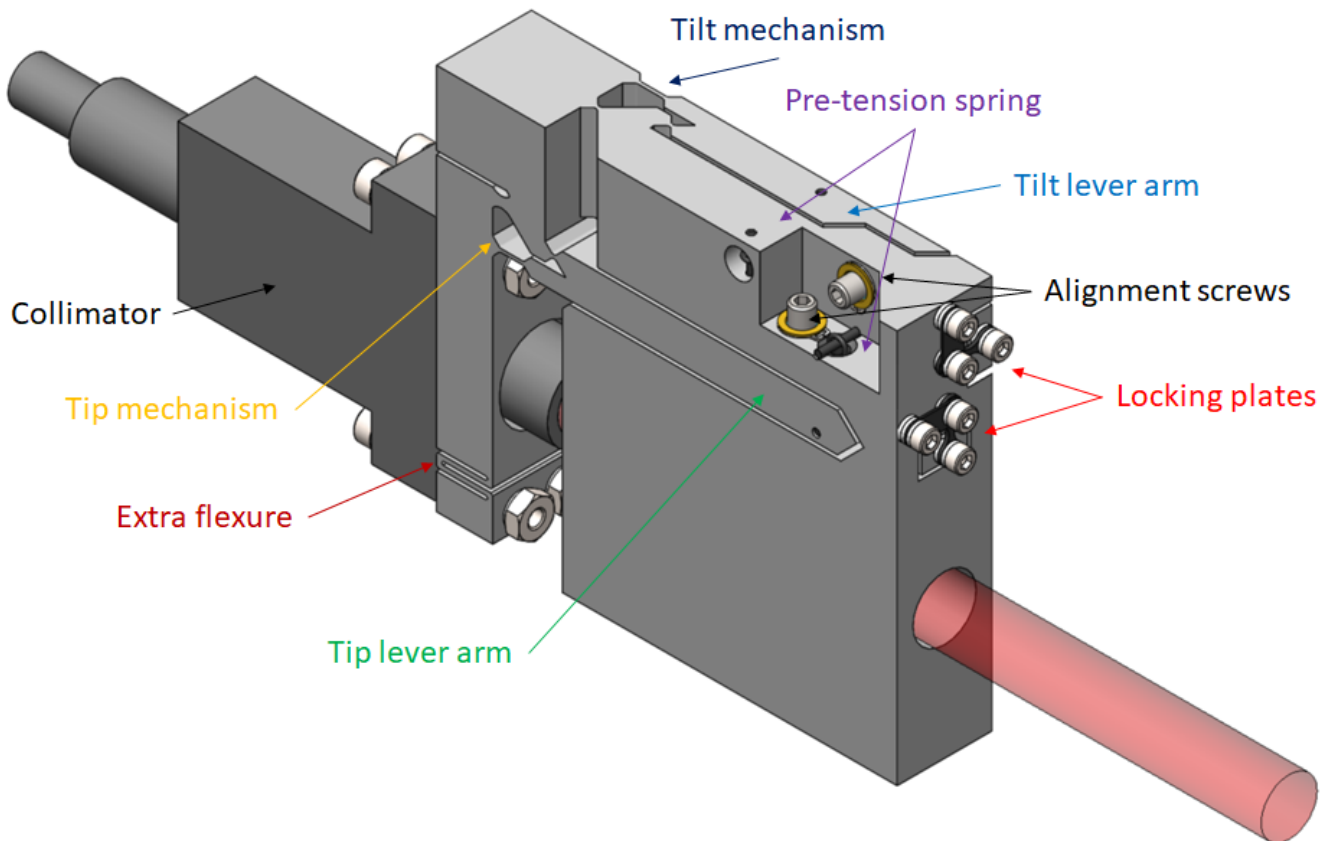


Figure 6.9: Detailed design of the lever ratio concept.

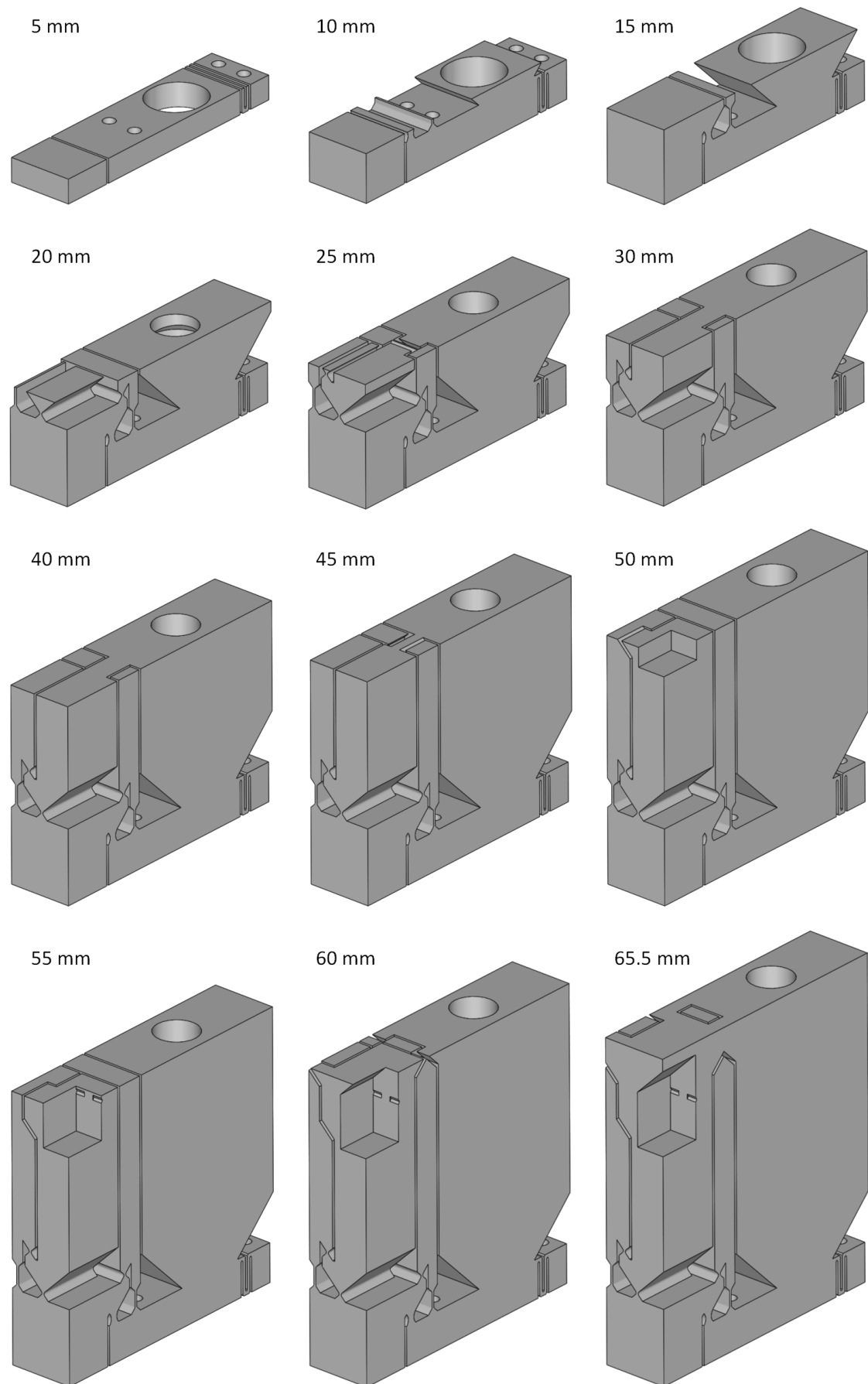


Figure 6.10: Printing process of the main block of the lever ratio concept rapid prototyping design. The part is printed from the interface with the collimator, so rotated with respect to Figure 6.9.

The chosen printing process is shown for each layer in Figure 6.10, showing all the 45 degree features described before. Note that the holes that are in line with the printing orientation are printed, while the holes that are orthogonal to the printing orientation are not. These holes are later drilled during the post-processing steps.

The design also has two support structures printed along with it. The first is located between the mounting interface of the collimator and the heat sink block. This support structure is milled away during the post-processing steps. The second support structure is below the tilt mechanism. This structure however does not limit the motion so does not need to be removed.

Despite being attractive for creating complicated structures, rapid prototyping is still limited by manufacturing tolerances. As also apparent from the design constraints provided by the manufacturer, the manufacturing tolerances are in the order of a tenth of a millimeter. This could lead to problems when making a high precision mechanism, especially concerning the flexures. Therefore, one of the research objectives in making the proposed prototype is evaluating the feasibility of designing high precision mechanisms using rapid prototyping.

Breadboard design

Note that the above design is missing a breadboard mounting feature. This is because the breadboard design is left outside the scope of the prototyping. Instead, the focus is on the mechanism itself. However, when using a similar design as presented for the double wedge concept, the mechanisms can easily be mounted to a breadboard. Note that the mounting feature at the bottom of the mechanism might be difficult to achieve, since it overlaps with the support structure mentioned earlier. This means that the support structure would need to be milled with 90 degree features, which is not possible. Instead, wire erosion could be used, or the design could be slightly altered to allow for milling.

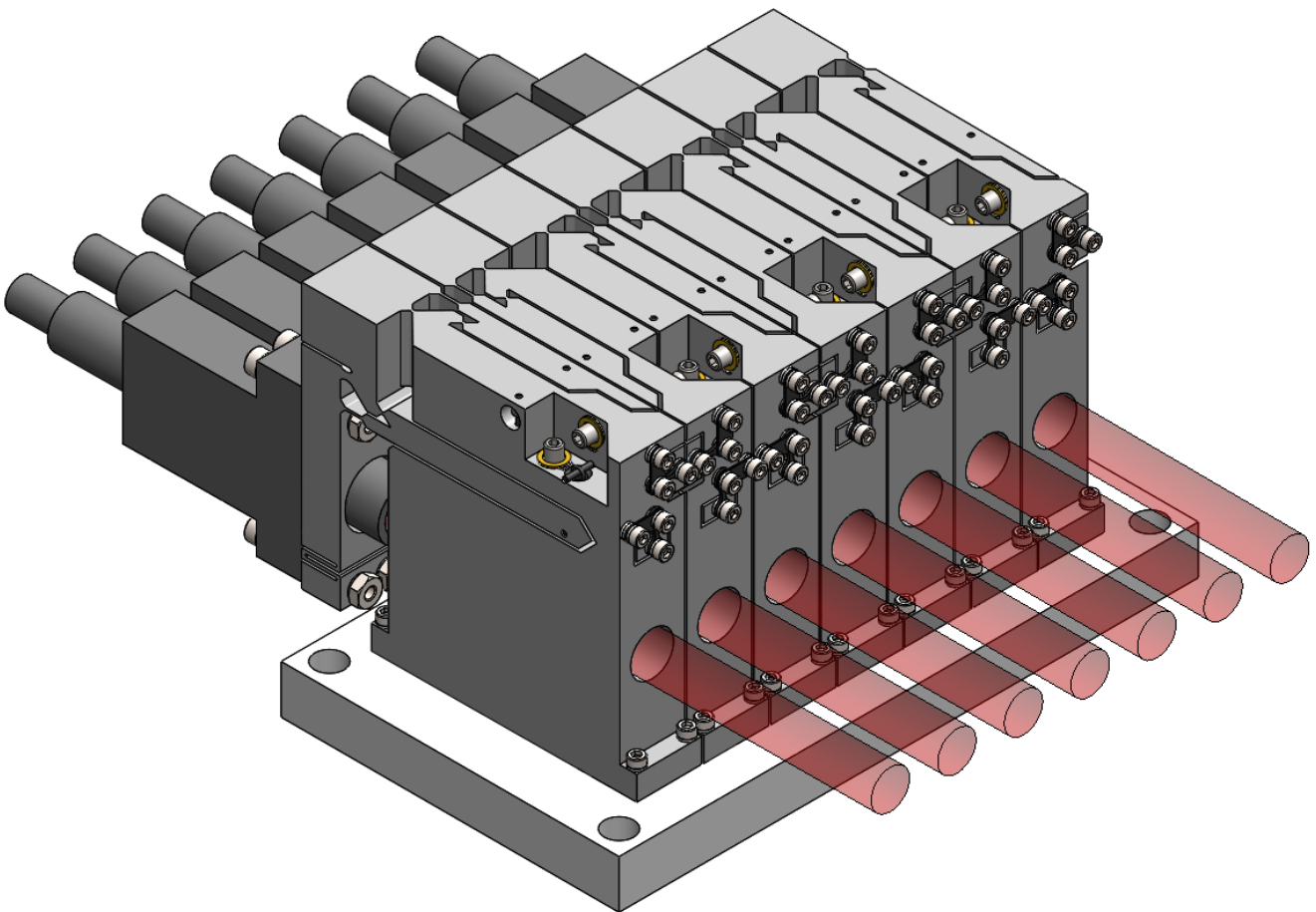


Figure 6.11: Breadboard assembly for the lever ratio concept.

6.3.3 Material selection

The pre-tension springs are made of spring steel, to allow for a stiff spring with small dimensions. The springs are held into place by small rods, which are cut from a 1 mm diameter steel rod. For these rods, a stainless steel alternative was also considered but the harder, regular steel was chosen because it is easier to cut and is less likely to bend due to the spring or assembling forces.

The locking plates and bolt rings are laser cut out of an aluminium 1060 plate. Using aluminium rings rather than off-the-shelf alternatives allows for a better thermal conductivity. The small dimensions are achieved with improved tolerances by placing an extra aluminium plate underneath during the laser cutting process. The retaining rings for the adjustment screw bushels are not available in the desired dimensions, because the cavity in which the screws are placed is very limited. These retaining rings are intended to be laser cut as well, but are left out of the prototype.

The screw tip is made of hardened steel, and a sapphire pad is placed underneath the screw to reduce the friction as well as prevent the Hertzian stresses from creating a pit in the lever arm. Such a pit would lock the screw into one position on the lever arm which can create problems during alignment.

The fasteners are again not made of aluminium, but rather steel. The difference in coefficient of thermal expansion can again be compensated for by applying a high enough pre-tension force on the bolts.

The main block and heat sink block of the spark erosion design are made of aluminium 6061-T6, because of its high failure stress levels and high thermal conductivity.

Aluminium AlSi10Mg

The chosen material for the rapid prototyping mechanism is also aluminium. Specifically, the alloy AlSi10Mg [28, 29] is chosen. As mentioned, the parts are printed per layer. This is done by depositing a layer of aluminium powder in the printing machine. The powder is then melted locally using a laser to create the desired structure. After the laser has melted the current layer as specified by the .step file, another layer of aluminium powder is deposited and the process is repeated for the next layer of the .step file.

This printing process means that there is a large uncertainty in the material properties of the resulting mechanism. In fact, the properties are expected to vary throughout the mechanism based on the local feature sizes and direction with respect to the printing direction [29]. Also, there will be small air cavities throughout the mechanism since the density is stated to be 99.8 %.

The Young's modulus is given to be 75 GPa, making the printed aluminium stiffer than similar non-printed aluminium alloys (the Young's modulus of aluminium 6061-T6 is 68.9 GPa [30]). This makes printed aluminium less favorable for flexures.

The yield strength is given to be 170 - 220 MPa, which is lower than the yield strength of 276 MPa given for aluminium 6061-T6. Off course, the yield strength varies greatly for different aluminium alloys. A high yield strength is however also favorable for flexures.

The ultimate tensile strength is given to be 310 - 325 MPa, which is actually very similar to that stated for aluminium 6061-T6 (310 MPa). Since the alignment is intended to be done only once, it might be worth considering loading the mechanism beyond its yield strength should this be required.

And finally the thermal conductivity is given to be 120 - 180 W/mK. This great variation is particularly challenging for the thermal stability of the mechanism. It is difficult to predict the exact thermal behaviour because the thermal conductivity can vary locally. Therefore a worst case estimate will be taken. On average, the thermal conductivity is somewhat similar to that of aluminium 6061-T6, which is stated to be 167 W/mK.

Note that porous materials are known to have increased damping, which could benefit the mechanical stability of the mechanism. This effect is studied in [31], for densities between 25 and 90 %. Therefore the density of 99.8 % is outside the scope of this study. However, the study does show a stabilizing of the damping effect towards the 90 % density.

Titanium Gr23

Another popular metal for rapid prototyping is titanium. Specifically the Gr23 alloy was considered for this design [32]. Even though the Young's modulus is slightly higher (110 GPa) than that of aluminium, the printed titanium does have a yield strength between 900 and 1200 MPa, and an ultimate tensile strength between 1100 and 1300 MPa. This makes it more suitable for designing flexures.

The thermal conductivity of printed titanium is stated to be 7 W/mK, which is over an order of magnitude lower than that of aluminium. This is however in part compensated by its coefficient of thermal expansion. This is 8.64 K^{-1} , which is lower than the coefficient for aluminium (23.4 K^{-1}) [33]. As a result, the thermal deformation for the same temperature gradient is only a factor 6 higher for titanium.

Furthermore, the lower conductivity means more heat is trapped in the collimator. As a result, there is a large temperature gradient with the surrounding air (for which the temperature is regulated within $\pm 1 \text{ }^\circ\text{C}$), meaning that heat loss through convection becomes more dominant. Therefore titanium was found to be a good alternative for aluminium.

However, the final choice for aluminium is based on the maximum allowed temperature of the collimator. The fact that the heat is trapped in the collimator means that the collimator temperature exceeds $35 \text{ }^\circ\text{C}$ for the current design. This could be mitigated by adding a copper heat sink which would be extra effective due to the large temperature gradient, but this would also add complexity to the design.

Chapter 7

Stability Analysis

7.1 Introduction

In this chapter, four stability concerns of the lever ratio concept are evaluated: thermal gradients, vibration stiffness, locking drift and screw play. Note that these stability concerns were tackled during the design process. Therefore the design presented in the previous chapter is the result of designing for these different stability concerns.

The chapter is concluded with a back-scatter analysis for the double wedge concept, since this is the main stability concern for that concept.

7.2 Thermal gradients

The greatest stability concern is due to thermal gradients in the system, caused by the local heat source in the collimator cylinder. This heat source is the result of the clipped power in the collimator, which is estimated to be at most 0.6 W (see Section 4.4 and the supporting document). The cumulative clipped power along the optical axis of the collimator is exponential, as shown in Figure 7.1. This is based on the local beam diameter of an expanding beam. As a result, most of the power is clipped in the last part of the collimator.

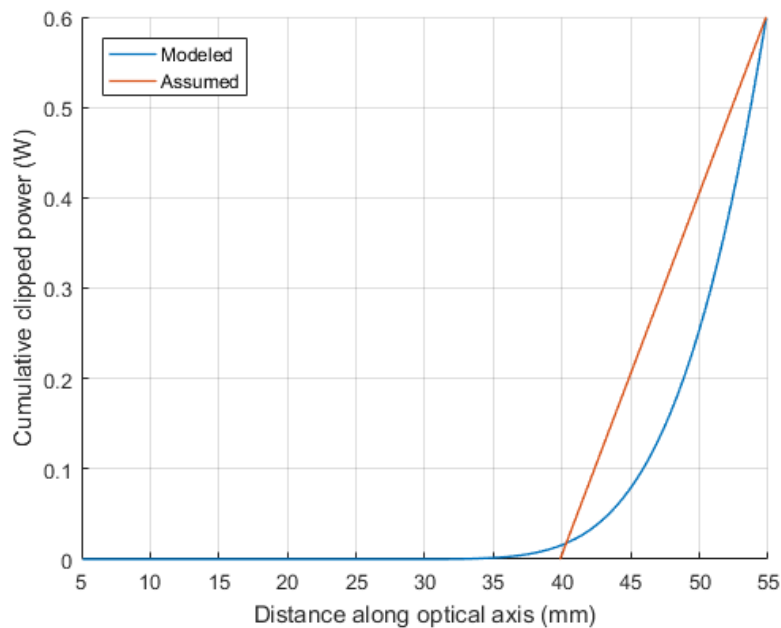


Figure 7.1: Cumulative clipped power distribution in the collimator, for both the modeled and the assumed case.

The collimator has a cylinder with a length of 15 mm at the end, which roughly coincides with the largest concentration of the clipped power. Therefore the clipped power is applied at this cylinder in the finite element model (FEM) simulations. This effectively means that a cumulative clipped power distribution is assumed as also shown in Figure 7.1. This assumption is made to simplify the model, and is justified by the fact that an expansion of the cylinder will only cause a negligible focus error. Therefore the simulation only needs to model the effect of sinking the heat through the collimator and mechanism.

Only conduction and convection are modeled. Radiation is left out because it is difficult to model and is assumed to have a negligible contribution due to the relatively small temperature gradients. Conduction is modeled assuming aluminium 1060 (with a thermal conductivity of 234 W/mK [34]) for the collimator, lock plates and bolt rings, and a uniform worst case thermal conductivity of printed aluminium (120 W/mK) for the printed mechanism.

The applied thermal boundary conditions are indicated in Figure 7.2. The bottom of the mechanism is set at 20 °C, because there the mechanism will be in contact with the breadboard (note that this same surface is also constrained in all directions). As mentioned, the 0.6 W heat source is applied on the collimator cylinder (equally distributed across the cylinder surface). Furthermore, a convection of 5 W/(m²K) is applied with a reference temperature of 21 °C at the blue surfaces. These surfaces are selected because they are intended to be exposed when placed in an assembly of 7 collimators. The temperature of 21 °C is chosen to model the likely scenario where the air surrounding the assembly will heat up due to the 7 heat sources.

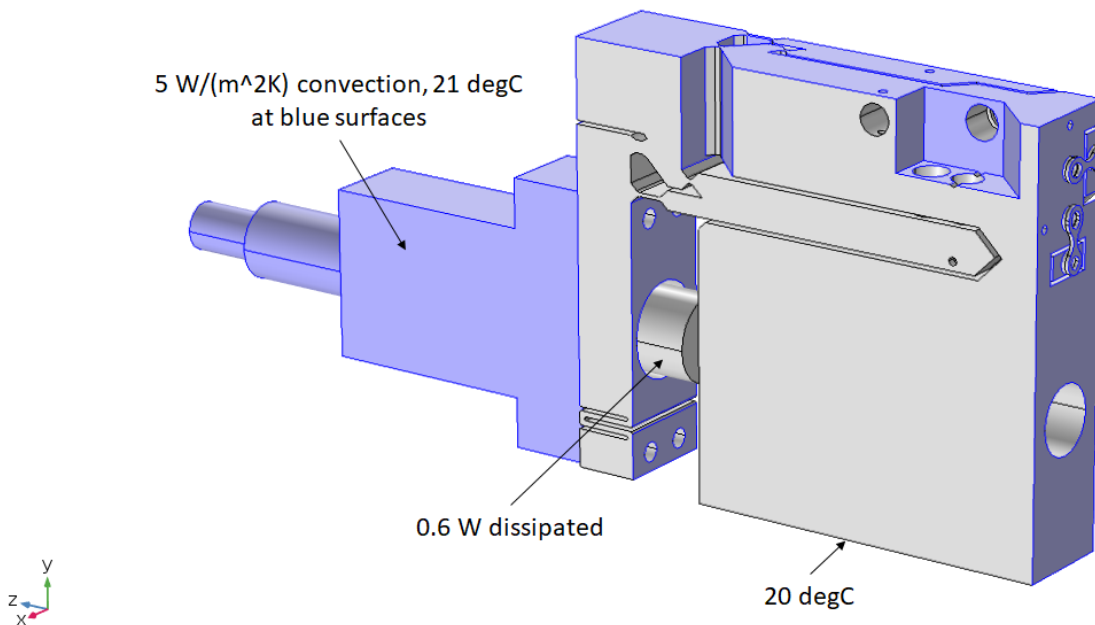


Figure 7.2: The applied thermal boundary conditions.

As mentioned, both convection and conduction are modeled. Convection causes exposed surfaces with high temperatures to reach a lower temperature instead. Conduction causes thermal gradients throughout the collimator and mechanism. These thermal gradients can be seen in Figure 7.3, where the temperature distribution is plotted in the steady state solution.

The gradients are caused by the thermal resistances on the thermal path from the heat source to the heat sink. The amount of power that can be conducted across a thermal resistance depends on the temperature gradient across that resistance. Therefore each part of the mechanism will reach a certain temperature in the steady state, that allows for all the power from the heat source to be dissipated in the heat sink.

Based on the temperature distribution, the thermal path can be reconstructed. The heat in the collimator cylinder first spreads into the rest of the collimator. Then the heat flows into the mechanism through its four

bolted connections. Even though the thermal resistance into the mechanism is equal for all four connection points, the flows more easily into the top two connection points. This is because the heat flowing into the bottom two connection points experiences a larger thermal resistance before reaching the top two connection points.

The heat flowing into the mechanism subsequently flows into the tip mechanism. The tip mechanism has a total of three flexures, each causing a thermal resistance. Part of the heat flows into the tilt mechanism, while part of the heat flows into the tip lever arm and is sunk through the locking plate. The heat that flows into the tilt mechanism also crosses three flexures, and thus three thermal resistances. Part of the heat flows into the main structure directly (which is dark blue in Figure 7.3), while another part flows into the tilt lever arm and is sunk into the main structure through the locking plate.

As a result of the described thermal path and the thermal gradients across this path, there are three main drift sources to be identified in this mechanism. The first drift source is the asymmetric heat sink from the collimator to the mechanism. As mentioned, the heat flows more easily to the top of the collimator than to the bottom. The resulting temperature gradient causes an approximate $0.5 \mu\text{rad}$ drift.

The second drift source is the temperature gradient between the collimator and the mechanism. This causes the collimator to expand more than the surface which it is attached to. The result is that the collimator will bend around the mechanism surface. This effect is however reduced to almost zero by introducing the extra flexure shown. This allows the collimator to expand downwards, and keeps it from bending.

The third drift source is the temperature gradient in the flexures of the tip and tilt mechanisms. The bottom (thin) flexure heats up more than the top (thick) flexure. This causes a moment around the arm between those flexures, because the bottom flexures expands more. This effect has been reduced by increasing the thermal resistance of the bottom flexure, while decreasing this resistance in the top flexure. The result is that more heat flows through the top flexure, thus increasing its temperature and achieving a more similar temperature gradient in both flexures. Thus the collimator moves to the left when the flexures expand, and the tip/tilt drift is kept to a minimum.

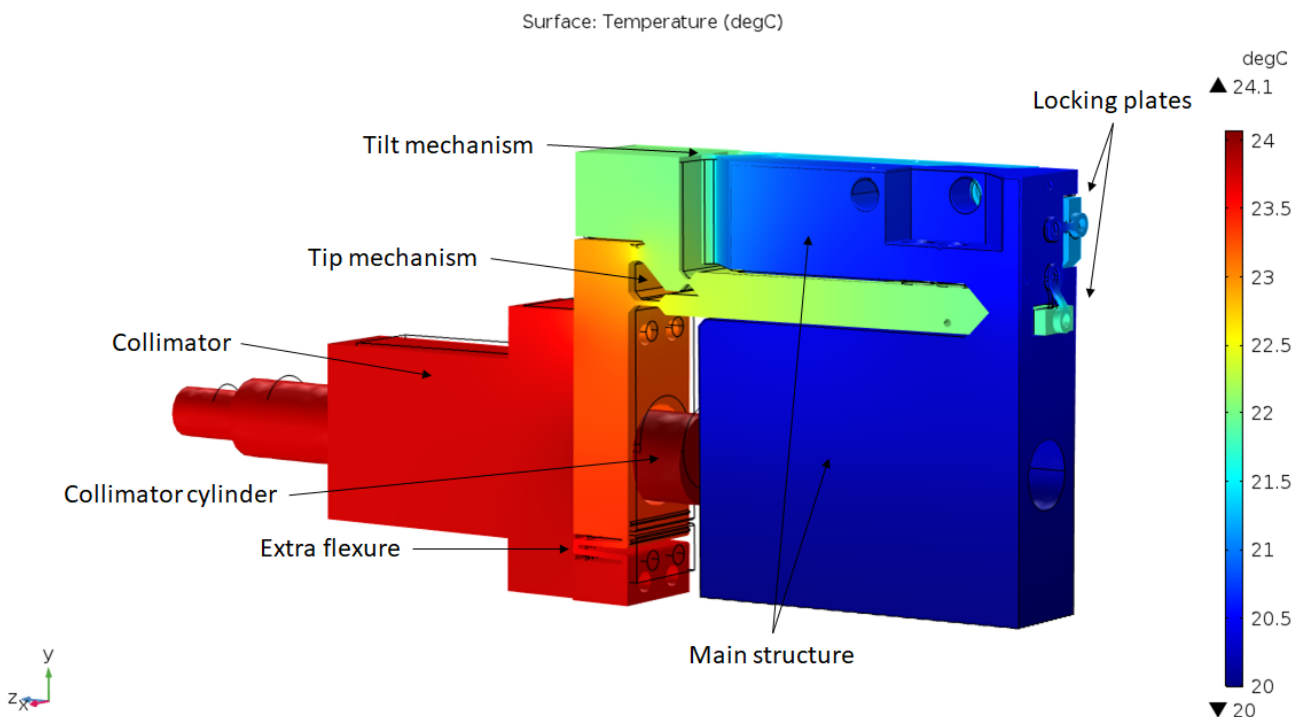


Figure 7.3: Temperature distribution in steady state, and deformations shown with a scale factor of 889.

In total, the thermal drift for tip is calculated to be $10 \mu\text{rad}$, while the drift in tilt is $5 \mu\text{rad}$. This difference can be explained by the fact that the heat first flows through the tip mechanism, and afterwards through the tilt mechanism. Therefore, the temperature of the tip mechanism is higher than that of the

tilt mechanism. The temperature gradient is also smaller for the tilt mechanism because part of the heat is already sunked through the lever arms and locking plates, meaning less heat flows through the tilt mechanism. Furthermore, the block between the tip and tilt mechanisms has a uniform temperature whereas the block between the collimator and the tip mechanism has a gradient.

Note that for tip, the total stability budget of $\pm 5 \mu\text{rad}$ is used for thermal stability. In fact, the mechanism needs to be misaligned by $5 \mu\text{rad}$ in order to ensure it remains within the budget. However, the presented analysis is intended to be a worst case scenario. In reality, the clipped power will be less than 0.6 W for most of the cases, and the thermal conductivity will be better than $120 \text{ W}/(\text{mK})$ for most of the printed mechanism.

Nevertheless, there is no longer room for other error sources in the stability budget. However, the design is intended to have no long term error sources. The effect of creep on the tip and tilt mechanisms should be negligible because the design is geometrically defined (as mentioned in Section 5.4). Furthermore, the effect of creep on the locking plates should also be negligible because the stress levels are low. Therefore only short term error sources are expected, which thus should be compensated for during the alignment process.

7.3 Vibration stiffness

The mechanism can be mechanically loaded by two main sources: the alignment operator and ground vibrations. The alignment operator could touch or even hit either the mechanism or the table accidentally. Furthermore, the operator will put forces (torque, tension and compression) on the adjustment and locking screws during the alignment. Any vibrations caused by these events should dampen out quickly, such that the alignment can be accurately measured. These events should also not cause the mechanism to snap into a different position.

The ground vibrations should also not cause the mechanism to vibrate significantly nor snap into a different position. However, these ground vibrations are controlled in the bulk multiplexer subsystem to either the VC-E or VC-F spectrum [13]. For VC-E this means that the vibration levels are allowed to be at most $3 \mu\text{m}/\text{s}$, which is considered sufficient for very sensitive laser systems [35].

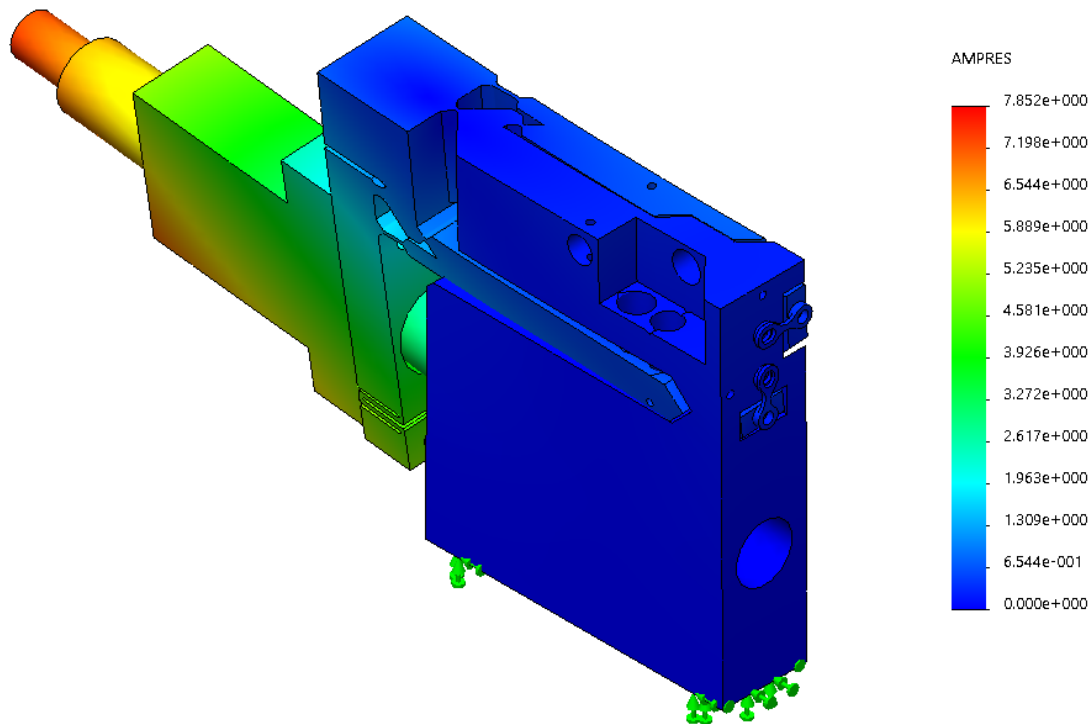


Figure 7.4: First eigenmode at 411 Hz. The mechanism is only constrained on the bottom surface, indicated by the green arrows.

Note that the actual dynamic stability is also determined by the damping in the mechanism. The damping is however difficult to predict, so only the eigenfrequencies of the mechanism are considered for now. Since the vibrations mentioned are assumed to be low-frequency, increasing the eigenfrequencies means that less dynamics can be excited. The eigenfrequencies can be increased by increasing the stiffness of the mechanism and decreasing the vibrating mass.

The first eigenmode of the mechanism is shown in Figure 7.4, where the mechanism is only constrained on the bottom surface (indicated with the green arrows). The deformation shows a rotation around the optical axis due to a torsional mode in the thick flexures, as well as the locking plates. The Eigen-frequency is 411 Hz and the VC-E vibrations for this frequency have an amplitude of 7 nm. These vibrations are assumed to be small enough to be dampened out by the bolted connections within the mechanism.

The second eigenmode of the mechanism shows a tip of the collimator, caused by a bending mode in the tip lever arm, as well as in the flexures and locking plates. The eigenfrequency for this mode is 470 Hz.

The third eigenmode of the mechanism again shows a rotation, due to a second order torsional mode at an eigenfrequency of 1249 Hz.

7.4 Locking drift

The stability concern for locking drift is actually two-fold. First of all, the torsion applied on the locking plates will cause the alignment to drift slightly during locking. This is in part mitigated by placing a moment-release plate on top of the locking plate, which prevents the torque from deforming the locking plate. However, the drift is still in the order of $0.3 \mu\text{m}$, as mentioned in Section 5.6.1.

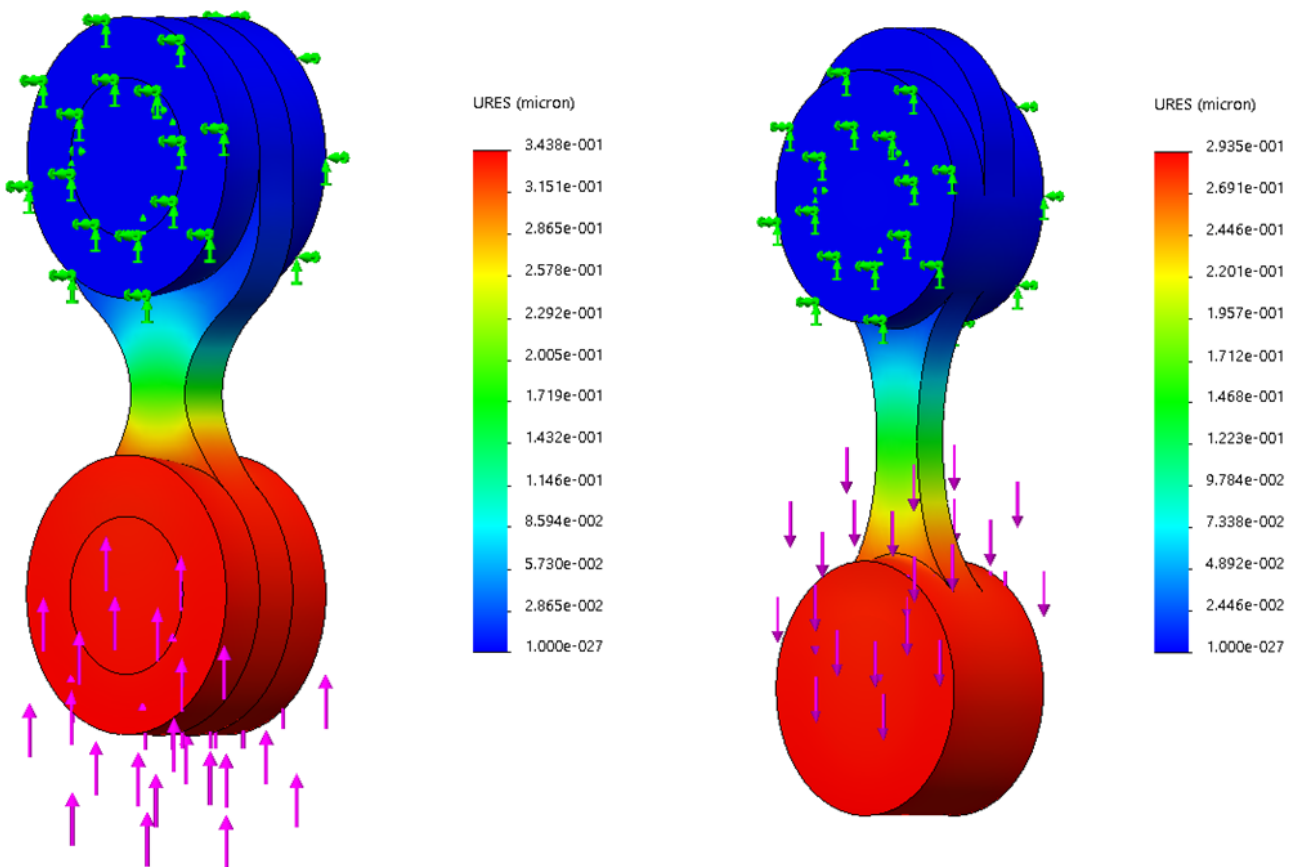


Figure 7.5: Elastic play in locking plates due to expected force for releasing adjustment screws after locking at the end of the range. The plate has a maximum compression load in the left figure, and a maximum tension load in the right figure. The blue rings are constrained, while the red rings are loaded.

The second source of drift is due to the elastic play in the locking plates. During alignment, the flexures in the mechanism are elastically deformed by the force exerted by the adjustment screw. After locking, this adjustment screw might need to be taken out in order to release the degree of freedom that is locked by the locking plate (thus preventing the mechanism from being over-constrained). However, when this screw is taken out, the force of this screw will instead be exerted by the locking plate.

As shown in Figure 7.5, these plates have a limited stiffness. This is because the plates should only restrain one degree of freedom, and should therefore act as rods. The plates are shown in the deformed state, caused by the expected force for when the mechanism is aligned at the end of its range. The deformations are tuned to also be in the order of $0.3\ \mu\text{m}$ (and not more), while also sufficiently releasing the other five degrees of freedom.

This elastic play can be compensated for by aligning the mechanism, then taking out the adjustment screws, then measuring the drift, then aligning to minus that drift and taking out the adjustment screws again.

7.5 Screw play

As mentioned in Section 5.2 and Section 6.3, the chosen adjustment screw has a $50\ \mu\text{m}$ pitch and exceeds the thread class 6g-6H by 45%. The screw play has three main components: the intended allowance for allowing motion within the screw, the tolerance on the internal thread, and the tolerance on the external thread. These tolerances are assumed to be independent, and therefore added quadratically. The allowance is added linearly because it is the nominal value, rather than a tolerance.

The screw play is estimated based on the data provided by the supplier ($50\ \mu\text{m}$ pitch, and exceeding thread class 6g-6H by 45%). This estimation yields an allowance of $15\ \mu\text{m}$, an internal thread tolerance of $20\ \mu\text{m}$ and an external thread tolerance of $19\ \mu\text{m}$. Adding these as described above yields a total screw play of $43\ \mu\text{m}$.

The screw play is shown in Figure 7.6, showing the screw inside its bushel and the screw pushing against a lever arm. As shown, the screw play means that the screw can rotate inside its bushel. Since the effective length of the screw is its nominal length multiplied with the cosine of its rotation, this rotation causes an uncertainty in the adjustment made by the screw. Note that this effect is also true for straight surfaces.

The second effect shown in Figure 7.6 is however unique for tilted surfaces. The lever arm is rotated because the screw actuates the lever arm. The maximum rotation is determined by the range of the mechanism and the lever ratio applied. Here, the range is set at 0.12° and the lever ratio at 2. Therefore the maximum rotation of the lever arm is 0.24° . This rotation of the lever arm means that the rotation of the screw inside its bushel yields an uncertainty in the position of the lever arm.

Both these effects are plotted in Figure 7.7 for the entire screw play range of $\pm 43\ \mu\text{m}$. When adding these effects, the new sensitivity of the screw can be determined by taking the maximum and minimum longitudinal play. This sensitivity is $0.65\ \mu\text{m}$, which corresponds to 5° Allen key adjustments of the screw. Note that in order to reach the required $10\ \mu\text{rad}$ resolution, an arm length of $32.5\ \text{mm}$ is required (which is the designed arm length in the detailed design).

However, the issue is in part solved by the fact that the screw pushes against a sapphire pad in the final design. This means that the friction coefficient is low, which limits the number of expected angles for the screw within its bushel. Furthermore, the screw is placed under pre-tension by pushing against a lever arm that is attached to a pre-tension spring. This forces the screw into a certain position within its bushel.

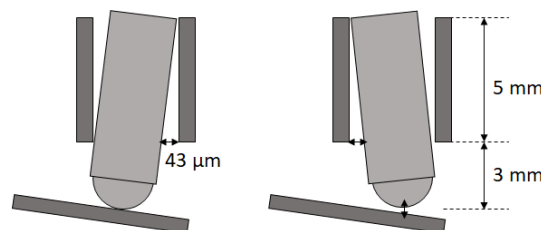


Figure 7.6: Visualisation of the uncertainty in screw position due to play in its thread.

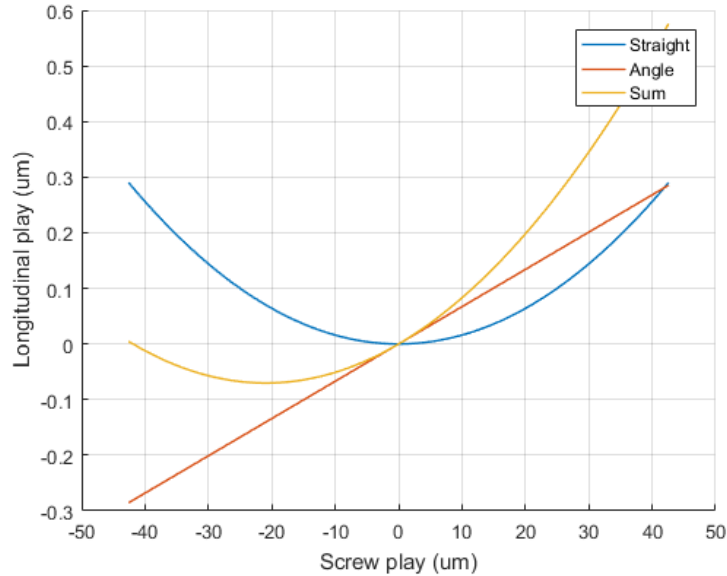


Figure 7.7: Longitudinal play due to two factors and its sum, across the screw play range.

7.6 Back-scatter analysis

The above-mentioned stability concerns can be reduced to negligible for the double wedge concept. For this concept, however there is a different, optical stability concern. The laser light transmitted by the collimator is not allowed to enter back into the fiber. This would destabilize the laser because this back-scattered light is out of phase with the laser source.

Fortunately, coupling laser light into the fiber is difficult, because the aperture of the fiber is very small and the coupling efficiency is sensitive to focus shifts. Furthermore, the reflection coefficients of the wedges can be kept low by using proper anti-reflection coatings. As a result of these effects, the back-scattered light coupled into the fiber is approximately 0.02 W (or -34 dB, compared to 50 W) if the light is reflected along the optical axis.

However, the light is not reflected along the optical axis, because the wedges are oriented such that the light never travels orthogonal to the reflecting surfaces. Instead, the light is reflected under an angle, as shown in Figure 7.8 using an online ray optics simulation (<https://ricktu288.github.io/ray-optics/simulator/>).

The first surface reflects the light under an angle that is double the apex angle of the wedges. This means a back-scatter angle of 0.266° for the smallest possible apex angle.

The second surface reflects the light under an angle that is equal to the maximum range of the double wedges. This is because the light effectively travels twice through the single wedge, giving the same effect as traveling once through two wedges. This means a back-scatter angle of 0.118° for the smallest possible maximum range.

The third surface reflects light under the same angle as the second, because it is parallel to the second surface.

The fourth surface reflects light under an angle that depends on the rotation of the second wedge with respect to the first wedge. If the second wedge is rotated such that it doubles the effect of the first wedge, the back-scatter angle is the summation of the double apex angle and the maximum range angle, thus 0.384° . If the second wedge is rotated such that it cancels the effect of the first wedge, the back-scatter angle instead is the difference of the double apex angle and the maximum range angle, thus 0.148° .

Therefore the smallest expected back-scatter angle is 0.118° . Calculating the back-scattered power yields the result presented in Figure 7.9, which is equal to -241 dB. This is further exemplified in Figure 7.10, where the image is zoomed to show that the back-scattered light misses the fiber aperture.

However, note that the wedges might also be mis-aligned in tip or tilt because the beam steering is

insensitive to these mis-alignments in first order. Therefore, assuming a severe mis-alignment, the back-scattered power is also calculated for a back-scatter angle of 0.05° , which is found to be -71 dB.

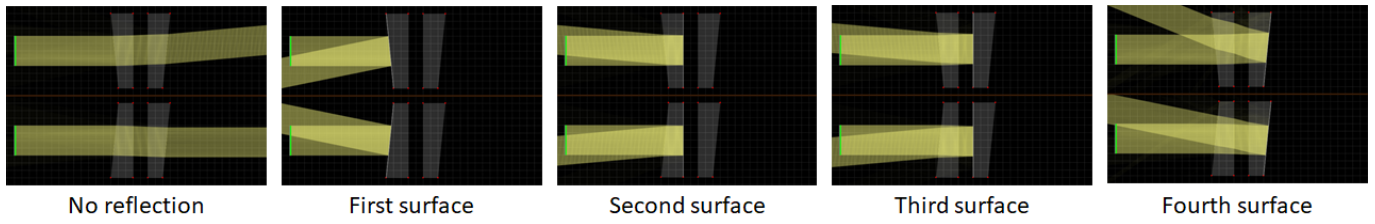


Figure 7.8: Ray optics simulation for all four back-scattering surfaces.

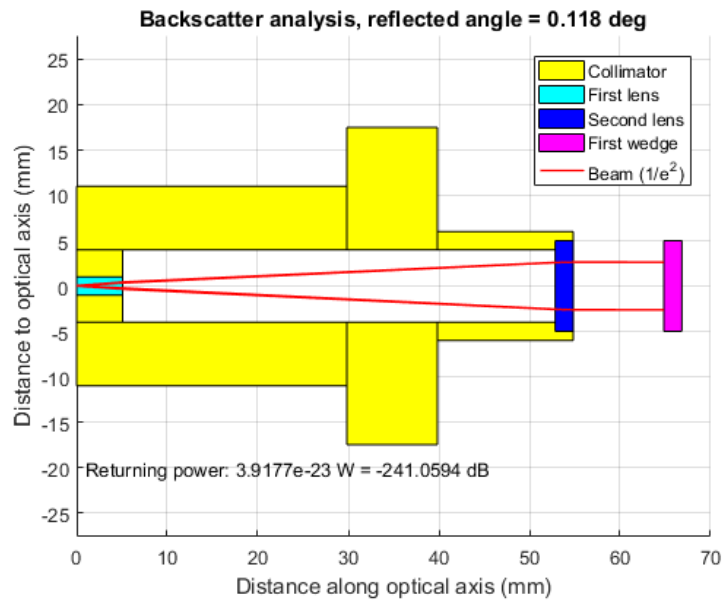


Figure 7.9: Gaussian optics simulation of the collimator with a back-scatter angle of 0.118° .

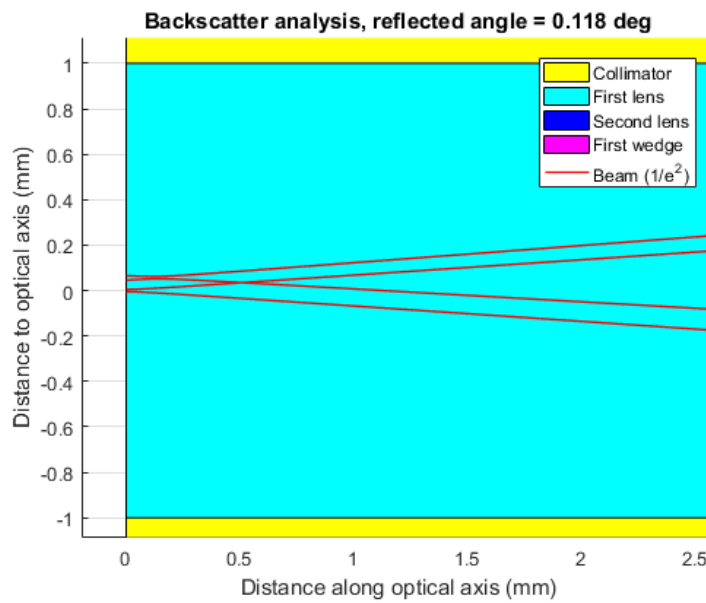


Figure 7.10: Gaussian optics simulation of the collimator with a back-scatter angle of 0.118° , zoomed in to show the waist misses the fiber.

Part III
Validation

Chapter 8

Prototype

8.1 Introduction

In this chapter the obtained prototype is discussed. The printed parts and the adjustment screws are presented separately, since they form the main parts of the prototype. The chapter is concluded with an overview of how the mechanism is assembled.

8.2 Printed parts

As mentioned, one of the research objectives for manufacturing the proposed prototype is evaluating the feasibility of designing high precision mechanisms using rapid prototyping. The anticipated tolerances are in the order of a tenth of a micrometer. Therefore the printed parts are inspected in detail.

A total of five mechanisms were printed: three regular and two mirrored versions. One of the regular versions is shown in Figure 8.1 through Figure 8.3. Unfortunately, due to a communication error with the supplier, an old version used for obtaining a quotation was printed instead of the final design. Since there was no time/budget available for ordering new parts, the validation is done for these old parts. As a result, there are three main differences between the intended and obtained parts.

First of all, the extra flexure is missing, which was added to prevent the bending of the collimator due to the temperature gradient between the collimator and the mechanism. Therefore, the thermal stability is expected to be significantly worse than anticipated.

Secondly, the positions for the spring axes holes are outdated. These were fine-tuned in the final design to allow for a 0.1 mm tolerance on their position. These tolerances could only be met by using a stiffer spring. Therefore the spring holes as obtained in the printed parts are designed for a less stiff spring without taking tolerances into account.

The third difference is in the tilt flexure: instead of a thick flexure the final design has a thin flexure (0.5 mm thick). This was changed to allow for a greater range of motion in the tilt direction, because the thick flexure was not required for the thermal stability in the tilt direction. Therefore, the range in tilt is expected to be less than anticipated.

There are however also two main issues with the printed parts regardless of which version is printed. First of all, as can be seen in the pictures, the long flexures are not straight. This angle is however consistent for the naked eye for every mechanism. Also, there are no anticipated issues due to this angle. In fact, this angle was actually anticipated since the advised minimal wall thickness provided by the manufacturer is 0.7 mm (see Table 6.1), while these flexures are designed for 0.5 mm thickness.

The second issue is much more severe, and is found in all the printed flexures: the flexures are much thicker than designed. The thin flexures are 0.8 mm thick (with a variation of ± 0.01 mm) instead of 0.5 mm. The thick flexures are 1.6 mm thick (also with a variation of ± 0.01 mm), instead of 1.5 mm. This difference was not anticipated, because the specified embossed details minimal size is 0.5 mm. The result of the extra thickness is that the mechanism is much stiffer than designed for. Therefore it is anticipated that the pre-tension springs are not stiff enough, which limits the range of the mechanism.

The perpendicularity between the interface to the breadboard and the interface to the collimator is checked using a machinist square. Since there is no visible deviation between the printed block and the machinist square, the achieved tolerance is assumed to be within the set $\pm 0.033^\circ$ (see Table 4.2).

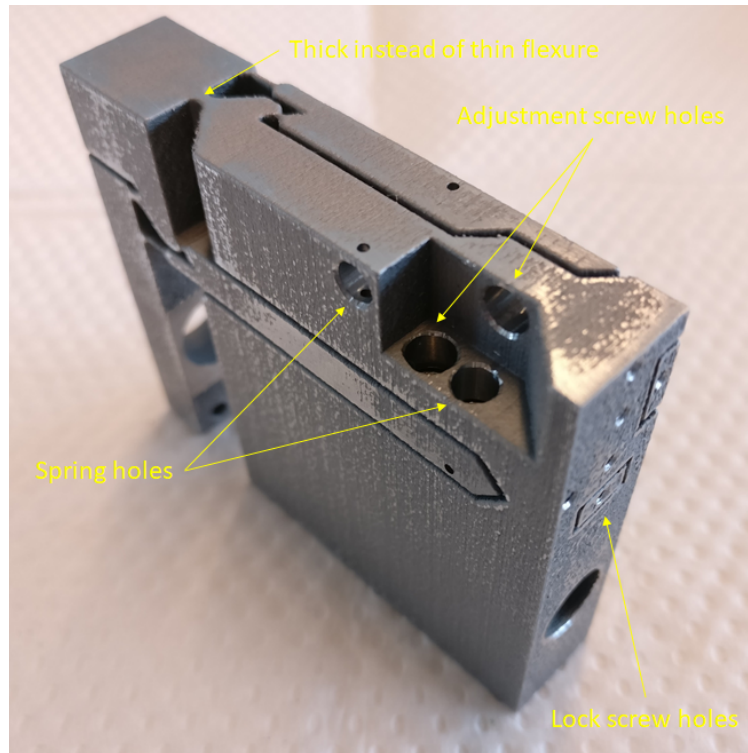


Figure 8.1: Printed block, including post-processing steps.

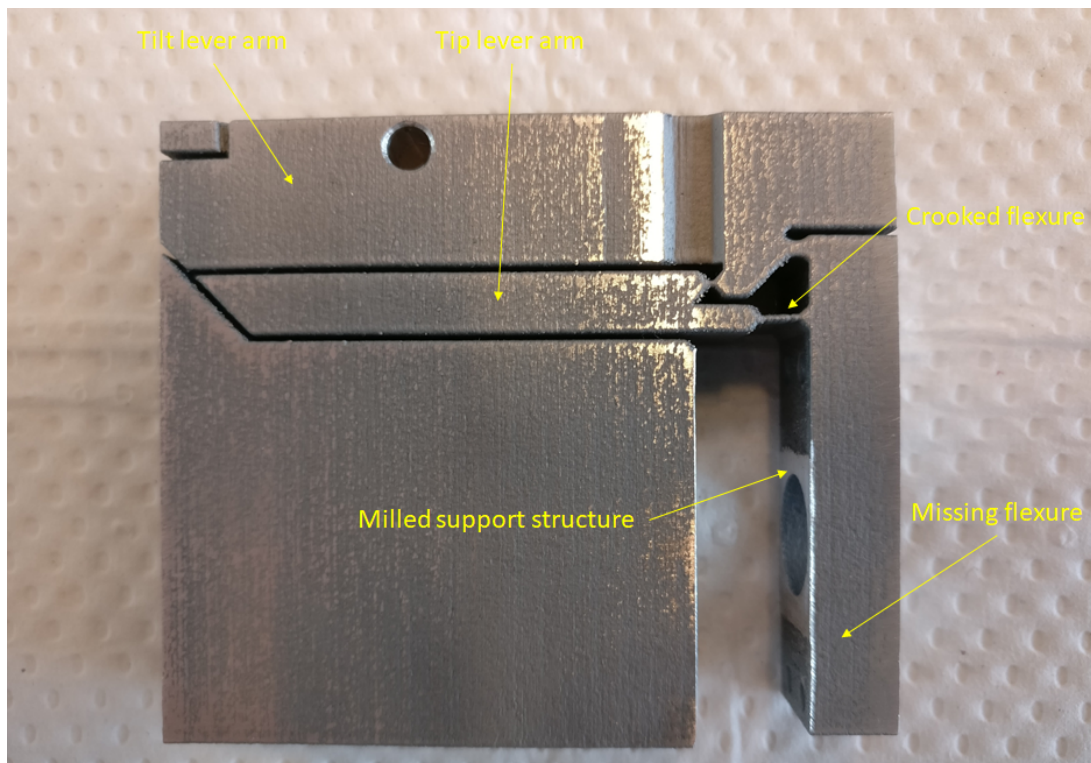


Figure 8.2: Printed block, including post-processing steps. The crooked flexure of the tip mechanism is indicated, as well as the milled support structure.

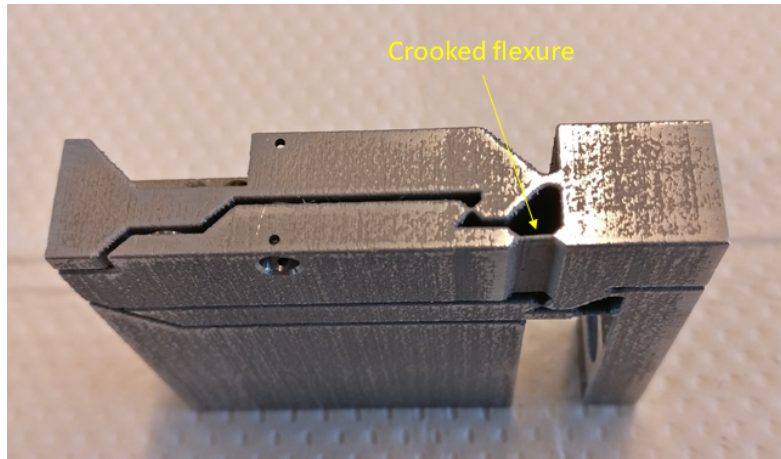


Figure 8.3: Printed block, including post-processing steps. The crooked flexure of the tilt mechanism is indicated.

8.3 Adjustment screws

The 50 μm pitch adjustment screw is shown in Figure 8.4 along with the 1.5 mm Allen key used for actuating the screw. The screw can be used for its entire range and can even be flipped with respect to its bushel without any noticeable increase in friction. The friction between the screw and its bushel is low enough to allow for small rotation steps in the order of 1° .

There is an issue with the mounting of the bushel however. The hole in the printed part is designed to be a tight fit for the bushel. In practice, the bushel fits either too loosely or too tightly in this hole. This means that in some cases the bushel will be pressed out of the hole when actuating the adjustment screw, and in other cases the bushel is compressed so tightly that the adjustment screw no longer fits into the bushel.

The first scenario has been mitigated by applying Loctite around the bushel. The Loctite spreads between the bushel and its hole, after which it hardens due to a lack of air. The second scenario could not be mitigated. Therefore it is recommended to use a clearance fit instead, and use glue for every bushel.



Figure 8.4: 50 μm pitch adjustment screw with a 1.5 mm Allen key.

8.4 Mechanism assembly

The assembling process of the mechanism is started with the lock plates (see Figure 8.5). This restricts the degrees of freedom of the mechanism and locks it into its nominal position. Therefore there is a reduced risk of failure due to overloading the flexures. Furthermore, assuming that the mechanism is indeed locked into its nominal position, this can be used to find this position during the test.

The locking plates, moment release plates, bolt rings and bolts are too small to position properly by hand. Therefore a pincet is used to position the plates and rings and an Allen key is used to position the bolts, after which the bolts are immediately locked.

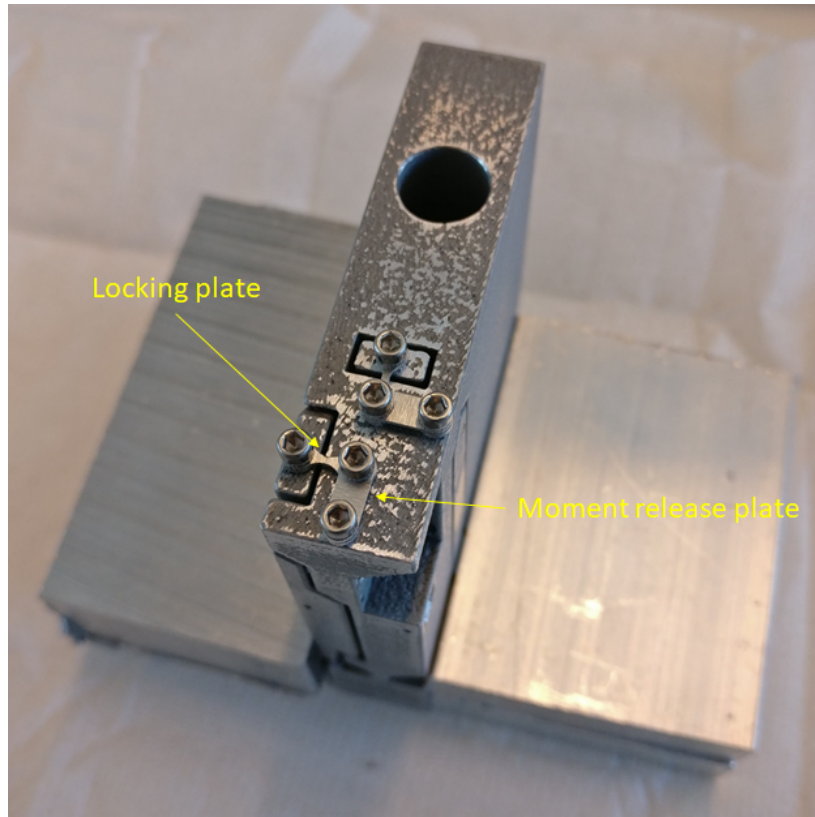


Figure 8.5: Assembling of the locking plates, using a pincet and an Allen key.

The next step is to mount the pre-tension springs, which is particularly challenging using standard equipment. First, the spring is positioned into its hole and locked into place using the first spring rod (which is positioned through the first ring of the spring). Then, the second spring rod needs to be positioned through the second ring of the spring. This however needs to be done while the spring is under tension.

The spring is put under tension by placing a pincet in the second ring and using the pincet as a lever to lift up the spring (as shown in Figure 8.6). The second spring rod can then be placed through the second ring after which the pincet can be released. The challenging part is that the ring is not large enough for both the pincet and the spring rod to fit through. Therefore it is recommended to either use a spring with a larger ring, use smaller spring rods, or use a smaller pincet.

Note that the process is slightly easier when the spring rods are cut to size after assembly. This is especially the case for the tip spring, as shown in Figure 8.7. The long spring rod can be used as the lever instead of the pincet. As such mounting this spring is relatively straight forward and requires no re-design. However, the spring rods need to be grinded after assembly for the final design because it is not possible to cut the rods to the proper size using this method.

The last parts to be assembled are the adjustment screws, see Figure 8.8. As mentioned, due to an issue with the tolerance fit, the bushels need to be glued into the mechanism using Loctite. If the hole for the bushel is too small, the screw will no longer fit into the bushel. Therefore it is recommended to pre-assemble the screw and bushel, since actuating the screw can be used to de-assemble the bushel while the bushel itself can not be taken out of the mechanism.

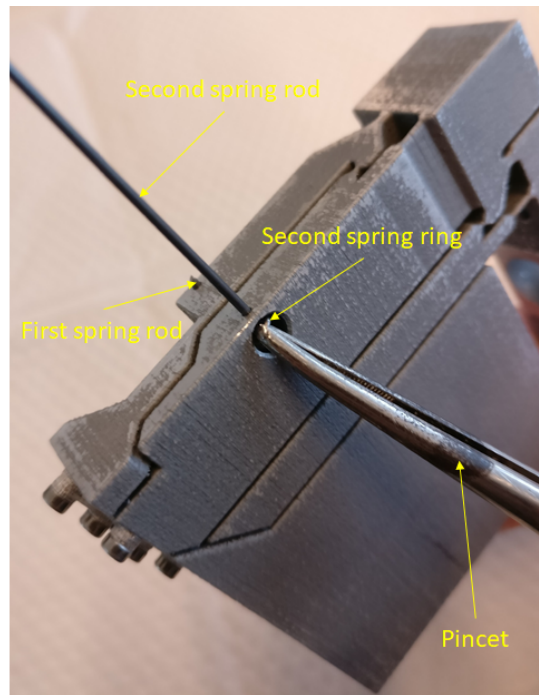


Figure 8.6: Mounting the tilt spring.

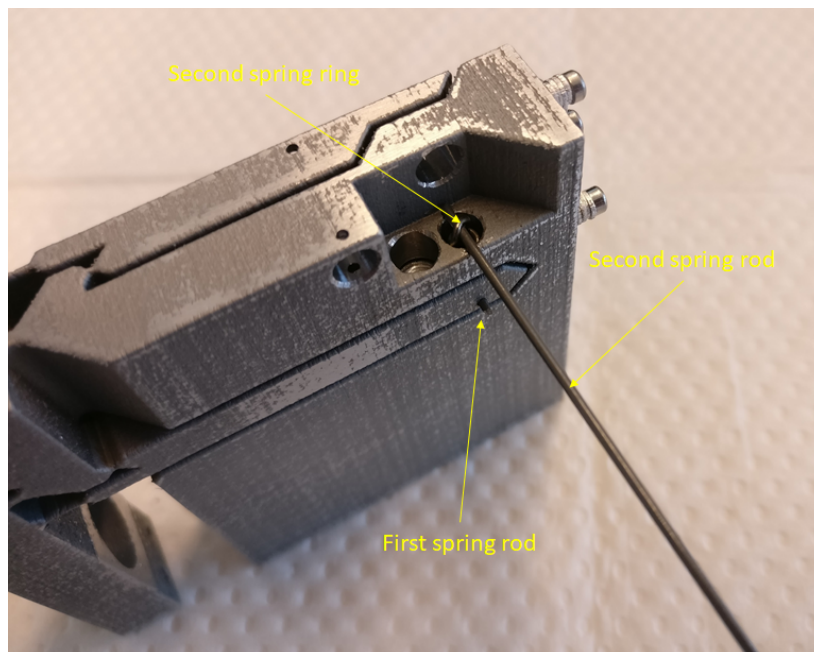


Figure 8.7: Mounting the tip spring.

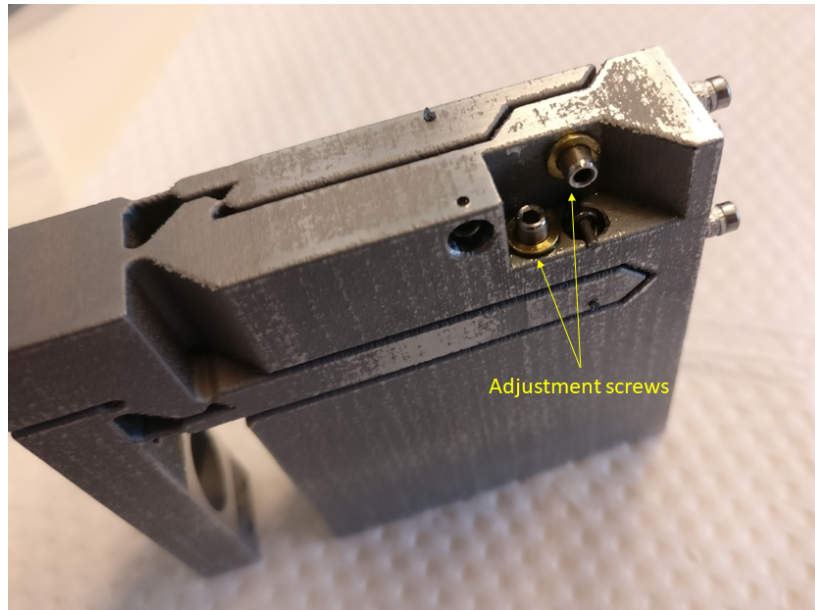


Figure 8.8: Mounting the adjustment screws.

Chapter 9

Test setup

9.1 Introduction

In this chapter, the different elements of the test setup are presented. This test setup is designed to answer the following research questions:

- What is the smallest setting resolution that can be achieved?
- What is the maximum range of the mechanism?
- Is the resolution consistent across the range?
- How much cross-coupling can be seen between tip and tilt?
- How much does the alignment drift during locking?
- How much does the alignment drift when applying a 0.6 W heat source?

The expected smallest setting resolution is 1 μrad , based on the 0.5° rotation step size (see Section 4.2.3). However, as mentioned in Section 7.5, the screw play is expected to cause an uncontrolled 10 μrad snapping behaviour, thus limiting the resolution.

As mentioned in the previous chapter, the range of the mechanism is expected to be lower than designed for due to issues with the printed parts. The increased stiffness of the mechanism means that the mechanism can not reach its full range when the adjustment screw is actuated away from the lever arm (since the lever arm has an insufficient pre-tension). Furthermore, the increased stiffness also means that the flexures are expected to yield or even break before reaching the full range of the mechanism.

The resolution is expected to be consistent across the range, because the angles are very small (less than 0.12° for the adjusted frame, and less than 0.24° for the lever arm). Furthermore, the lever arms are designed to be stiff enough to prevent significant bending under the expected loads.

The cross-coupling into tip when actuating tilt is expected to be 4%, and the cross-coupling into tilt when actuating tip is expected to be 2%, based on FEM simulations. This cross-coupling is due to the fact that the adjustment screws actuate the lever arms off-center. Combined with a limited stiffness in the flexures this results in the cross-talk.

The locking drift is expected to be 3 μrad , based on the 0.3 μm sensitivity mentioned in Section 5.6.1. It is however possible that the example found in literature is not fully representative, because in the prototype made for this thesis the tip lever arm is connected to the adjusted frame of the tilt mechanism. The effect of this on the locking can be minimized by first locking the tilt mechanism, such that the tip locking plate can not cause the tilt alignment to drift. Furthermore, the dimensions of the locking plates differ from the example found in literature.

As discussed in the previous chapter, the thermal drift is expected to be worse than the 10 μrad anticipated in Section 7.2 because the extra flexure is missing in the printed parts. This means that the collimator will bend due to the the thermal gradient between the collimator and the mechanism.

9.2 Collimator dummy

Since the actual collimators are not yet available for testing, instead a dummy is milled out of aluminium. This dummy is shown in Figure 9.1, and is intended to simulate the thermal mass of the actual collimator (which will be made out of aluminium as well). Furthermore, the dummy can be used to attach the mirror under test to such that the alignment of the collimator can be measured rather than the mechanism itself.

The mirror under test was intended to be attached to the collimator cylinder to simulate the position of the collimator lens. However, the mirror is too small to return enough light to the auto-collimator. Therefore instead a larger mirror is attached to the back of the collimator dummy.

Note that it is difficult to mount the collimator (dummy) to the mechanism, because it is difficult to resist the rotation of the nut. This is done using a pincet, but this can only resist a limited amount of torque. As such, the pre-tension between the collimator and the mechanism is limited.

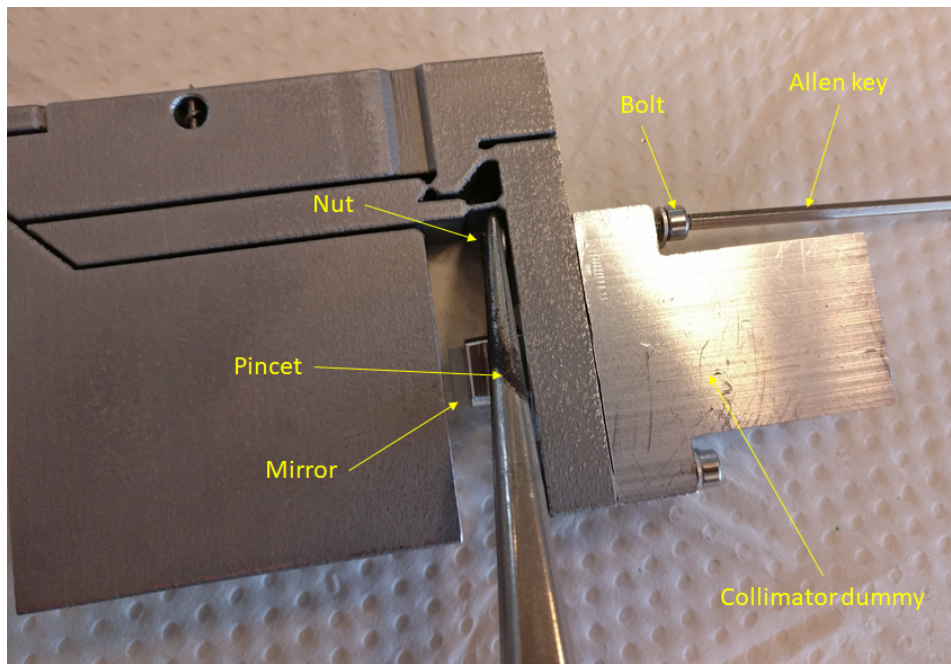


Figure 9.1: Mounting the collimator dummy to the mechanism.

9.3 Auto-collimator

The alignment measurement is done using an auto-collimator. The lay-out is shown schematically in Figure 9.2. A LED shines light through a reticle, after which the light passes through a beam splitter towards the collimator objective. The distance between the LED and the objective is equal to the focal distance, such that the outgoing beam is collimated.

The outgoing beam is then reflected upon a mirror under test, and returns under an angle to the auto-collimator. This angle is twice the tip/tilt of the mirror with respect to the optical axis of the objective. The returning light then passes through the same beam splitter and is projected unto a light-sensitive receiver. Because the distance between the objective and the sensor is equal to the focal distance, the reticle is in focus on the sensor. This reticle can then be used to accurately reconstruct the location at the sensor, from which the tip/tilt of the returning light can be determined.

The specific auto-collimator used is the ELCOMA VARIO 500/D65 auto-collimator, meaning that the focal distance is 500 mm and the lens diameter 65 mm. These parameters determine the range and accuracy of the system. The range for tilt is given to be 0.5° , while the range for tip is 0.4° . The accuracy is given to be ± 0.5 arcseconds (which is equal to $2.4 \mu\text{rad}$), but this accuracy is only guaranteed for a range of 0.3° .

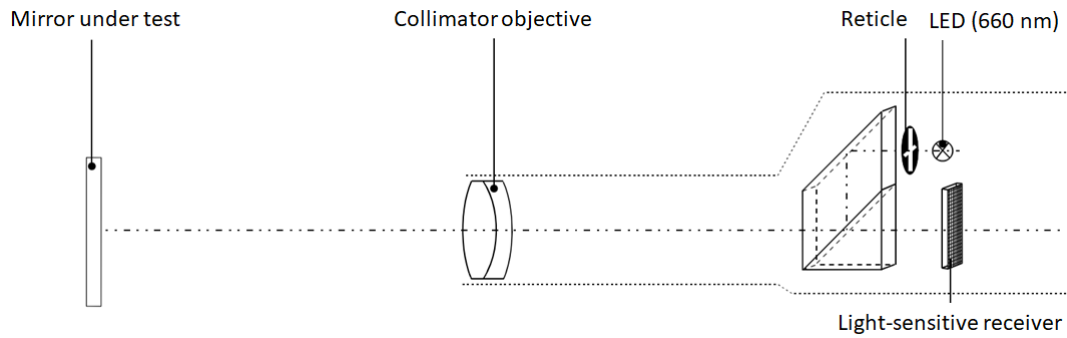


Figure 9.2: Lay-out of the ELCOMAT VARIO auto-collimator and its parts.

Note that this accuracy is in the same order of magnitude as the intended measurements. However, it is possible to obtain better measurement results by averaging over multiple data points and using the system for relative measurements rather than absolute.

Also note that the values stated here refer to the total range (thus corresponding to $\pm 0.15^\circ$). This is marginally enough to cover the intended range of the mechanism (which is $\pm 0.12^\circ$). Therefore the auto-collimator needs to be aligned to the center of the range of the mechanism. To achieve this, the auto-collimator is placed on a stage that can be actuated in tip and tilt using micrometer screws.

A picture of the auto-collimator system is shown in Figure 9.3, along with a mirror used for system validation. It is verified that the auto-collimator system is calibrated with a factor 2 off-set. This means that when adjusting the test mirror with a certain angle, the control unit will give that same angle (despite the fact that the light returns under a double angle).

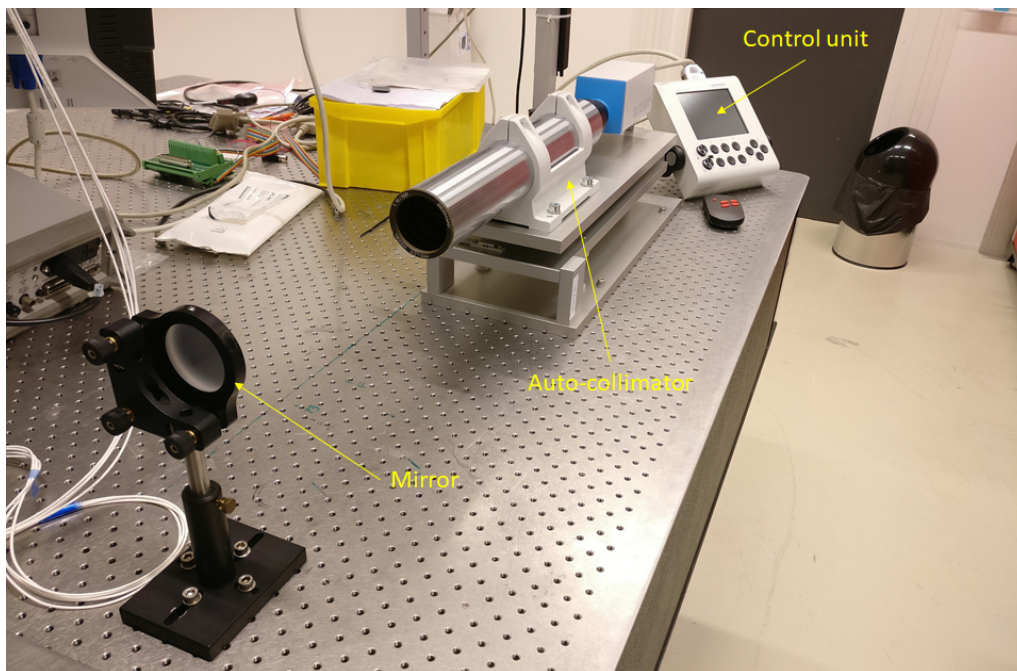


Figure 9.3: ELCOMAT VARIO auto-collimator with its control unit and a test mirror.

The control unit is shown up close in Figure 9.4. The control unit has three main interfaces: a power supply, a laptop interface and an auto-collimator interface. The laptop interface sends out the data seen on the screen in a continuous bit-stream. This data can then be decoded in MATLAB based on the information provided by the manufacturer. A MATLAB script is written to log and store the measurement data continuously. As such, it is possible to perform long-term measurements without interfering with the measurement equipment.

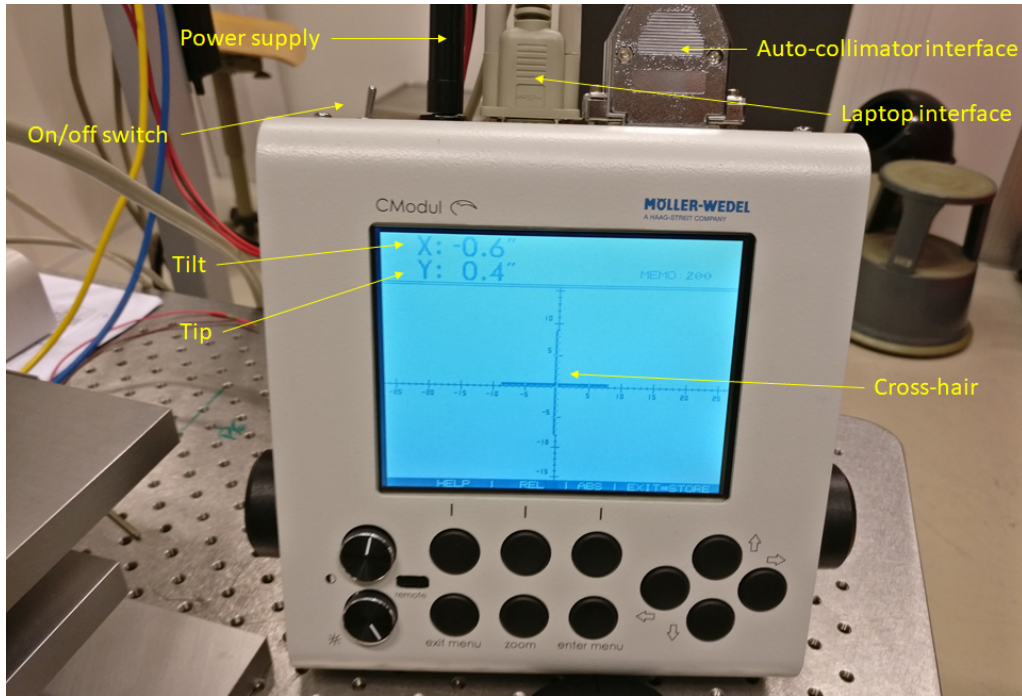


Figure 9.4: ELCOMAT VARIO control unit with its interfaces.

9.4 Double mirror alignment

As mentioned, the auto-collimator is positioned on an alignment stage (see Figure 9.5). However, the range of this stage is very limited (approximately $500 \mu\text{rad}$). The manufacturing and clamping tolerances exceed this range, and thus it is not possible to position the mirror under test within the range. Furthermore, the alignment stage causes the auto-collimator to be positioned much higher than the mechanism.

These issues are mitigated by using two steering mirrors. These mirrors have two main functions: redirect the light to the height of the mirror under test, and coarsely align the light to return to the collimator (within the $500 \mu\text{rad}$ range). The advantage of using two mirrors is also two-fold: first of all, both the auto-collimator and the mirror under test can be mounted parallel/perpendicular to the optical table. Secondly, the laser beam can be aligned in both tip/tilt and x/y position. This last advantage is particularly useful when a small mirror under test is used. For a larger mirror, the position on the mirror is less critical.

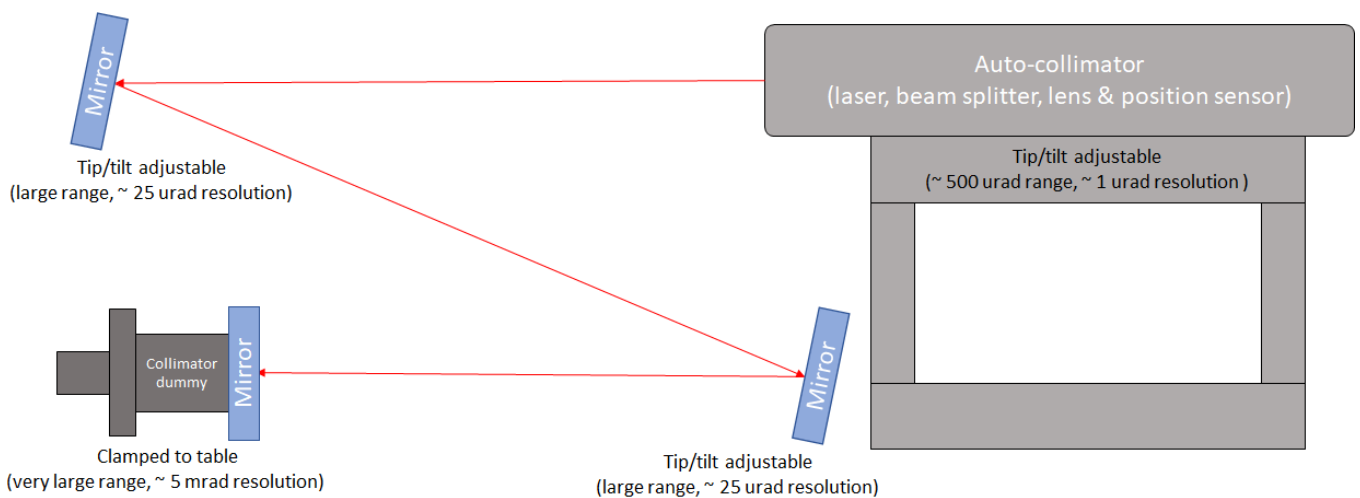


Figure 9.5: Test setup for aligning auto-collimator to the collimator dummy.

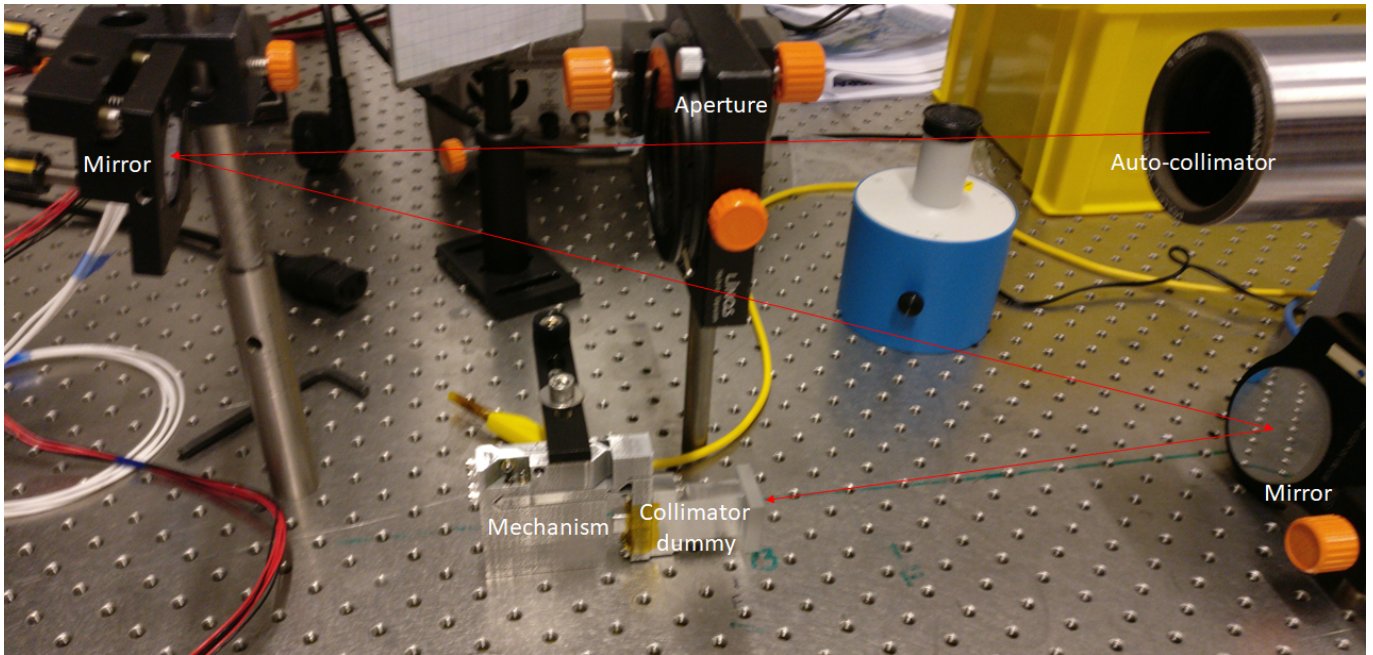


Figure 9.6: Test setup for aligning auto-collimator to the collimator dummy.

A picture of the test setup is shown in Figure 9.6. The beam path is indicated with red arrows. Note that an aperture is added to the system, which is used to take out possible stray light and limit the beam diameter. As such, the outer rings of the mirrors are not used, since these regions tend to have a reduced optical quality. Furthermore, the aperture makes sure that the laser light remains within the system and does not travel into the rest of the room.

Since the auto-collimator laser beam has a very large diameter and low power, it is difficult to see it with the naked eye (even if the light in the room is turned off). Therefore a special, smaller alignment laser can be placed around the auto-collimator tube, see Figure 9.7. The laser can be aligned to return into its source by using the steering mirrors and the auto-collimator alignment stage. After removing the alignment laser, the system is aligned within approximately 25 arc-seconds which can further be corrected using the control unit monitor as a live read-out.

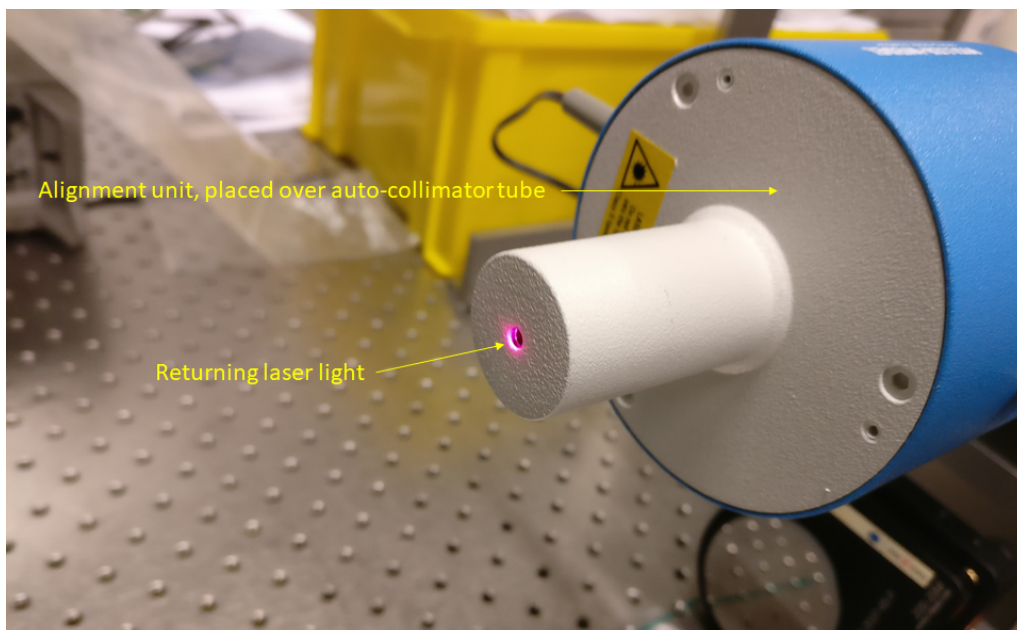


Figure 9.7: Alignment laser placed around the auto-collimator tube.

9.5 Electric heat dissipation

As mentioned, a maximum of 0.6 W is expected to be clipped in the collimator. Since the collimator is replaced with a dummy for the test setup, this heat source also needs to be replaced with an alternative. This heat source is created using electrical heat dissipation. An electric current flowing through a set of resistors leads to a voltage drop U_{tot} given by:

$$U_{tot} = I_{tot}R_{tot} \quad (9.1)$$

Where I_{tot} is the total current flowing through the circuit, and R_{tot} is the total resistance. The total dissipated power P_{tot} in these resistors is then given by the following equation (rewritten to eliminate I_{tot}):

$$P_{tot} = U_{tot}I_{tot} = \frac{U_{tot}^2}{R_{tot}} \quad (9.2)$$

The used resistors are graded for a maximum power of 0.25 W, which is why a set of three resistors is used to allow for 0.6 W total power. The total resistance of these three resistors is given by the following equation:

$$\frac{1}{R_{tot}} = \frac{1}{R_1} + \frac{1}{R_2} + \frac{1}{R_3} = \frac{3}{R} \quad (9.3)$$

Where R_i is the resistance of the i -th resistor. These resistances are assumed to be equal to each other and therefore simplified to R . The required value for R is therefore known:

$$R = 3R_{tot} = 3 \cdot \frac{U_{tot}^2}{P_{tot}} \quad (9.4)$$

Applying the above equation for a 12 V power supply and 0.6 W dissipated power gives $R = 720 \Omega$, as depicted in Figure 9.8. This 12 V power supply is obtained from the auto-collimator power supply by placing the resistors in parallel with the control unit.

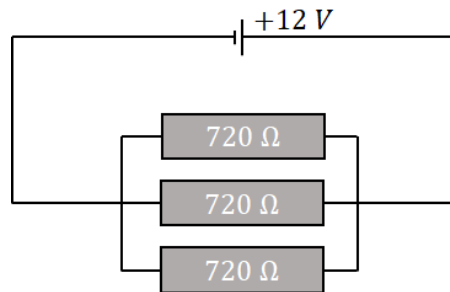


Figure 9.8: Electrical circuit used for dissipating 0.6 W into the collimator dummy.

The thermal stability is also evaluated for three mechanisms placed next to each other, each with its own heat source. This is achieved by placing three sets of resistors in series, with 4 V voltage drop per power source. Applying the same equation for a 4 V supply gives $R = 80 \Omega$, as depicted in Figure 9.9.

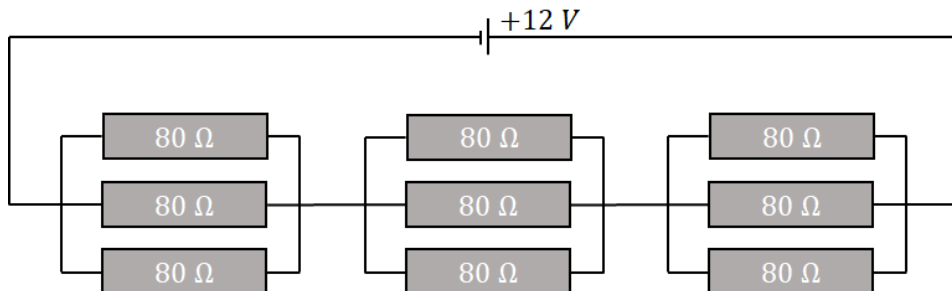


Figure 9.9: Electrical circuit used for dissipating 0.6 W into three collimator dummies.

The resistors are connected to each other by soldering, as shown in Figure 9.10. The ends of the resistors are attached to the power supply using banana plugs. The heat sources are attached to the collimator dummy using a combination of thermal paste and tape.



Figure 9.10: Set of resistors used for dissipating 0.6 W into three collimator dummies.

9.6 Assembling three mechanisms

For the tests that involve the use of three mechanisms, these need to be assembled with the correct spatial separation to represent the real situation. The mechanisms are 13.5 mm wide, and they need to be placed with a 14 mm spatial separation. Therefore the distance between two mechanisms is 0.5 mm. This is done using 6 spare laser cut rings, as shown in Figure 9.11. These rings are aluminium, so they are shielded off using tape to prevent thermal conductance between the mechanisms. This tape also makes sure that the rings remain in their intended position.

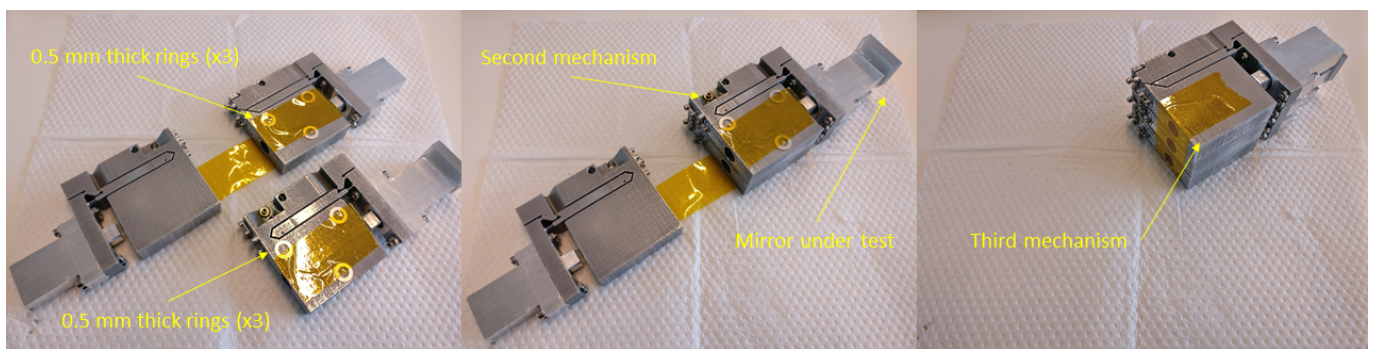


Figure 9.11: Assembling three mechanisms at the correct distance using 0.5 mm thick rings.

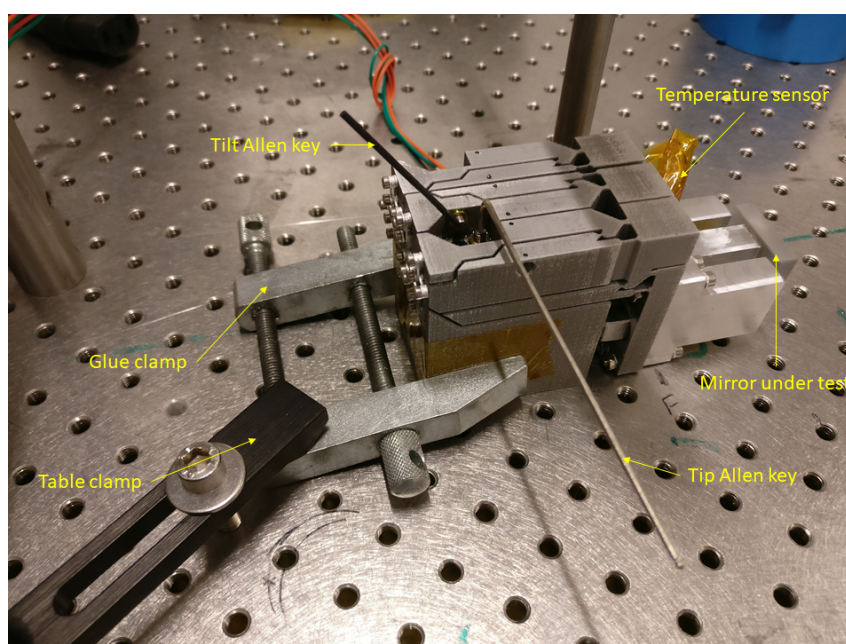


Figure 9.12: Test setup with three mechanisms and three collimator dummies.

The three mechanisms are clamped against each other using a glue clamp. This glue clamp can then be clamped to the table using a table clamp, as shown in Figure 9.12. The picture also shows the temperature sensor used for logging the temperature of the collimator dummy during the thermal stability tests.

9.7 Stability

Since the test setup will be used to measure the stability of the prototype, it is important that the setup itself is stable. This is evaluated using the setup shown in Figure 9.5, where the collimator dummy is clamped directly to the table (without the mechanism attached to it).

There are four main error sources in the test setup. The first is in the ELCOMAT itself: turning on the ELCOMAT system causes the electronics to heat up and this leads to thermal drift, see Figure 9.13. However, after approximately 4 hours the system settles to within $\pm 1 \mu\text{rad}$.

The second error source are $1 \mu\text{rad}$ oscillations with periods in the order of minutes, as also seen in the figure. This is assumed to be either caused by local temperature fluctuations in one or more of the components, or to be simply due to the limited accuracy of the ELCOMAT system.

The third error source is $2 \mu\text{rad}$ measurement noise. This noise is filtered out using a low-pass filter that yields the black lines shown. The cut-off frequency is tuned based on the power spectral density of the original and filtered data, as shown in Figure 9.14. As can be seen, only the most incoherent frequencies are filtered out.

The fourth error source is due to global temperature fluctuations. This is mainly caused by humans entering or leaving the test room. These events can cause significant temperature increase or decrease (in the order of $1 \text{ }^\circ\text{C}$), depending on how long the human remains in the room. This is in part prevented by placing a sign on the door, but unfortunately alignment actually requires a human operator to be present in the room.

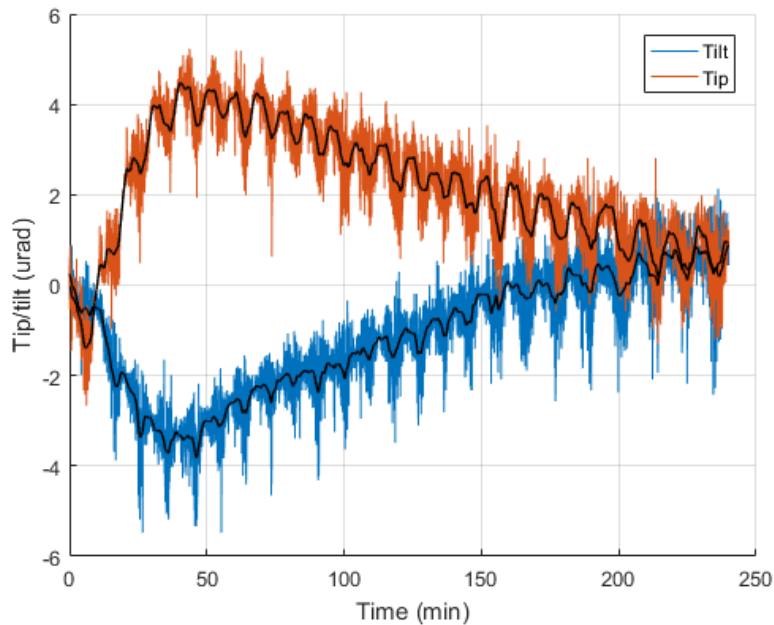


Figure 9.13: Warming up and settling behaviour of ELCOMAT electronics.

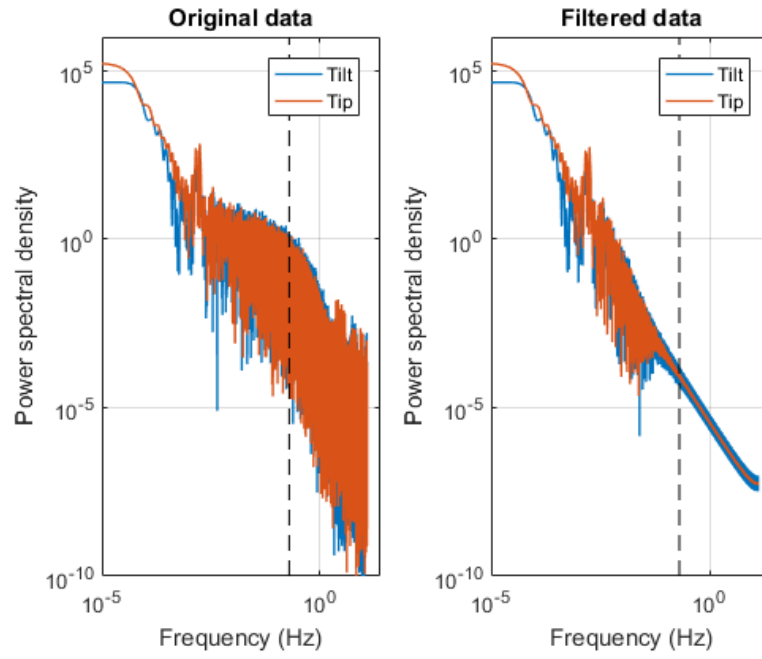


Figure 9.14: Power spectral density of the original and filtered data, showing only incoherent frequencies are filtered.

Chapter 10

Test Results

10.1 Introduction

This chapter presents the most interesting measurement results obtained, discussed in three distinct sections: range and cross-talk, resolution and locking, and thermal stability.

10.2 Range and cross-talk

The designed range is $\pm 0.12^\circ$ (or 2.1 mrad), and the cross-talk 2-4% (depending on whether tip or tilt is actuated). As mentioned, the flexures are thicker than intended, and thus increase the stiffness of the mechanism. Therefore the pre-tension springs can not provide sufficient force. As a result, it is found that the range in one direction is severely limited to approximately 0.5 mrad.

However, the range in the other direction is much better than anticipated. This is due to the fact that the mechanism is allowed to yield during this test. This yielding does result in large-scale creep effects after the test, but these effects settle within a few hours. The entire range is plotted in Figure 10.1, where the 0,0 point is chosen such that the achieved range is covered by the range of the auto-collimator.

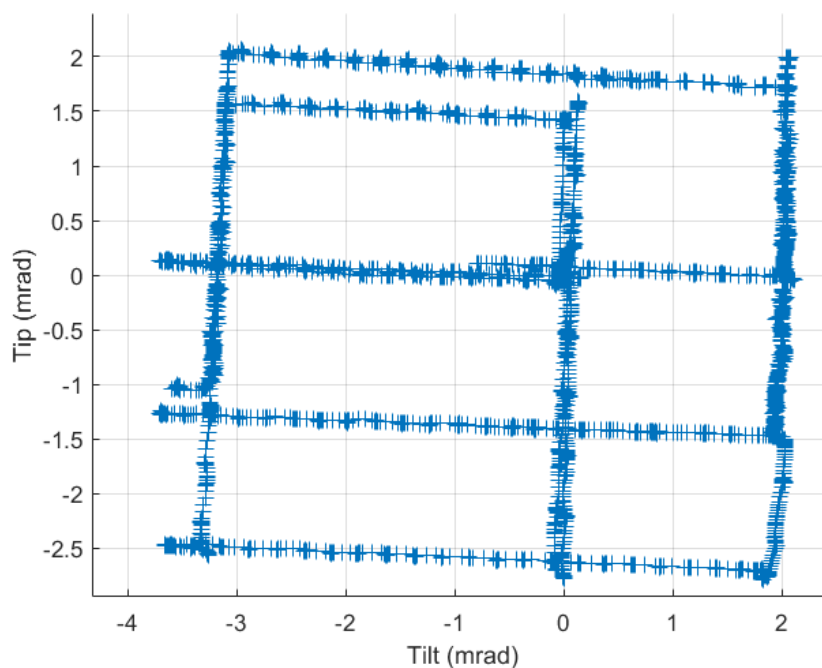


Figure 10.1: All data points acquired while moving across the range of the alignment mechanism. The separate tip and tilt contributions are plotted against time in Figure 10.2.

From this plot it is found that the required range is met. The range in tip is 4.5 mrad, whereas the range in tilt is 5.5 mrad. Note that the range is mostly limited by an increasing friction near the end of the range. As such, it becomes increasingly difficult to actuate the adjustment screw and the mechanism is not actuated any further to prevent catastrophic failure.

Furthermore, it is concluded that the cross-talk is very similar to the anticipated percentages based on simulation. The cross-talk is found to be 3-5% instead of 2-4%. This cross talk can also be seen in Figure 10.2, where both tip and tilt are plotted against time. It can be seen that the tip alignment drifts while tilt is actuated and vice versa. The plot also shows that tip and tilt are actuated in steps. This is because the Allen key can not rotate continuously, but instead needs to be taken out and re-orientated to continue.

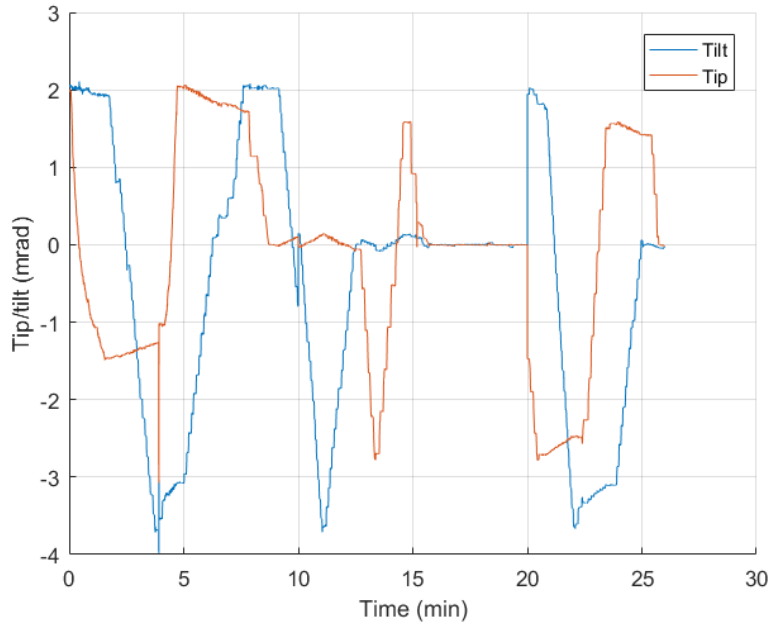


Figure 10.2: All data points acquired while moving across the range of the alignment mechanism, plotted against time. The sharp jumps at 10 and 20 minutes are because too little time was allocated before the measurement. Therefore the plot shows three data sets attached to each other.

10.3 Resolution and locking

The mechanism needs to be aligned and locked with a resolution of $10 \mu\text{rad}$. The process of setting and locking is shown in Figure 10.3 against time. The tip and tilt alignment is plotted against each other in Figure 10.4). Note that the operator waits approximately one minute between each step. This makes it easier to distinguish the events. However, the whole process can easily be performed within 5 minutes, to obtain a setting within $\pm 2 \mu\text{rad}$. Note that this setting and locking resolution is limited by the oscillations and measurement noise in the auto-collimator read-out.

The process of setting and locking is as follows: first the mechanism is aligned to approximately 0,0 using the adjustment screws. Then the outer lock screws of both sets of three are locked, which limits the range of the mechanism even though it is still possible to actuate freely within that limited range. Then the mechanism is aligned to 0,0 again, to compensate for the locking drift. Afterwards, the inner lock screws are locked (as shown in Figure 10.5). And finally the mechanism is aligned again to 0,0 using the adjustment screws.

Note that this final step is only possible when there is enough elastic play in the locking plates. Also, this elastic play should be in the desired direction because the adjustment screw can only be released after the locking plates are all locked. Since the screws are never fully released in this alignment strategy, the system is over-constrained. However, the operating temperature of this part of the mechanism is limited to between 19 and 22 °C. Therefore this over-constraint has a limited effect.

The benefit of the final step is however that a superior setting resolution can be achieved. This is especially the case if the mechanism is left to rest for a few hours after it is aligned and locked. Re-aligning and re-locking after these few hours yields a significant improvement in resolution. When repeating this process a few times, it is possible to align the mechanism to within $\pm 2 \mu\text{rad}$ for long-term stability.

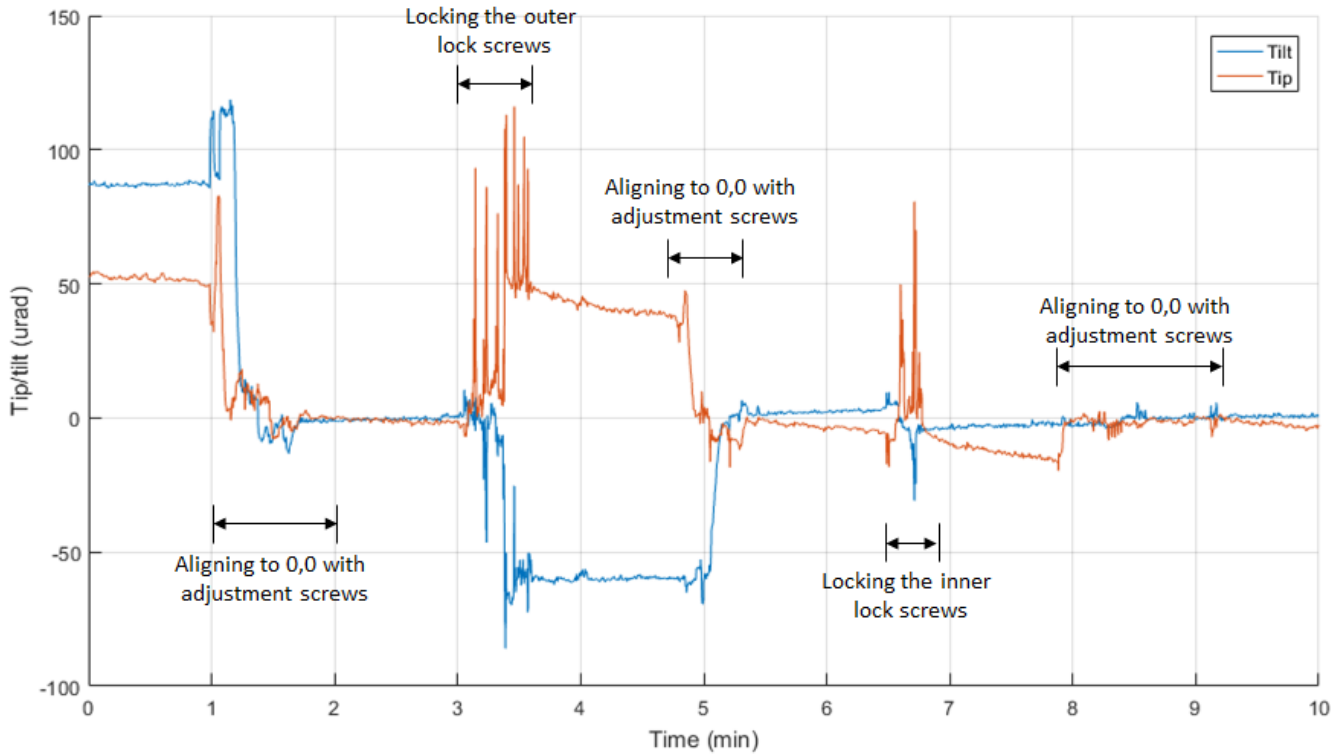


Figure 10.3: Setting and locking over time with all major events indicated.

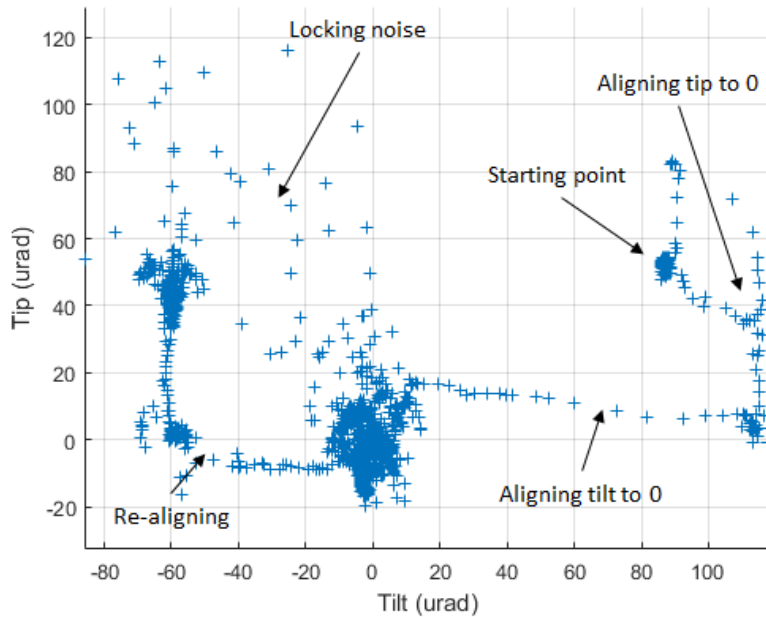


Figure 10.4: All data points acquired during setting and locking.

The drift after locking can also be reduced by allowing for more play in the locking plates. As such, the full range of the mechanism can be reached without unlocking the outer locking screws. This prevents the

drift as a result of locking these screws. Furthermore, the mechanism can be designed to not yield within its range which would further reduce the drift.

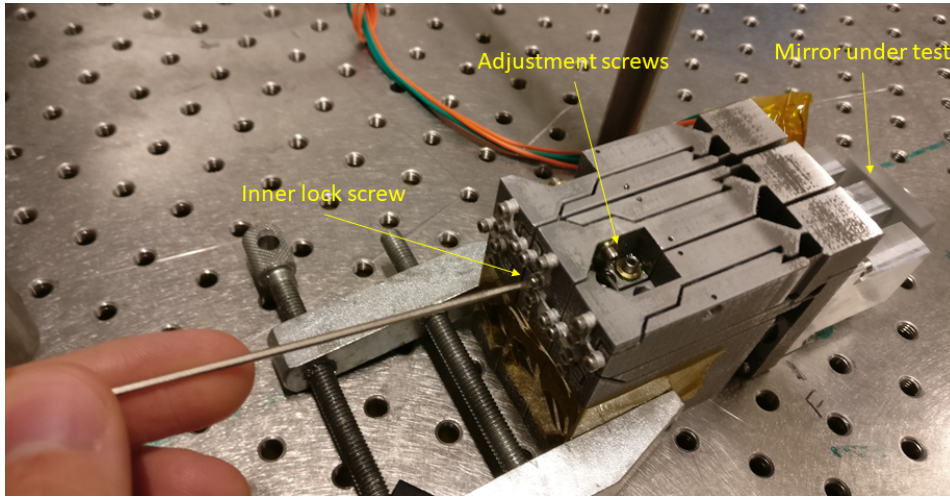


Figure 10.5: Alignment tool used for locking.

10.4 Thermal stability

The thermal stability is tested for two different scenarios: first a single mechanism with a single collimator dummy is tested, and then an assembly of three mechanisms with three collimator dummies is tested. The heat source is mounted in either one of two possible locations, which are indicated in Figure 10.6.

The first location gives a better representation of the actual heat source location, but is discarded because part of the heat flows into the surrounding mechanism without first flowing through the collimator dummy. Since it is difficult to predict which portion of the heat flows as intended, it is difficult to match the FEM simulation to this scenario. Instead, location 2 is used for the results presented in this chapter.

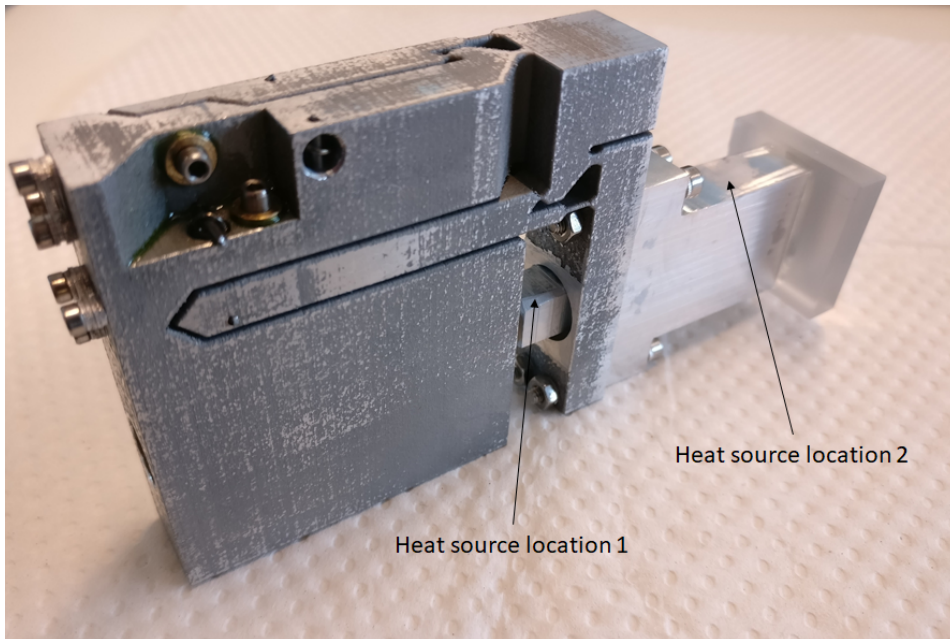


Figure 10.6: Locations used for heat source.

One set of measurement data of the thermal drift for the single mechanism test is shown in Figure 10.7. The measurement is performed by first aligning the test setup to 0,0. Note that the test setup rather than

the mechanism is aligned to prevent the drift found in the previous tests from dominating the thermal tests. Instead the situation where the drift is settled is represented. After the test setup is aligned, the operator walks out of the room. After 90 minutes the operator returns to the room, connects the heat source and leaves the room again.

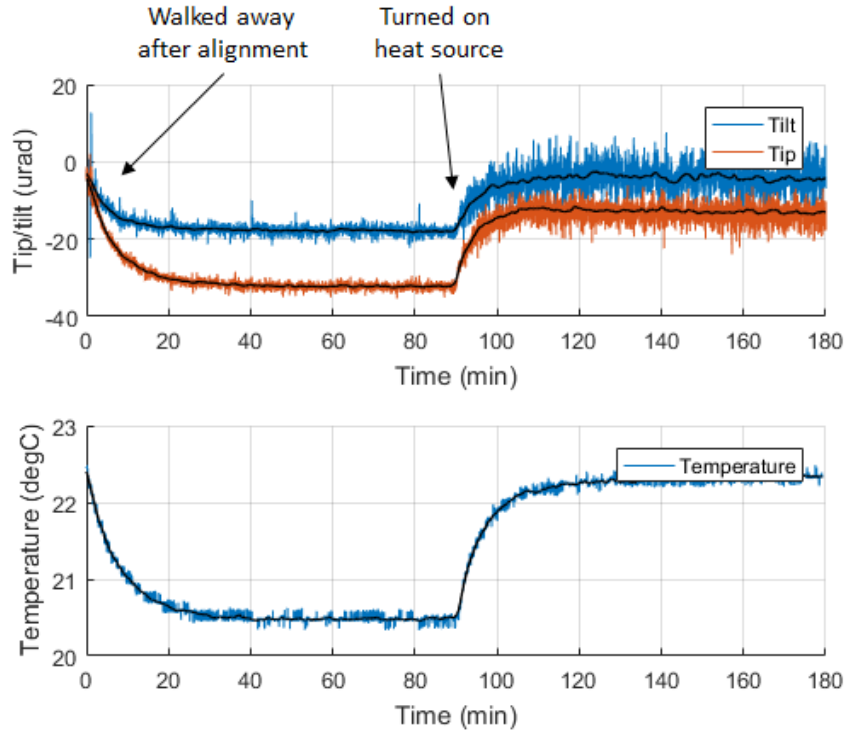


Figure 10.7: Thermal drift as a result of turning on the heat source.

These events can be recognised in the figure. Both the tip/tilt alignment and the temperature of the collimator dummy are plotted. The temperature sensor is pressed against the collimator dummy using tape. Note that there is a 20 μrad drift for tilt and 30 μrad drift for tip as a result of leaving the room, which is matched by an approximate 2 $^{\circ}\text{C}$ temperature decrease as the collimator dummy takes on the temperature of the room.

After 90 minutes, the heat source is turned on as a result of which the collimator dummy heats up by 1.85 $^{\circ}\text{C}$. The associated drift for tip is found to be between 18 and 20 μrad , based on three similar tests. The tilt drift is between 2 and 15 μrad . This large difference is due to the method and force used for clamping the mechanism to the table. The direction and force with which the mechanism is clamped restricts its thermal expansion. The best tilt drift is achieved for clamping the mechanism from its sides rather than from the top, and with a small clamping force.

Note that this effect is negligible for the tip drift, because the tip mechanism is not directly connected to the base of the printed block whereas the tilt mechanism is.

One set of measurements for the three mechanism test is shown in Figure 10.8. A similar test procedure is applied, but this time the collimator dummy is already at room temperature at the start of the test.

When the heat sources are turned on, the collimator dummy temperature increases by 3 $^{\circ}\text{C}$. The associated drift for tip is between 26 and 30 μrad , and the drift for tilt is between 20 and 30 μrad . Note that the tilt drift is even more unstable as a result of the clamping force. Presumably the clamping force varies locally during the measurement as a result of the increase in temperature.

The temperature increase and tip drift scale approximately linearly for this data set. This is expected, because the greatest drift source is due to the thermal gradient between the collimator dummy and the mechanism. The collimator dummy bends because the extra flexure designed to avoid this is absent in this prototype.

The linear scaling is presumably also a result of how the heat sources are implemented. The heat sources are connected to each other with soldering tin which is a good conductor. Therefore it is likely that the heat of the neighbouring sources are added to each other, and that the extra drift for three mechanisms is because more heat flows into the central collimator dummy directly.

The time constant also scales along with the temperature increase and tip drift. For the single mechanism the time constant is between 30 and 40 minutes, and for the three mechanisms this time constant is 60 minutes.

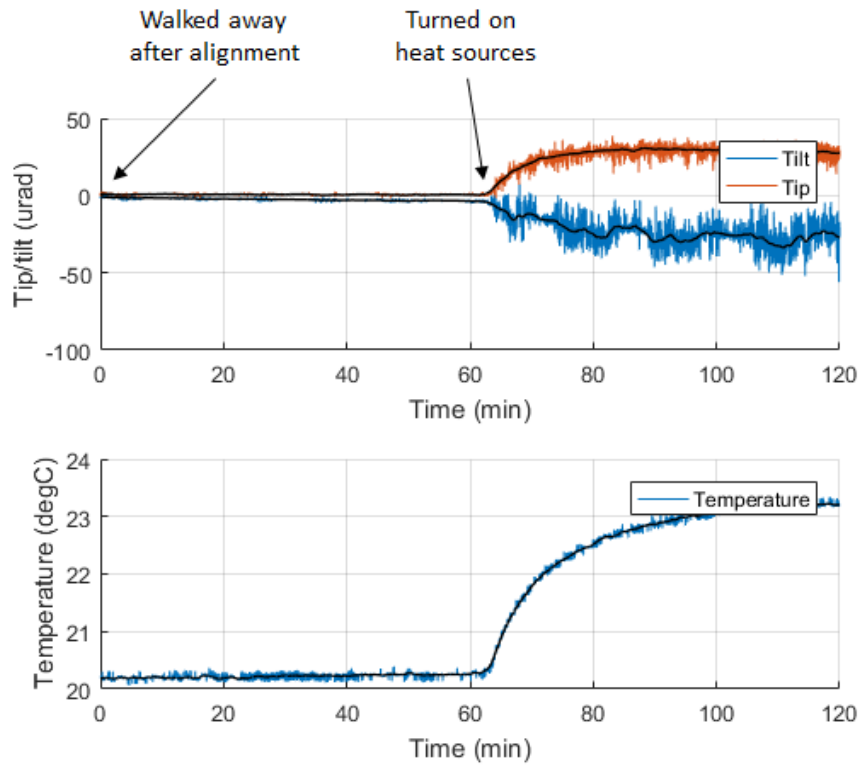


Figure 10.8: Thermal drift as a result of turning on the heat sources, with three mechanisms and heat sources.

Chapter 11

Discussion

11.1 Introduction

In this chapter, the lessons learned from the prototype are discussed as well as the steps taken to match the thermal FEM simulation to the measurement data. The chapter is concluded with an updated model for the final design.

11.2 Lessons learned from prototype

11.2.1 Rapid prototyping tolerances

As mentioned in Section 8.2, the perpendicularity between the surfaces of the printed parts is better than anticipated. The tolerance on this angle is in the order of the 0.033° requirement set and therefore needs no post-processing steps.

The thickness of the flexures on the other hand are printed to worse tolerances than anticipated. This is because these elements have a much smaller feature size which is incompatible with the manufacturing technique. For this mechanism a decreased stiffness does not decrease the performance, whereas an increased stiffness does.

Therefore a possible mitigation strategy is to design the flexures thinner (for instance 0.3 mm thick), such that the achieved flexures are 0.6 mm thick (assuming a similar tolerance). However, decreasing the feature size can lead to issues with the local material properties.

An alternative mitigation strategy is to decrease the thickness in a post-processing step. However, the small feature size of the flexures limits the available techniques.

A third mitigation strategy is to design for thicker flexures. However, increasing the thickness of the flexures also increases the stress levels (if the range of motion remains the same). Furthermore, increasing the required pre-tension force is challenging because of the limited footprint available.

11.2.2 Assembling challenges

Three main challenges are identified for the assembling process: mounting the springs, the adjustment screw bushels and the collimator (as presented in Chapter 8 and Section 9.2).

The issue of mounting the springs can be mitigated by increasing the diameter of the spring rings, or by decreasing the diameter of the spring rod or the pincet.

The issue of mounting the adjustment screw bushels can be mitigated by improving the tolerances on the holes for these bushels and using Loctite to mount the bushels in these holes.

The issue of mounting the collimator can be mitigated by increasing the footprint available surrounding the nut (see Figure 9.1).

11.2.3 Locking drift

The short-term locking drift for locking the inner lock screw (see Figure 10.5) is between 5 and 10 μrad (see Figure 10.3). This is higher than the 3 μrad anticipated based on literature, but in the same order of magnitude. The long-term locking drift is however much larger than anticipated.

This long-term is found to settle within a few hours after locking. The mechanism can be set and locked within $\pm 2 \mu\text{rad}$ when re-aligning and/or re-locking at least three times (separated by resting periods of a few hours).

11.2.4 Hysteresis in cross-talk

It was found that adjusting tip gives a cross-talk into tilt that is subject to hysteresis. The most likely explanation for this is the screw play. However, this can be compensated for because the cross-talk is not bidirectional. Therefore the tip can be adjusted first, and then the tilt. This way the hysteresis in the cross-talk can be avoided.

11.2.5 Heat source

The electric heat source is found to be unreliable in the used test setup. Not all heat flows into the collimator dummy directly, and the exact proportion is unknown.

This can be mitigated by using an alternative heat source, for example a high-power laser. If the collimator dummy tip is made highly absorbing, such a laser can be directed at the collimator tip. Thus all heat is guaranteed to flow into the collimator dummy tip first. Unfortunately, lasers in the order of tenths of Watts requires more stringent safety precautions.

11.2.6 Mounting to table

The direction and force used for mounting the mechanism to the table is found to strongly influence the thermal stability tests. Therefore the situation as used in the final design should be properly simulated. This can be done by adding the mounting feature and mounting the mechanism to a dedicated breadboard, as shown in the detailed design (see Section 6.3.2).

11.3 Match between simulation and measurements

As mentioned in Section 10.4, the location of the heat source for the final set of tests is chosen to match the test results to the thermal FEM simulation and thus verify the model. The updated model is shown in Figure 11.1. The drift at the back of the collimator dummy (where the mirror under test is mounted) is 18.5 μrad for tip and 1.3 μrad for tilt while the temperature increase of the collimator dummy is 1.9 $^{\circ}\text{C}$.

Note that this is very similar to the thermal test results for a single mechanism. These test results showed a 1.85 $^{\circ}\text{C}$ temperature increase, a tip drift between 18 and 20 μrad and a tilt drift of 2 μrad for the least clamping force. Based on this, it is found that the test setup differs from the original FEM simulation in five ways.

11.3.1 Conductance collimator dummy

First of all, the conductance of the collimator dummy was assumed to be 234 W/mK (based on aluminium 1060 [34]). Aluminium 1060 is very pure and therefore a good conductor. Since the exact type of aluminium used for the collimator dummy is unknown, a worst case conductance of 160 W/mK is chosen (based on aluminium types such as 6061-T6 [30]).

This reduction in conductance yields an increase in temperature gradients and therefore an increase in drift. As a result, the tip drift increases from 10 μrad to 11.5 μrad while the tilt also increases but not significantly.

11.3.2 Thermal contact resistance

The main difference between the original FEM simulation and the updated model is the thermal contact resistance. This resistance was assumed to be negligible in the original model because the contact area is very small. This small contact area is achieved by placing bolt rings between the collimator and the mechanism.

Thermal contact resistance for aluminium is typically in the order of $10000 \text{ W}/(\text{m}^2\text{K})$ [36], but assumed to be $15000 \text{ W}/(\text{m}^2\text{K})$ due to the small contact area. This is translated to a thermal conductance of $3.7 \text{ W}/\text{mK}$ in the bolt rings between the collimator and the mechanism and the bolt rings between the mechanism and the locking plates.

This conductance is much lower than $160 \text{ W}/\text{mK}$ and therefore there is an increased thermal gradient between the collimator and the mechanism. This gradient leads to a large drift in tip due to the bending of the collimator. As mentioned before, the extra flexure designed to mitigate this bending is missing in the prototype.

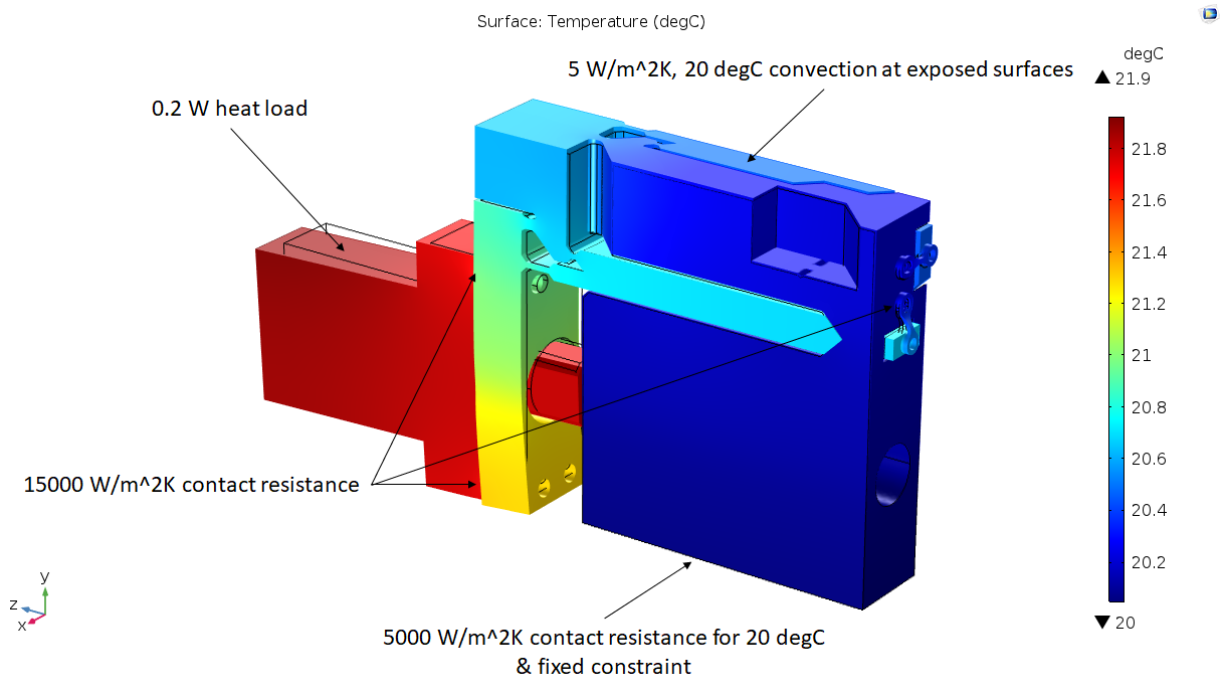


Figure 11.1: Updated model to match test results.

11.3.3 Lower achieved heat load

The combined effect of the thermal contact resistance and the missing flexure yields an expected tip drift of $56 \mu\text{rad}$, a tilt drift of $3.8 \mu\text{rad}$. However, the simulated temperature increase is $5.7 \text{ }^\circ\text{C}$. Therefore, it is concluded that only a third of the heat load is applied to the collimator dummy. The rest of the heat is assumed to be lost in the banana plugs connecting the heat source to the power supply, and due to convection.

As such, the stated results of the updated model ($18.5 \mu\text{rad}$ tip drift, $1.3 \mu\text{rad}$ tilt drift and $1.9 \text{ }^\circ\text{C}$ temperature increase) are achieved for a heat source of 0.2 W instead of 0.6 W .

11.4 Updated model for final design

Translating the lessons learned into an updated model for the final design yields the simulation results shown in Figure 11.2. The same parameters are used as shown in Figure 11.1, except that the heat load is changed back to 0.6 W . Also note that the collimator has improved detail to properly represent the thin walls in the collimator cylinder.

The simulation results show a tip drift of $10.4 \mu\text{rad}$, a tilt drift of $4.7 \mu\text{rad}$ and a temperature increase of $7 \text{ }^\circ\text{C}$. However, these results are for modeling for a single collimator and mechanism. In reality, the mechanism

is surrounded by other mechanisms, thus the convection will be lower because less surfaces will be exposed and because the temperature surrounding the mechanism will increase. Unfortunately, the effect of these other mechanisms could not be properly tested due to issues with the heat sources and therefore this is left out of the simulation for now.

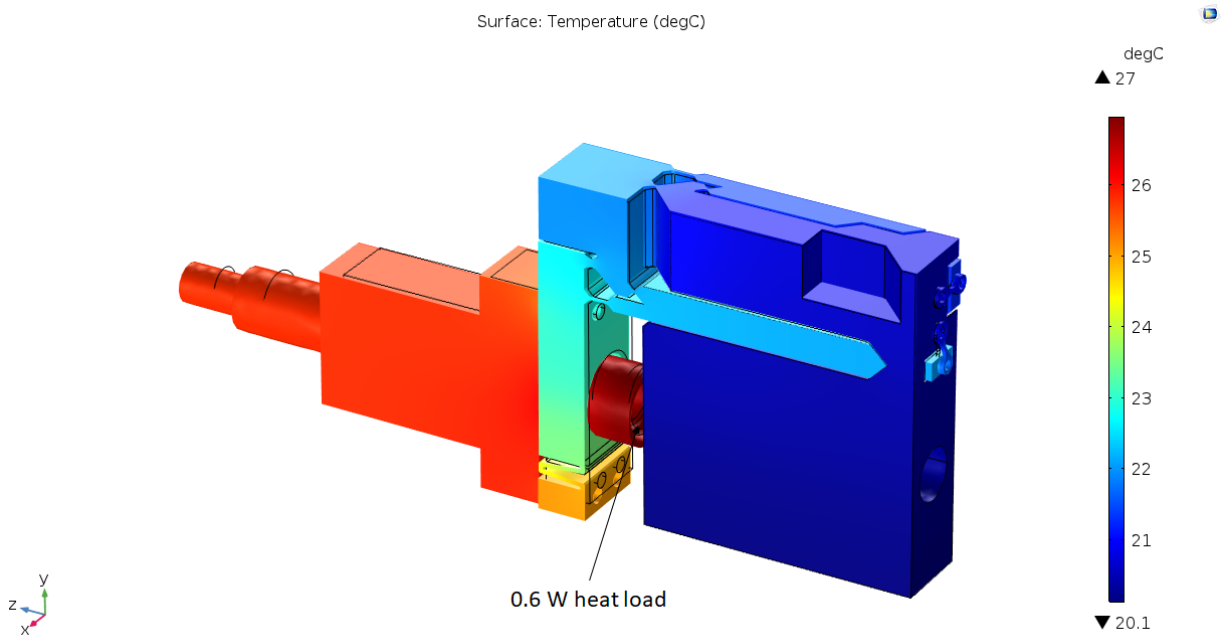


Figure 11.2: Updated model for the final design to match test results.

Chapter 12

Conclusions and recommendations

12.1 Conclusions

The aim of this thesis has been two-fold: to show the need for achieving state-of-the-art alignment specifications with strict footprint constraints, and to defend the steps taken to achieve these requirements.

12.1.1 Literature survey

The first aim has been achieved by presenting the design process leading up to the required design challenge. The most important conclusions are:

- The lasers used for the bulk multiplexer need to have a high power to compensate for the losses in the link budget.
- The channel spacing for the used optical frequencies needs to be stringent in order to reach the targeted data rate.
- The dispersion of the used grating needs to be minimal to ensure that the signal can be reconstructed at the satellite.
- As a result of the above two points, the spatial separation between the collimators is limited.
- The collimators have a limited width to cope with the limited spatial separation, leading to a significant amount of clipped power.
- The collimators need to be aligned with strict specifications to minimize the lost power at the satellite and ensure that the signal can be reconstructed.

12.1.2 Design

The second aim has been achieved by presenting the design process leading up to the final recommended design. The most important conclusions for the design phase are:

- An alignment mechanism using a lever ratio is required to meet the alignment specifications for the strict footprint constraints.
- The clipped power leads to a challenging thermal design requirement for the alignment mechanism.
- The mechanism needs to be 3D-printed because of its complicated geometry.
- The requirements can also be met using a beam steering concept, thus eliminating the stability concerns.

12.1.3 Validation

The second aim is expanded upon by validating the design. The most important conclusions from the prototype phase are:

- Rapid prototyping can be used for creating precision mechanisms, provided that the thickness of small feature size elements is not critical.
- The required range can be easily achieved, provided that the mechanism flexures are allowed to yield.
- The setting and locking requirements can easily be achieved, provided that the mechanism is re-aligned several times with a few hours between.
- The required thermal stability can be achieved for a single mechanism, but not yet for an assembly.

12.2 Recommendations

Based on the lessons learned from the prototype, there are four main recommendations to be made for the final design of a collimator alignment assembly for a high-power bulk multiplexer used in ground-to-GEO laser communication.

12.2.1 Replace rings

The bolt rings used between the collimator and the designed mechanism can be replaced by extending features on the mechanism to decrease the number of parts. This should reduce the thermal contact resistance as well as decrease the assembly challenges. The thermal contact resistance can further be reduced by polishing the extending features.

12.2.2 Reduce heat load

The clipped power and thus the heat load can be reduced by cherry-picking the optical fibers for the largest mode field diameter (discussed in the supporting document). Alternatively, the clipped power can be reduced by re-designing the collimator. The width of the collimator can be increased to match the width of the mechanism without causing any penalties to the rest of the system.

12.2.3 Remove lever ratio

It was found that the setting and locking resolution is much better than anticipated, provided that the system is re-aligned several times. As such, this resolution can be increased by a factor 2 while still being compatible with the requirement. The main contribution of the thermal drift is due to the double flexure path used in the lever ratio concept. Therefore removing the lever ratio would dramatically improve the thermal stability of the mechanism.

12.2.4 Beam steering

The thermal stability can also be improved by using the double wedge concept for beam steering, rather than aligning the collimator. This takes out all major instability sources because the collimator can be locked to the solid ground.

The smallest possible rotation needs to be tested in order to determine the allowed dynamic range. If this dynamic range is insufficient, the wedge mechanism can instead be coarsely aligned using for instance shims.

Part IV

Appendices

Appendix A

Divergence

Divergence can be understood from the fact that in physical optics, there is no such thing as a light ray or beam. Instead, an electromagnetic field induced in one specific location always travels in all directions from that location (similar to how water waves travel when a rock is thrown into a lake). However, when an electromagnetic field is induced in multiple specific locations, the traveling fields will interfere with each other in specific patterns.

The location where the electromagnetic field is induced can be considered as a point source (see Figure A.1). Such a point source can be described in a two-dimensional wave equation:

$$E = E_0 \cos\left(k\sqrt{x^2 + y^2} - \omega t + \phi\right), \quad \omega = ck, \quad k = \frac{2\pi}{\lambda} \quad (\text{A.1})$$

Where k is the wave number in rad/m, x and y are the two-dimensional coordinates, ω is the electromagnetic frequency in rad/s, ϕ is the relative phase shift in rad, c is the speed of light in m/s, and λ is the wavelength.

Interference is the effect where the waves either strengthen or weaken each other, because they are either in phase or not. The interference patterns across space therefore depend on the locations of the point sources, their relative phase, their individual field strengths, and their wavelengths.

In the waist of a Gaussian beam, the wavefront is flat: meaning that all point sources along the cross section of the waist are in phase with each other. When considering an infinite amount of point sources placed on one line segment, the interference pattern results in a Gaussian beam.

The interference pattern of 11 point sources placed next to each other is shown in Figure A.2, with a waist diameter of 10 μm . Here, one time frame is shown to compare to the single point source seen in Figure A.1. In Figure A.3, the time average of the intensity distribution is shown. This is the interference pattern that can actually be measured for optical wavelengths. Such a measurement is simulated in Figure A.4, by plotting the intensity in the far field (or actually, the right side of Figure A.3) against the y -coordinate.

The resulting plot is very similar to the intensity distribution of a Gaussian beam, and would actually be precisely the same when using sufficiently high resolutions and taking the intensity at a large enough far field distance.

The field strength by point source 1 at one specific location ($x = L, y = h$) can be described by rewriting Equation (A.1) using the definitions specified in Figure A.5:

$$E_n = E_0 \cos\left(k\sqrt{L^2 + (h - w/2)^2} - \omega t + \phi\right) \quad (\text{A.2})$$

The interference can then be described as the sum of all N point sources ($n = \{1, N\}$):

$$E_{tot} = \sum_{n=1}^N E_0 \cos\left(k\sqrt{L^2 + (h - w/2 + (n-1)d)^2} - \omega t + \phi\right) \quad (\text{A.3})$$

Since the beam waist diameter w is equal to $(N-1)d$, and the tangent of the far field angle $\tan\theta$ is equal to h/L , this equation becomes:

$$E_{tot} = \sum_{n=1}^N E_0 \cos \left(k \sqrt{L^2 + \left(L \tan \theta - w/2 + \frac{w(n-1)}{N-1} \right)^2} - \omega t + \phi \right) \quad (\text{A.4})$$

When calculating this interference for a wavelength λ of 1550 nm, a far field distance L of 100 μm , a waist diameter w of 10 μm , and 2001 point sources, the time average intensity is as shown in Figure A.6. This intensity is plotted against the far field angle θ , and the $1/e^2$ line and the divergence angle calculated using Equation (2.1) are plotted as well.

Since the equation is meant to give the divergence angle at the $1/e^2$ line, it can be seen that there are some small errors in these calculations. This is presumably because the intensity of each point source was chosen to be equal, while in reality the intensity distribution in the point sources will be Gaussian as well.

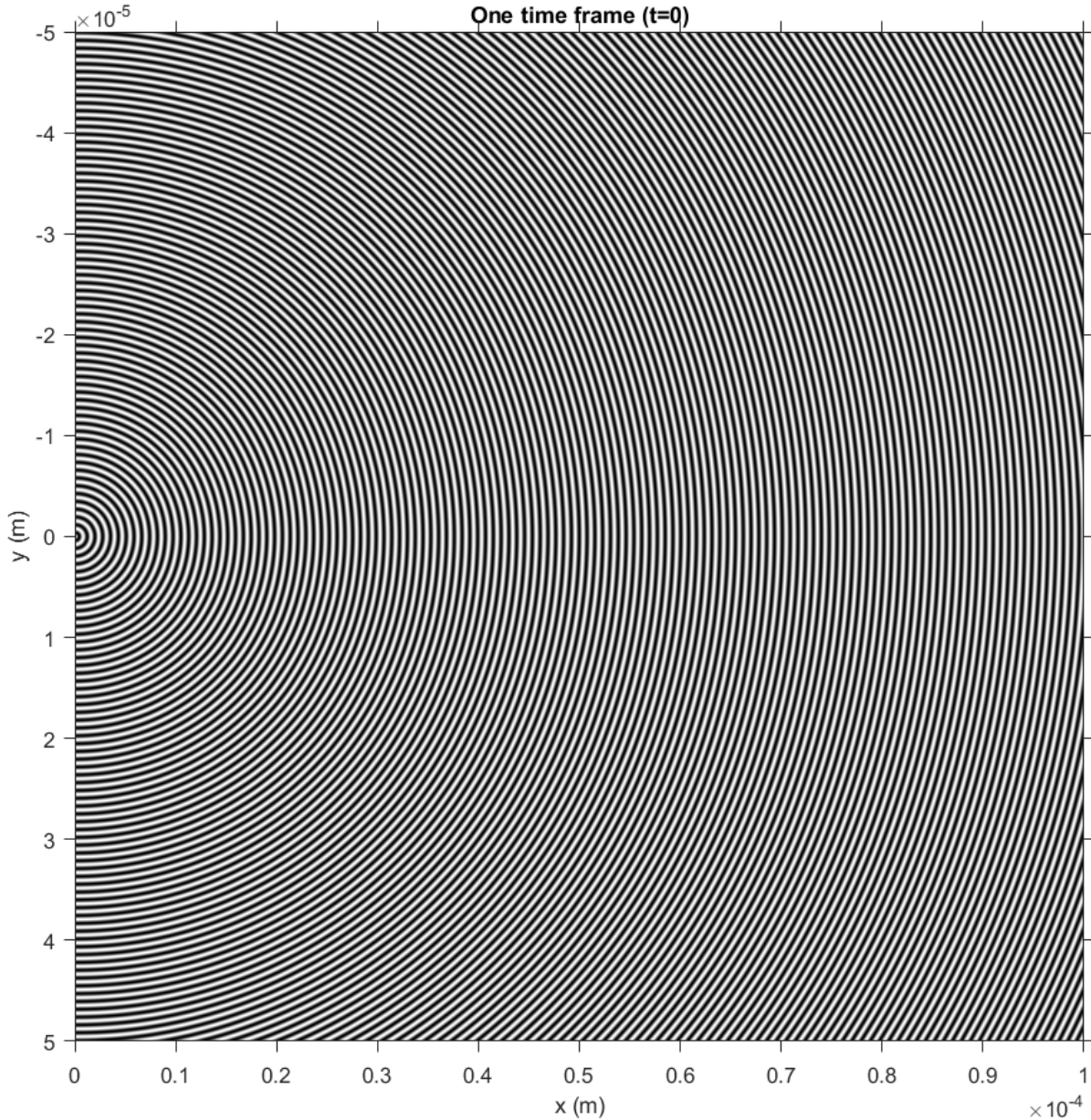


Figure A.1: One point source and its intensity propagation for a single time stamp.

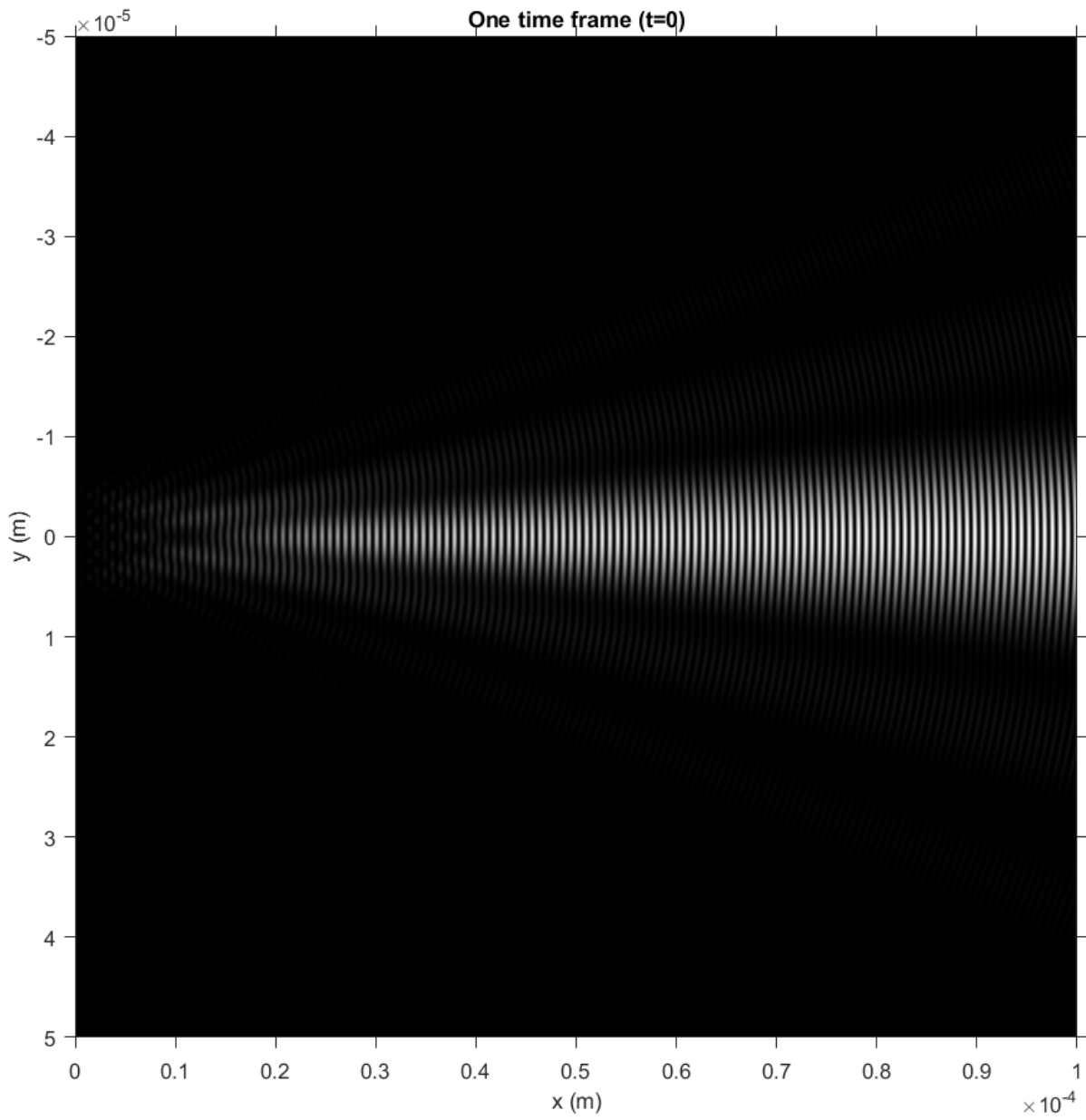


Figure A.2: Eleven point sources and their intensity propagation for a single time stamp.

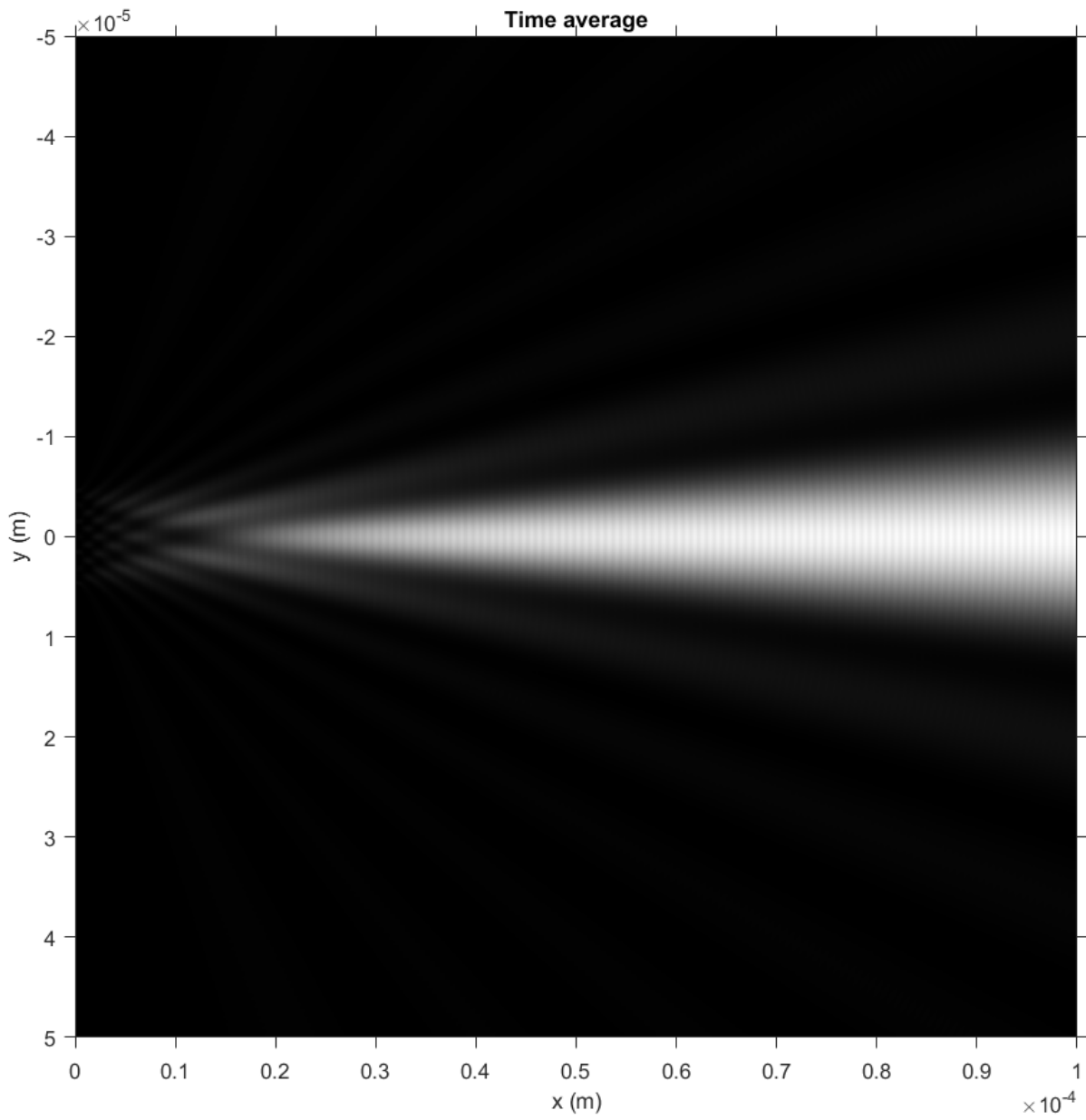


Figure A.3: Eleven point sources and their intensity propagation for a time average.

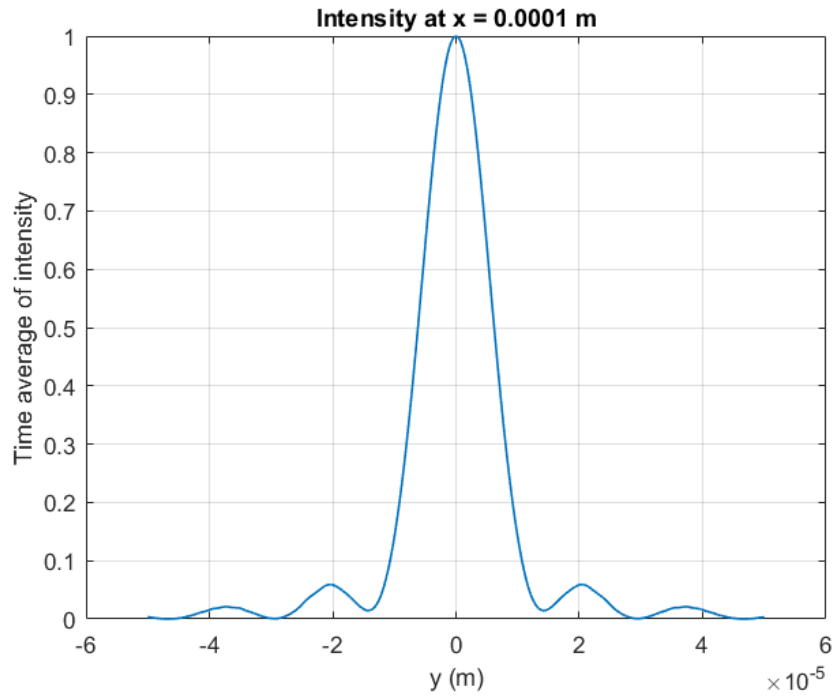


Figure A.4: Eleven point sources and their intensity propagation for a time average, at the far field (right side) of Figure A.3.

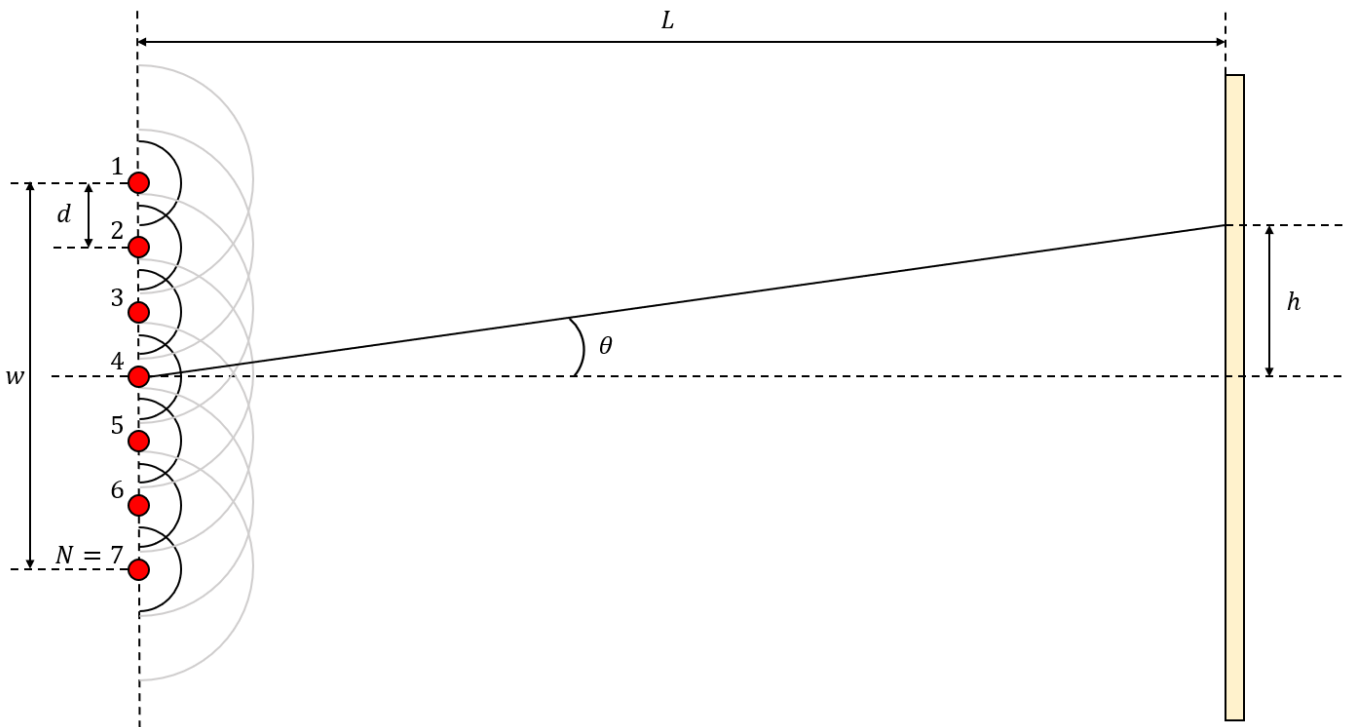


Figure A.5: Schematic drawing of the dimensions used in the calculation of the divergence of a Gaussian waist.

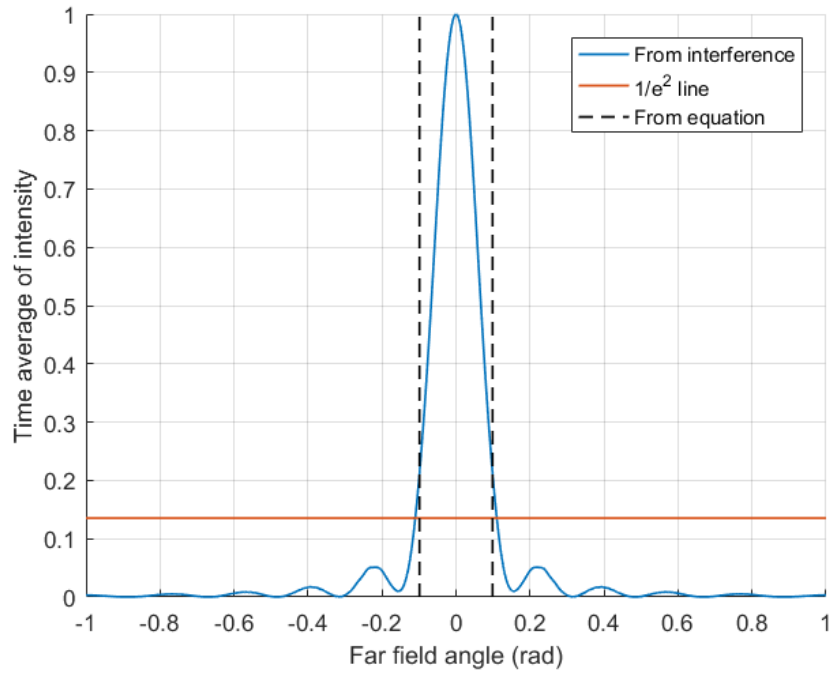


Figure A.6: The time average intensity plotted against the far field angle. The $1/e^2$ line and the divergence angle calculated using Equation (2.1) are plotted as well.

Appendix B

Grating interference

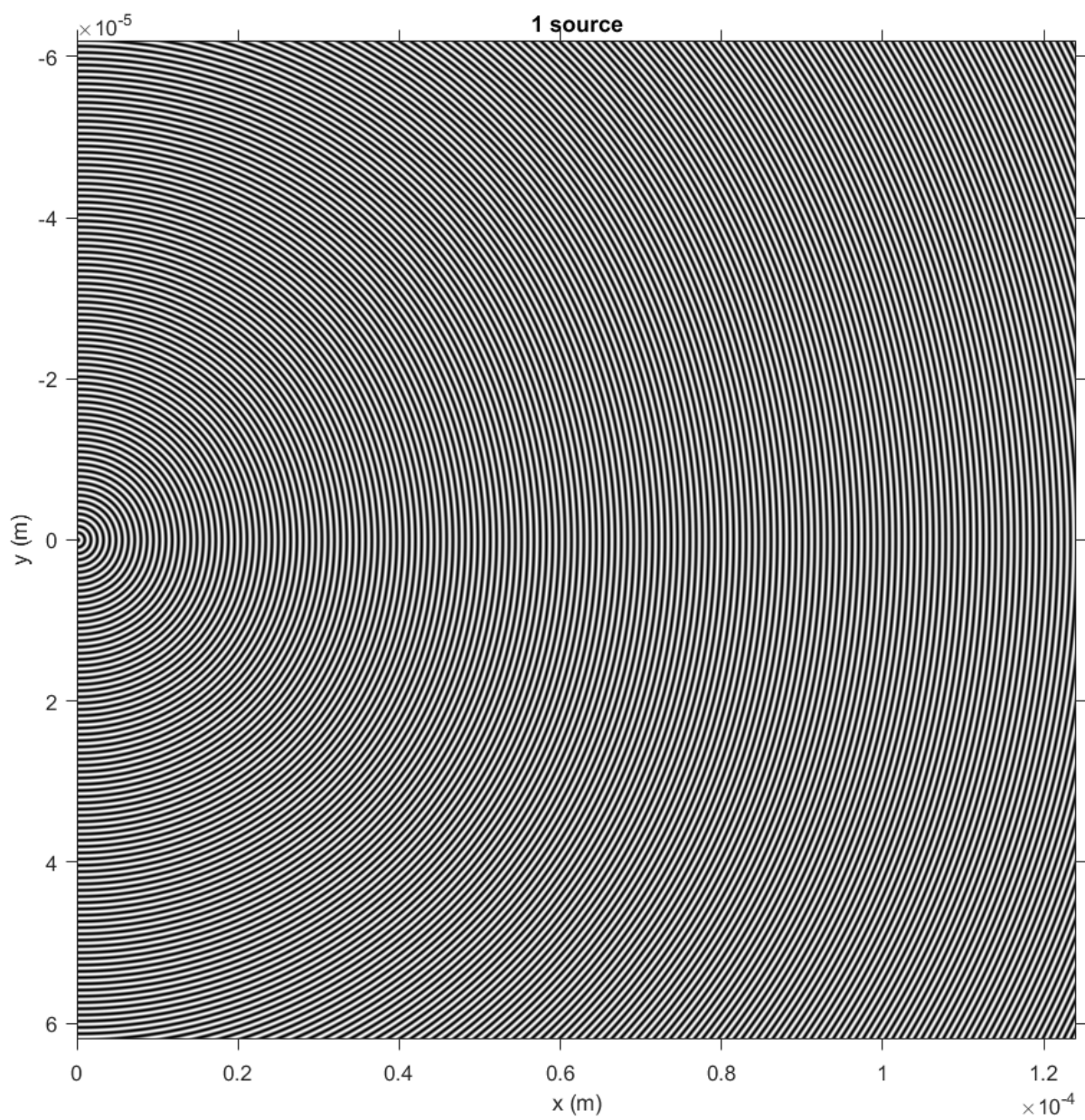


Figure B.1: Intensity distribution for 1 source, at one time frame.

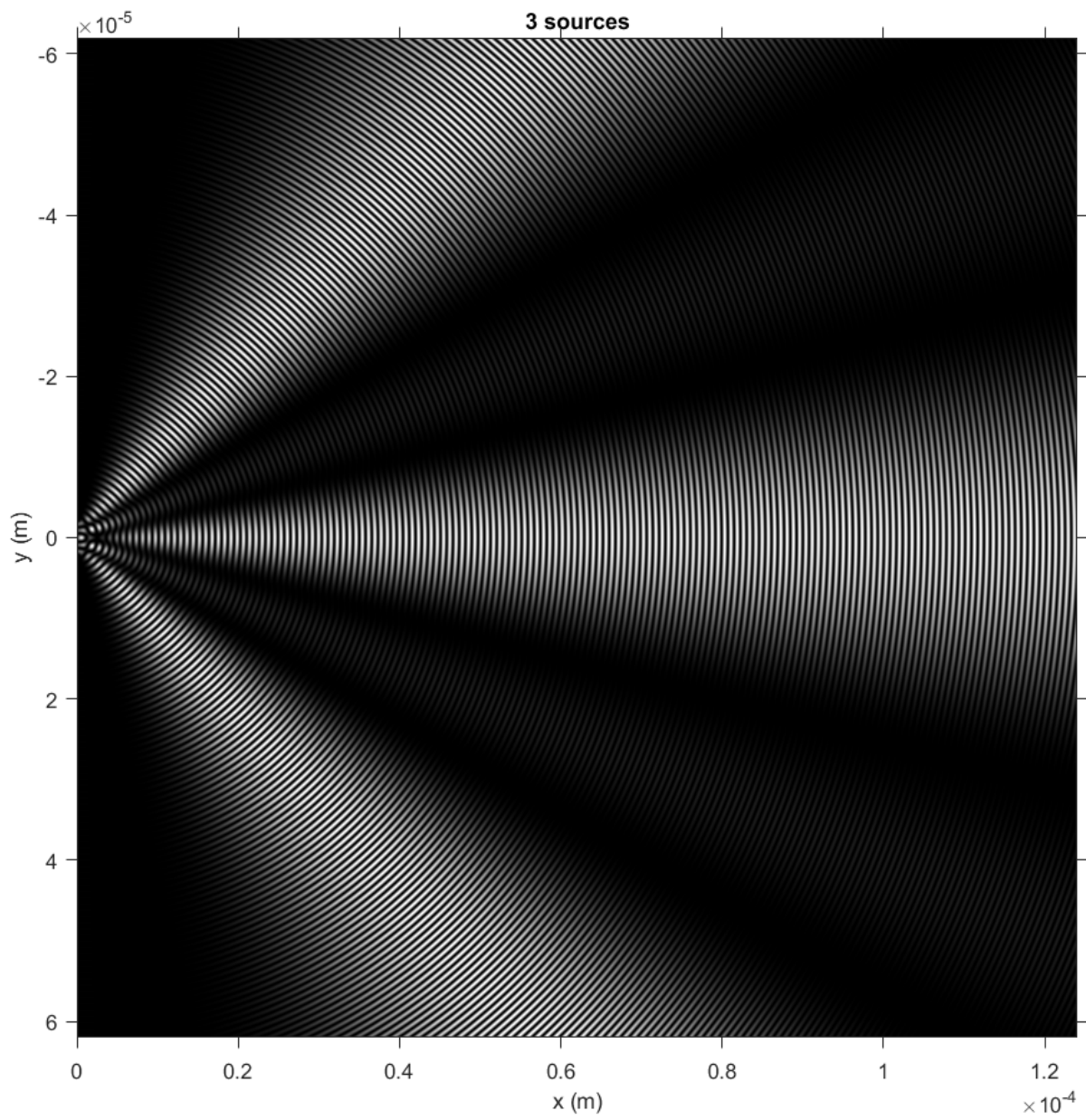


Figure B.2: Intensity distribution for 3 sources, at one time frame.

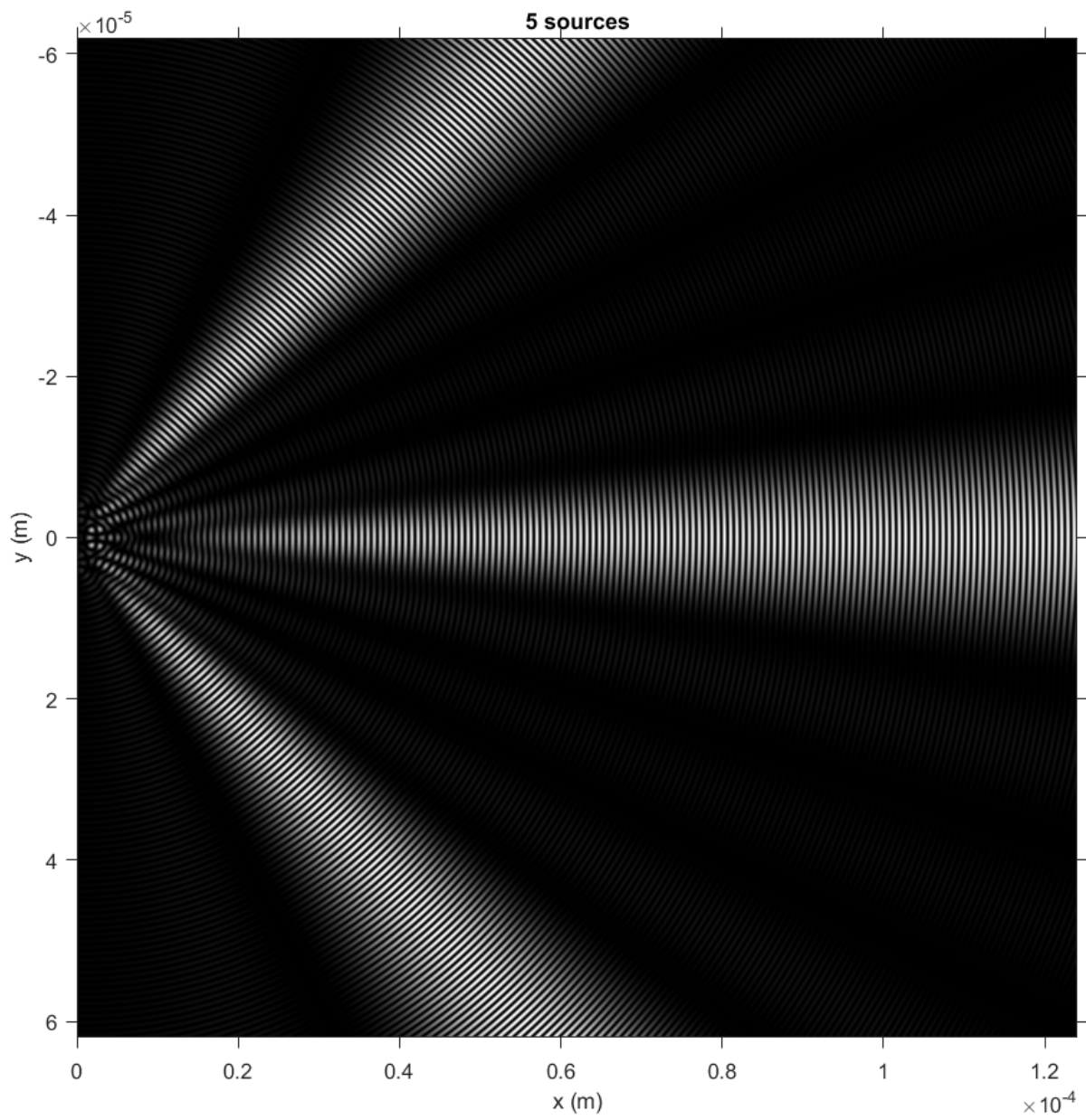


Figure B.3: Intensity distribution for 5 sources, at one time frame.

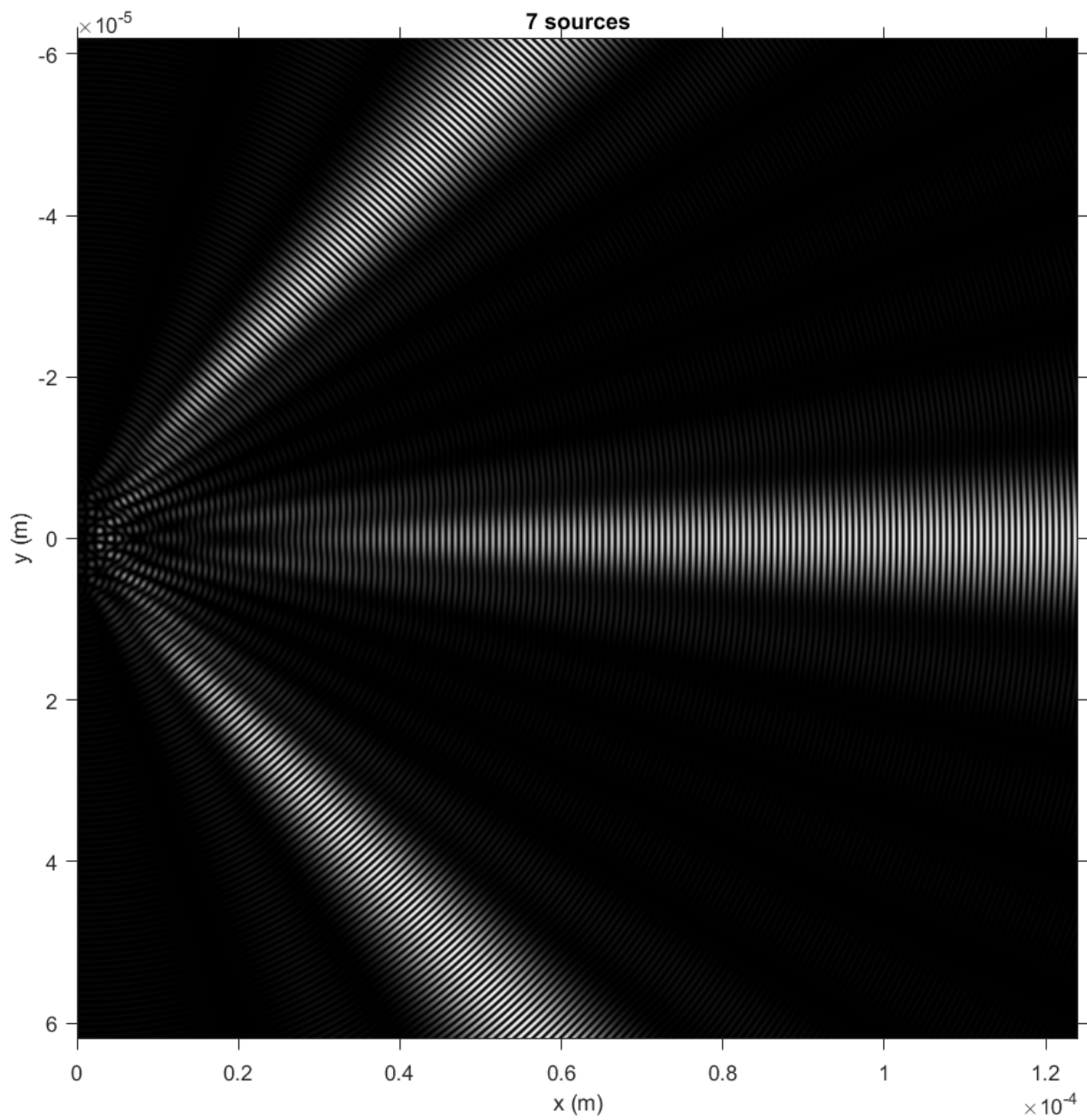


Figure B.4: Intensity distribution for 7 sources, at one time frame.

References

- [1] VNI Cisco. Cisco visual networking index: Forecast and trends, 2017–2022. *White Paper*, 2018.
- [2] Hamid Hemmati. *Near-earth laser communications*. CRC press, 2009.
- [3] Remco den Breeje, Federico Pettazzi and Ivan Ferrario (2018). *Terabit Optical Communication Adaptive Terminal (TOMCAT) Optical Feeder Link Design Definition*.
- [4] Hennes Henniger and Otakar Wilfert. An introduction to free-space optical communications. *Radio-engineering*, 19(2), 2010.
- [5] Zabih Ghassemlooy and Wasiu Oyewole Popoola. *Terrestrial free-space optical communications*. InTech, 2010.
- [6] International Telecommunication Union (2016). Retrieved from: <https://www.unsceb.org/content/itu>.
- [7] Gaussian Beam Propagation (2019). Retrieved from: <https://www.edmundoptics.com/resources/application-notes/lasers/gaussian-beam-propagation/>.
- [8] Satellite frequency bands (2013, November 21). Retrieved from: https://www.esa.int/Our_Activities/Telecommunications_Integrated_Applications/Satellite_frequency_bands.
- [9] Abdulsalam Ghalib Alkholidi and Khaleel Saeed Altowij. Free space optical communications—theory and practices. In *Contemporary Issues in Wireless Communications*. InTech, 2014.
- [10] Dirk Giggenbach and Hennes Henniger. Fading-loss assessment in atmospheric free-space optical communication links with on-off keying. *Optical Engineering*, 47(4):046001, 2008.
- [11] Daniel R Neal, James Copland, and David A Neal. Shack-hartmann wavefront sensor precision and accuracy. In *Advanced Characterization Techniques for Optical, Semiconductor, and Data Storage Components*, volume 4779, pages 148–161. International Society for Optics and Photonics, 2002.
- [12] JW Herbstreit and MC Thompson. Measurements of the phase of radio waves received over transmission paths with electrical lengths varying as a result of atmospheric turbulence. *Proceedings of the IRE*, 43(10):1391–1401, 1955.
- [13] Wimar Klop, Remco den Breeje, and Ivan Ferrario (2018). *Terabit Optical Communication Adaptive Terminal (TOMCAT) Optical Ground Terminal Design Definition*.
- [14] Richard C Olsen and RC Olsen. *Remote sensing from air and space*, volume 229. SPIE Press Bellingham, 2007.
- [15] Wes McGowan. Water processing. *Residential, Commercial, Light-Industrial, 3rd edition Water Quality Association*, 2000.

- [16] D Tröndle, P Martin Pimentel, C Rochow, H Zech, G Muehlnikel, F Heine, R Meyer, S Philipp-May, M Lutzer, E Benzi, et al. Alphasat-sentinel-1a optical inter-satellite links: run-up for the european data relay satellite system. In *Free-Space Laser Communication and Atmospheric Propagation XXVIII*, volume 9739, page 973902. International Society for Optics and Photonics, 2016.
- [17] Knut Böhmer, Mark Gregory, Frank Heine, Hartmut Kämpfner, Robert Lange, Michael Lutzer, and Rolf Meyer. Laser communication terminals for the european data relay system. In *Free-Space Laser Communication Technologies XXIV*, volume 8246, page 82460D. International Society for Optics and Photonics, 2012.
- [18] M Gregory, F Heine, H Kämpfner, R Meyer, R Fields, and C Lunde. Tesat laser communication terminal performance results on 5.6 gbit coherent inter satellite and satellite to ground links. In *International Conference on Space Optics—ICSO 2010*, volume 10565, page 105651F. International Society for Optics and Photonics, 2017.
- [19] Don M Boroson, Bryan S Robinson, Daniel V Murphy, Dennis A Burianek, Farzana Khatri, Joseph M Kovalik, Zoran Sodnik, and Donald M Cornwell. Overview and results of the lunar laser communication demonstration. In *Free-Space Laser Communication and Atmospheric Propagation XXVI*, volume 8971, page 89710S. International Society for Optics and Photonics, 2014.
- [20] Optical constants of Fused silica (2019). Retrieved from: https://refractiveindex.info/?shelf=glassbook=fused_silicapage=Malitson.
- [21] Kristian Buchwald (2007). Fused silica transmission gratings. Retrieved from: <https://ibsen.com/technology-2/white-paper-fused-silica-transmission-gratings>.
- [22] Pieter Kappelhof and Jan Nijenhuis (2019). *Opto-mechatronics Lecture 8 - Alignment mechanisms*, Delft University of Technology.
- [23] Kinematic and Quasi-Kinematic Constraints: What They Are How They Work (2006). Retrieved from: <https://wp.optics.arizona.edu/optomech/wp-content/uploads/sites/53/2016/10/FellowesTutorial1.pdf>.
- [24] Anees Ahmad. *Handbook of optomechanical engineering*. CRC Press, 2017.
- [25] J.P. Kappelhof (2000). Anthology from the mechanical design of the GAIA OPD Testbench. *Modifications, design and lessons learned from alignment mechanisms and mountings of optical components*. TNO-report.
- [26] Round wedge prisms, application idea: beam steering (2019). Retrieved from: https://www.thorlabs.de/NewGroupPage9.cfm?ObjectGroup_ID=147.
- [27] N. van der Lee (2007). Uitleijnmechanismen: Overzicht. TNO-report.
- [28] Aluminium (AlSi10Mg). *Ontwerp specificaties* (2019). Retrieved from: <https://www.rapidcenter.nl/nl/materialen/aluminium-alsi10mg>.
- [29] EOS Aluminium (AlSi10Mg). *Material data sheet* (2014). Retrieved from: https://gpiprototype.com/pdf/EOS_Aluminium_AlSi10Mg_en.pdf.
- [30] ASM Aerospace Specification Metals Inc. *Aluminum 6061-T6* (2019). Retrieved from: <http://asm.matweb.com/search/SpecificMaterial.asp?bassnum=MA6061T6>.
- [31] John Banhart, J Baumeister, and M Weber. Damping properties of aluminium foams. *Materials Science and Engineering: A*, 205(1-2):221–228, 1996.
- [32] Titanium (Gr23). *Ontwerp specificaties* (2019). Retrieved from: <https://www.rapidcenter.nl/nl/materialen/titanium-gr23>.

-
- [33] Engineering ToolBox. *Thermal Expansion of Metals* (2005). Retrieved from: https://www.engineeringtoolbox.com/thermal-expansion-metals-d_859.html.
- [34] Aluminium / Aluminum 1060 Alloy (UNS A91060) (2012). Retrieved from: <https://www.azom.com/article.aspx?ArticleID=6587>.
- [35] Colin G Gordon. Generic vibration criteria for vibration-sensitive equipment. In *Optomechanical Engineering and Vibration Control*, volume 3786, pages 22–34. International Society for Optics and Photonics, 1999.
- [36] Thermal contact resistance (2011). Retrieved from: <http://www.thermopedia.com/content/1188/>.